

Calibration and Validation of
Argus 1000 Spectrometer –
A Canadian Pollution Monitor

Rajinder K. Jagpal

A DISSERTATION SUBMITTED TO THE FACULTY OF GRADUATE STUDIES

IN PARTIAL FULFILMENT OF THE REQUIREMENTS

FOR THE DEGREE OF

DOCTOR OF PHILOSOPHY

GRADUATE PROGRAM IN PHYSICS AND ASTRONOMY

YORK UNIVERSITY,

TORONTO, ONTARIO

June 2011

**Calibration and Validation of Argus 1000
Spectrometer –A Canadian Pollution Monitor**

by **Rajinder K. Jagpal**

A dissertation submitted to the Faculty of Graduate Studies of York University in partial fulfillment of the requirements for the degree of

DOCTOR OF PHILOSOPHY

Copyright

Permission has been granted to: a) YORK UNIVERSITY LIBRARIES to lend or sell copies of this dissertation in paper, microform or electronic formats, and b) LIBRARY AND ARCHIVES CANADA to reproduce, lend, distribute, or sell copies of this dissertation anywhere in the world in microform, paper or electronic formats and to authorize or procure the reproduction, loan, distribution or sale of copies of this dissertation anywhere in the world in microform, paper or electronic formats. The author do reserve other publication rights and the dissertation nor may extensive extracts from it be printed or otherwise reproduced without the author's written permission.

Abstract

Argus 1000 is a modern, light-weight and inexpensive micro-spectrometer. It is representative of a new generation of miniature remote sensing instruments to monitor pollutants and greenhouse-gas emissions from space. Argus was launched on aboard CanX-2 micro-satellite on the 28th of April 2008 as part of a technology demonstration mission. Operating in the near infrared and nadir-viewing mode, Argus is able to provide an efficient capability for the pollution monitoring of Earth-based sources and sinks of anthropogenic pollution. It has 136 channels in the near infrared spectrum $0.9 - 1.7 \mu\text{m}$ with a spectral resolution of 6 nm and an instantaneous spatial resolution of 1.4 km at 640 km orbit. The instrument is a demonstrator for a future micro-satellite network that can supply near-real time monitoring of pollution events in order to facilitate the monitoring of climate change. In this thesis a description of the instrument, its in-orbit performance as well as a preliminary retrieval of space data, based on our theoretical and laboratory calibration programs, are provided and discussed.

Acknowledgements

It takes a long time to write a PhD thesis, though not as long as it takes to lay some rail track, surprisingly. I would here like to express my thanks to the people who have been very helpful to me during the time it took me to write this thesis. It is difficult to overstate my gratitude to my Ph.D. supervisor, Prof. Brendan Quine. With his enthusiasm, his inspiration, and his great efforts to explain things clearly and simply, he helped to make atmospheric physics exciting for me. Throughout my thesis-writing period, Prof. Brendan Quine provided encouragement, sound advice, good teaching, good company, and lots of good ideas. I would have been lost without him. I am also thankful for the excellent example he has provided as a successful physicist and York University professor.

I would like to thank my committee members Prof. Regina Lee and Dr. Brian Solheim for guiding me through successive academic reviews. I also thank Prof. Hugh Chesser who has helped me understand and utilize the Satellite Communication Kit (STK) that is crucial to determine the location of the satellite and the region of the earth it views. I am also grateful to Dr. Yajnavalkya Bhattacharya for discussions and review during writing this thesis. I am grateful to the staff of Physics and Astronomy at York, for helping the department to run smoothly and for assisting me in many different ways. Marlene Caplan, Nick Balaskas and Lauren deserve special mention. I am thankful to the graduate student and Argus team member Guy Benari for supplying software to obtain geo-location maps.

I am indebted to my many student colleagues for providing a stimulating and friendly environment in which to learn and grow. I am especially grateful to Sanjar Abrarov who always gave me good friendly advice. I am also thanking my friends and colleagues specially Farid Ahmed, Raj Seth, Alex Ho, Kenneth Sinclair and Abhay Rai at York. I wish to thank my entire extended family for providing a loving environment for me. My brothers, my sister-in-law, my uncles, and first-cousins-once-removed were particularly supportive.

My research work is supported by the Natural Sciences and Engineering Research Council of Canada, York University and Thoth Technology Inc. The CanX-2 space mission is supported by Defense Research and Development Canada (Ottawa), MacDonald Dettwiler and Associates Space Missions, Dynacon Incorporated, Ontario Centers of Excellence, ETech Division, Canadian Space Agency and Radio Amateur Satellite Corporation (AMSAT). I like to acknowledge Prof. R. E. Zee and his team, University of Toronto Institute for Aerospace Studies, for facilitating the first flight of Argus 1000 spectrometer and for providing the science and attitude data presented here.

Heartiest Thanks are due to Dr. Caroline Roberts, President, Thoth Technology Inc. Dr. Caroline Roberts closely collaborated with Argus research team and kindly offered her support with a with many activities – technical and proposal writing, sane advice whenever asked for, help with various applications, and giving plenty of publicity to Argus 1000 through timely media releases.

Lastly, and most importantly, I wish to thank my family – parents Ram Jagpal and Roop Rani Jagpal, wife Rajni Jagpal and children Amisha, Harshal and Himansh. They

have lovingly raised, taught and supported me throughout various phases of my life. To them I dedicate this thesis.

Table of Contents

Abstract	iv
Acknowledgements	v
Table of Symbols for Mathematics.....	xii
List of Figures.....	xiii
List of Tables.....	xxi
1.0 INTRODUCTION.....	1
1.1 Research Objectives.....	4
1.2 Thesis Organization.....	5
2.0 BACKGROUND.....	7
2.1 Argus 1000 Measurement Objectives.....	10
2.2 A review in trace gas measurements from Space	13
2.2.1 Remote sensing instruments beyond Argus spectral range.....	13
2.2.2 Remote sensing instruments within Argus spectral range	15
2.3 Argus 1000 Instrument Design	22
2.4 Small is beautiful!.....	26
2.5 CanX-2 (Canadian Advanced Nanosatellite eXperiment-2).....	28
2.6 Launch of CanX-2 Sattelite	31
3.0 THE ARGUS SPECTROMETER	35
3.1 Detector System	36
3.2 Optical Design	38
3.3 Argus Interfaces	43
3.3.1 Mechanical Interface.....	43
3.3.2 Power Interface	44
3.3.3 Communications Interface	44
3.3.4 Timing of Spectra Acquisition.....	45

3.3.5 Data Packet Format.....	45
3.3.6 Command format	46
3.3.7 Argus Commands.....	47
3.3.7.1 Exposure Time	47
3.3.7.2 Capacitor Selection	47
3.3.7.3 Cooler Temperature Setting.....	48
3.3.7.4 Scan Count	48
3.3.7.5 Auto-exposure.....	48
3.3.8 Argus Connectors.....	48
4.0 SPECTROMETER CALIBRATION METHODOLOGY	49
4.1 Wavelength Calibration	49
4.2 Radiance Calibration.....	50
4.3 Gas Absorption Calibration	53
4.4 Space Qualification Testing.....	56
4.4.1 Vibration Testing	56
4.4.2 Thermal Vacuum Test.....	57
4.5 Geolocation of Argus data	59
4.5.1 Satellite Coordinate System.....	59
4.5.1.1 Earth-centered inertial (ECI) frame	60
4.5.1.2 Earth-centered Earth-fixed (ECEF) frame	60
4.5.1.3 Spacecraft Body Frame.....	60
4.5.2 Satellite Attitude Determination	61
4.5.2.1 Geolocating the Argus Footprint	61
4.5.3 Correlation CanX-2 geolocation information with Argus Data	62
4.6 Observation Timing and Location Methodology.....	63
4.7 Overview of Radiative Transfer and Forward Modeling.....	66
4.7.1 Radiative Transfer Equations	70
4.7.2 Atmospheric Retrieval Methodologies	73

4.7.3 The GENSPECT Radiative Transfer Model.....	76
4.7.4 Instrument Slit Function	78
4.7.5 Instrument Forward Model	78
4.7.6 Retrieval Code and Library Functions	79
4.8 Effect of Surface Albedo	81
4.9 Cloud Process Method	82
4.10 Simulated Instrument sensitivity to CO ₂	84
5.0 RESULTS AND DISCUSSION	86
5.1 Wavelength Calibration Results	86
5.2 Radiance Calibration Results.....	90
5.3 Gas Cell Calibration	90
5.4 Space Environmental Test Results.....	95
5.5 Geolocation Results	99
5.6 Space Data Results.....	103
5.6.1 December 12, 2008 (First Data)	103
5.6.2 June 11, 2010 (Vancouver, Canada)	106
5.6.3 Space Observation Results over Ocean & Land	108
5.7 Retrieval Results	110
5.7.1 Results of data from May 28 and Sept 20, 2010.....	115
5.7.2 Presence of Cloud	119
5.7.3 Comparison of Rural vs. Industrial Zones (June 2, 2010 data over India).....	120
5.8 Comparison of Argus 1000 and GOSAT	122
5.9 Errors Analysis for Argus 1000	124
5.9.1 Errors Wavelength Calibration	124
5.9.2 Error due to Radiance Calibration	126
5.9.3 Error in Gas cell Measurements.....	128
5.9.4 Error due to Geolocation Analysis	129
5.9.5 Error in Retrieval Analysis	130

6.0 CONCLUSIONS	134
6.1 Future Work	137
REFERENCES	140

Table of Symbols for Mathematics

Physical quantity	Symbol
Irradiance	Y
Area	A
Detector temperature	D_T
Radius	r
Radiant Power	P
Solid angle	Ω
Maximum acceleration experienced by accelerometer	$g_{peakload}$
Actual acceleration experienced by accelerometer	g_{load}
Simulated radiance	R_t
Experimental radiance	R_e
Nadir angle	η
Density of the material	$\rho(x)$
Mass extinction cross-section	$k(\lambda)$
Decrease in radiance	$dI(\lambda)$
Emission coefficient	$j(\lambda)$
Source function	$J(\lambda)$
Optical depth	τ
2 sigma truncated Gaussian function	$F(z)$

List of Figures

Fig. 1: The industrial sources of atmospheric pollution. [http://www.green.in.msn.com/environmentalthreats]	1
Fig. 2: Monthly mean atmospheric carbon dioxide at Mauna Loa Observatory, Hawaii, a 50-year history of atmospheric CO ₂ buildup [NOAA Earth System Research Laboratory 2010.]: [http://www.esrl.noaa.gov/gmd/ccgg/trends/co2_data_mlo.html]	3
Fig. 3: Major components of air on Earth by volume (left) with other trace gas composition expanded and shown on a log scale (right) [Wallace and Hobbs, Atmospheric Science, An Introductory Survey, 1997].	7
Fig. 4: Near Infrared space instrument.	16
Fig. 5: Argus Observation Geometry for Pollution Detection.	23
Fig. 6: Argus design functional diagram showing the various components: optics (blue), hardware layer (tan), driver layer (red), software layer (green), and ground-system electronics (yellow) [Thoth Technology. Inc., 2010].	24
Fig. 7: Satellites flying in formation [Source UTIAS].	27
Fig. 8: Overview of the CanX-2 bus and device locations [Image credit UTIAS].	29
Fig. 9: The front end view of engineering model Argus 1000 (pointed by arrow) attached with CanX- 2 nano-satellite [Source UTIAS].	30
Fig. 10: The location of the CanX-2 in the upper stage of the rocket [Source ISRO].	32

Fig. 11: (a) CanX-2 & NTS integrated along with the rest of the small sat XPODs to the upper stage (image credit: UTIAS/SFL), (b) the final assembly of the rocket in Satish Dhawan Space Centre, (c) the launch of the rocket, India, on 28 April 2008 [Source ISRO].....	33
Fig. 12: Argus 1000 Spectrometer: (a) actual and (b) schematic representations.....	35
Fig. 13: Principle of Photo-Detector Circuit Operation.....	36
Fig. 14: Detector line sequence.....	37
Fig. 15: Detector Quantum Efficiency (data from detector data sheet).....	37
Fig. 16: Absorption cross-sections for CO ₂ , and O ₂	39
Fig. 17: Absorption cross-sections for H ₂ O, and CH ₄	40
Fig. 18: Sensitivity of GENSPECT code showing a 1% change in concentration of the species shown in the legend. The figure was constructed atmosphere typical of June at 40N containing O ₂ , CO ₂ , N ₂ O, CH ₄ and H ₂ O at typical volume mixing ratios and isotope values over 0-50 km altitude range.....	40
Fig.19: Optical layout schematic (300 groves/mm), spectral range 900-1700 nm, 30 mm input optics, 35 mm main mirror.....	42
Fig. 20: Argus 1000 Spectrometer External Dimensions and Mechanical Axes.....	43
Fig. 21: Setup for calibration of the Argus 1000 spectrometer (i.e. calibrate pixel position with wavelength).....	49
Fig. 22: Block diagram for radiance calibration of Argus 1000.....	51
Fig. 23: Hemispherical spectral reflectance of white tile for calibration of Argus 1000 micro-spectrometer.....	53

Fig. 24: CO ₂ absorption measurement set up.....	54
Fig. 25: Flow-chart for conversion of synthetic radiance into detector counts.....	55
Fig. 26: Argus 1000, (shown by arrow), is attached to the vibration system at York University, Toronto.....	57
Fig. 27: Argus 1000 (shown by arrow) is attached for thermal vacuum test setup.....	58
Fig. 28: Argus Footprint and Earth-Centered-Earth-Fixed frame determination.....	61
Fig. 29: September 2010, recorded Argus data (locations shown in red squares).....	64
Fig. 30: Solar Spectrum for Argus spectral window Reproduced from the 2000 ASTM Standard Extraterrestrial Spectrum Reference E-490-00	67
Fig. 31: Energy exchange processes occurring as radiation traverses a medium.....	69
Fig. 32: Typical computation points near line centre	77
Fig. 33: Spectral signatures of some typical backgrounds encountered by Argus observations.....	82
Fig. 34: Radiation path length through the clouds.....	83
Fig. 35: Expected Radiance (Synthetic Model Prediction using GENSPECT) (upper panel) and difference in radiance at +1% change of CO ₂ (lower panel).....	85
Fig. 36: Difference in Spectrometer Counts simulated for a 1% CO ₂ enhancement.....	85
Fig. 37: (a) Argus 1000 spectrometer laser calibration, (b) Argus 1000 spectrometer laser calibration with five Lasers.....	86
Fig. 38: The Argus 1000 angular sensitivity obtained by using milli-Watt collimated laser source at 1064 nm.....	87

Fig. 39: The Argus 1000 vertical sensitivity obtained by using milli-Watt collimated laser source at 1064 nm.....	88
Fig. 40: Four lasers bandwidths for the Argus 1000.....	89
Fig. 41: Normalized area plots at scaled FWHM using four lasers of four different wavelengths.....	89
Fig. 42: The variation of (a) the photons count (b) joules count with respect to the wavelength for 1000 W calibrated lamp.....	90
Fig. 43: (a) Comparison between CO ₂ and Air absorption spectra (b) Counts difference of CO ₂ compared to air.....	91
Fig. 44: (a) Comparison laboratory observed (gas cell flushed with CO ₂ for 20 minutes) (b) and forward-model (GENSPECT) equivalent detector counts and (b) the difference between these two detector counts. The forward model assumes pure CO ₂ in a 1 m long glass cell at STP.....	92
Fig. 45: Variation of detector counts showing decrease in transmittance of incident radiation as the concentration of CO ₂ in the gas cell increases with time.....	93
Fig. 46: Variation of Detector counts for Sun, glass cell filled with CO ₂ after 20 minute, glass cell filled with CO ₂ after 10 minute, glass cell filled with Air after 10 minute.....	94
Fig. 47: Variation of Detector counts for glass cell filled with CO ₂ after 20 minute, glass cell filled with CO ₂ after 10 minute, glass cell filled with Air after 10 minute near O ₂ window.....	94

Fig. 48: Variation of Detector counts for glass cell filled with CO₂ after 20 min., glass cell filled with CO₂ after 10 min., glass cell filled with Air after 10 min near CO₂ window.....95

Fig. 49: Sinusoidal vibration test results with spectrometer attached (a) length-wise horizontally and (b) vertically. The lens looks out of the longer side of the instrument.....96

Fig. 50: (a) Detector counts of the Argus at different Temperature and (b) the variation of the intensity for different pixel positions at different temperature.....97

Fig. 51: Temperature variation with respect to time of thermocouples attached at different locations inside the chamber during the vacuum test of Argus.....99

Fig. 52: Geolocated Argus observations using Google Earth with geography and cloud data overlaid. Inset illustrates three consecutive radiance spectra for these locations. Red ellipse shows the corresponding location as dots with an uncertainty zone.....100

Fig. 53: Deviation from nadir view of Argus obtained using spacecraft telemetry.....101

Fig. 54: KML Output in Google Earth of Argus Observations Acquired over Arctic Ocean, on September 15, 2010.....102

Fig. 55: Distribution of nadir angles (deviation from true nadir) for Argus observations – for approximately 91 sample profiles.....103

Fig. 56: Average detector counts of Argus on December 12, 2008. Different colors represent profile number 160, 161, 162.....	104
Fig. 57: Temperature variation of Argus 1000 for 3 minutes data taken on December 12, 2008.....	104
Fig. 58: (a) Raw (unsmoothed) radiance spectra from Argus1000 observation on December 12, 2008. Different colors represent profile number 160, 161, 162.....	105
Fig. 59: Smoothed radiance spectra obtained from raw radiances in Fig. 58.....	105
Fig. 60: Average Counts (Raw detector counts) recorded by Argus1000 on June 11, 2010. Different colors represent profile numbers 15, 16, 17.....	106
Fig. 61: Raw (unsmoothed) radiance spectra from Argus1000 on June 11, 2010.....	107
Fig. 62: Smoothed radiance spectra obtained from raw radiances in Fig. 61.....	107
Fig. 63: Raw (unsmoothed) radiance spectra from Argus1000 on September 20, 2010. Different colors represent profile numbers 129, 130, 131, 132.....	108
Fig. 64: Raw (unsmoothed) radiance spectra from Argus1000 on September 15, 2010. Different colors represent profile with different latitude and longitude.....	109

Fig. 65: Radiance spectra (left) and Spectra Counts (right) of Argus1000 taken on September 6, 2010 data over land and ocean.....	110
Fig. 66: Simulated (GENSPECT) and observed [actual orbital measurement taken on February 24, 2009 45 degree 25 min N, 75 degree 44 min W near Hudson Bay, Canada] spectrum for Argus 1000 spectrometer.....	112
Fig. 67: Simulated and Experimental radiance for CO ₂ absorption window around 1600 nm (120 % of standard atmospheric concentrations used).....	113
Fig. 68: Synthetic and Experimental radiance for CO ₂ absorption window around 1600 nm (May 28, 2010 observation at 15:27 GMT) latitude is 28°37'33" N, longitude is 77°13'44" E and Sun angle is 65°	117
Fig. 69: Synthetic and Experimental radiance for CO ₂ absorption window around 1600 nm (September 20, 2010 observation at 15:30 GMT) latitude (54°11'18") S and longitude (71°22'32") W respectively.....	117
Fig. 70: Comparison of Synthetic and Argus radiance observations (upper panel) and difference of theory and Argus measured radiance (lower panel).....	118
Fig. 71: Radiance plot for profile with cloud and without cloud of the data obtained on December 12, 2009.....	119
Fig. 72: Geolocated Argus observations using Google Earth with geography and cloud data overlaid. Inset illustrates three consecutive radiance spectra for these locations. Red ellipse shows the corresponding location as dots with an uncertainty zone.....	120

Fig. 73: Geolocated Argus observations using Google Earth with geography and cloud data overlaid. Inset illustrates three consecutive radiance spectra for these locations. Red ellipse shows the corresponding location as dots with an uncertainty zone.....121

Fig. 74: GOSAT observed spectral interferogram radiance (blue) and its smoothed variation (red).....123

Fig. 75: Comparison of GOSAT and Argus radiance observations (upper panel) and difference of GOSAT and Argus measured radiance (lower panel).....124

List of Tables

Table 1: Abundance, radiative forcing estimates since 1780 (15% uncertainty in total forcing) and projected additional forcing by 2050 (IPCC SRES A1b scenario), trend per year.	9
Table 2: Species observed by Argus.....	12
Table 3: NIR Space Instruments and their basic parameters.....	20
Table 4: Characteristics of the space satellites carrying NIR instruments.....	21
Table 5: Argus Spectrometer Specifications (Argus Owners Manual).....	24
Table 6: CanX-2 Orbital Parameters.....	34
Table 7: Argus 1000 Data Packet Format (CanX-2 flight models).....	46
Table 8: Laser types used for calibration.....	50
Table 9: Typical Argus 1000 data parameters for a sampling of different profiles.....	65
Table 10: Errors in calibration parameters.....	128
Table 11: Uncertainties in Position and Time.....	130
Table 12: Radiance average and RMS errors due to uncertainties in measurements (co-adding setting of 1.0).....	132

1.0 INTRODUCTION

Climate change caused by human activity, is one of the most significant issues facing the global society today. As the world population increases rapidly and the technology-driven global economy becomes progressively more industrialized, we expect that the pace of human-induced modifications to our climate to be accelerated further. As a consequence, many countries are beginning to implement climate-control policies and legislation aimed to curb anthropogenic effects on the environment through initiatives such as carbon-credit taxation. An important pre-requisite for both policy debates and sound scientific models is an accurate determination of the origin, impact and concentration of atmospheric constituents, linked to climate change.



Fig. 1. The industrial sources of atmospheric pollution.

[<http://www.green.in.msn.com/environmentalthreats>].

The effect of human activities on the atmosphere is severe and must not be underestimated. Before the industrial revolution, the CO₂ content in the air remained relatively stable for thousands of years. Current levels of primary greenhouse gases are unprecedented in the past 400,000 years [Bousquet *et al.*, 2000]. Large-scale industrial activities release large quantities of gases directly into our air where they become rapidly well mixed in the atmosphere modifying the chemical composition of the Earth's atmosphere [Chamard *et al.*, 2001].

Solar energy in the visible (and to a lesser degree, in the IR wavelengths) is the primary source of radiation absorbed by the Earth's surface, which is ultimately re-emitted as IR radiation and in turn, partially absorbed in the atmosphere. Increase in the concentration of gases with strong infrared absorption features are of particular concern as they disrupt the natural radiative balance and cause the climate system to retain excess solar energy, inducing the phenomenon of global warming.

Among all the gases contributing to global warming, carbon dioxide CO₂ is, arguably the most important gas directly associated with anthropogenic activities. Therefore, the monitoring of this gas from space in the near infrared region, where its absorption features can be clearly detected, is a matter of scientific importance. Fig. 1 shows the industrial sources of atmospheric pollution from Mandi Gobindgarh, Punjab, India, while Fig. 2 indicates the increase of carbon dioxide in the atmosphere in last 50 years as recorded at Mauna Loa Observatory in Hawaii under the supervision of Charles David Keeling. This graph is called the Keeling Curve and it shows a secular upward

slope in the variation in concentration of atmospheric CO₂ with superimposed biosphere breathing [Keeling and Whorf, 2004].

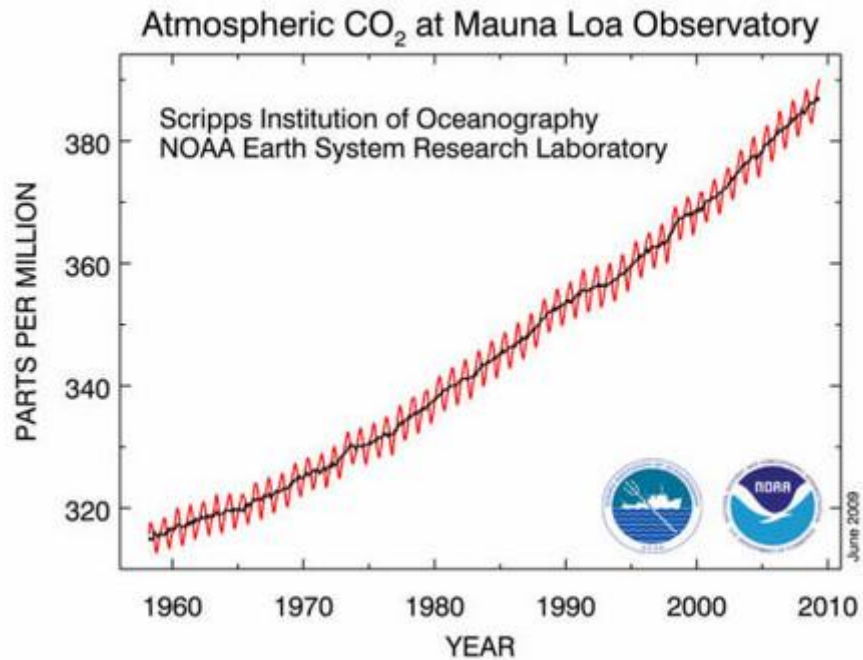


Fig. 2: Monthly mean atmospheric carbon dioxide at Mauna Loa Observatory, Hawaii, a 50-year history of atmospheric CO₂ buildup [NOAA Earth System Research Laboratory 2010.]:

[http://www.esrl.noaa.gov/gmd/ccgg/trends/co2_data_mlo.html].

The Argus 1000 is a micro-spectrometer that has been developed to record space-based measurements of reflected solar radiation in order to monitor radiation absorption by major atmospheric trace gases. The instrument is designed to operate in the 900-1700 nm spectral range, where these species have strong absorption spectra in this region. Argus 1000 has spectral resolution of approximately 6 nm. Within its spectral range are gases including carbon dioxide (CO₂), methane (CH₄), oxygen (O₂) and water vapor

(H₂O) have infrared emission features. Using radiative transfer modeling and with its 1.4 km spatial resolution from 640 km orbit, Argus has also the capability to infer local atmospheric composition in order to locate sources of gas emissions and pollution events. The first flight of Argus was on April 28, 2008 on board of the CanX-2 spacecraft. CanX-2 joined SCISAT-1 in orbit as one of only two Canadian spacecraft to carry atmospheric science packages into orbit over the past forty years. Other Argus 1000 instruments are slated for launch in 2011 & 2012. The CanX-2 mission and Argus instrument team was awarded the Alouette Award by the Canadian Aeronautics and Space Institute on May, 2010. The further development of similar space instrumentation is currently underway in our research laboratory. The Argus 1000 instrument is now available commercially from Thoth Technology Inc. and further flight units have been sold to clients in Europe and Asia.

1.1 Research Objectives

The objectives of my research program are:

- Investigate the effectiveness of the current design of the Argus 1000 micro-spectrometer. This was accomplished by building and testing the proto-flight and flight models in the laboratory, and analysis of actual instrument observations during spaceflight. An important goal for this project has been to make the size of the instrument very small (miniaturize), while maintaining an optimal wavelength range, adequate spectral and spatial resolution, and relatively low net power consumption. [A comparison of Argus optical parameters with contemporary instruments is given in section 2.2.2].

- To provide a technical point of contact and Argus instrument specialist for the CanX-2 mission and coordinate Argus team activities.
- To test and validate the effectiveness of the low-mass spectrometer hardware and associated electronics.
- To calibrate the Argus instrument using different calibration processes including laser, radiance and environmental certification.
- To record an orbital data set that is sufficient to validate on-orbit performance and to provide a data set for the further development of hardware designs and concentration retrieval tools.
- To develop a process to support command Argus observations, instrument settings and to assimilate Argus observations into geo-located data product.
- To compare initial space results with those from other measurement platforms and in comparison with a linear path retrieval algorithm.
- To provide preliminary retrieval results of near-surface greenhouse gas concentration measurements for the detection of pollution plumes from large-scale industrial and other processes.
- To provide a means to generate future experimental inputs for Global Climate Models used to simulate various climate change scenarios and ultimately to assist in the development of a method of validating climate control policy.

1.2 Thesis Organization

The structure of this thesis is as follows. Chapter 1 provides an introduction to the Argus instrument and this thesis. In Chapter 2 we include a comparison with other space-

borne instruments and an overview of CanX-2 satellite, along with measurement objectives of the spectrometer. Chapter 3 describes the electro-optical design of Argus 1000 and its interfaces. Chapter 4 describes the methodology of laser and radiance calibrations and the procedures developed for vibration and thermal vacuum testing. This chapter also describes the methods for geo-location of Argus data. A linear path retrieval process developed using the GENSPECT radiative transfer code is discussed in the latter part of chapter 4. Chapter 5 describes the results for Argus 1000 spectrometer: results of laser and radiance calibration, laboratory experiments with a gas cell and observations from space, and retrieval of trace gas concentrations using the radiative transfer code. This chapter also reviews the overall flight performance of Argus and an analysis of performance errors. A brief comparison with results obtained by GOSAT – another satellite-borne instrument operating approximately in the same spectral region is provided. Concluding remarks are given in Chapter 6.

2.0 BACKGROUND

The average composition of the atmosphere up to an altitude of 25 km is shown in Figure 3 as a pie chart (left), and with the composition of trace species shown in expanded bar-chart form (right panel). The most abundant gas in the atmosphere is Nitrogen followed by Oxygen. The main target gases contributing to the greenhouse effect, H₂O and CO₂ are considered in the thesis [Wallace and Hobbs, 2006].

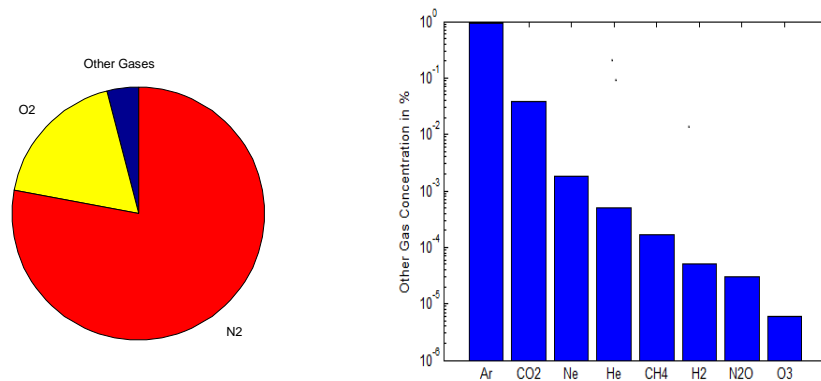


Fig. 3: Major components of air on Earth by volume (left) with other trace gas composition expanded and shown on a log scale (right) [Wallace and Hobbs, Atmospheric Science, An Introductory Survey, 1997].

It is commonly agreed that anthropogenic activity is impacting radiative forcing and changing and warming the climate [Conway *et al.*, 1999 and Cox *et al.*, 2000]. Prior to the start of the industrial revolution in the mid-18th century, the atmospheric concentrations of greenhouse gases were relatively stable for roughly one thousand years; since that time the concentrations have increased at an unprecedented rate. Carbon Dioxide levels, for example, have increased by 0.4% by volume annually, with

concentrations now exceeding 30% of pre-industrial levels. One effect of these increases has been an atmospheric warming at the Earth's surface of 0.4°C to 0.8°C since the late 19th century [Intergovernmental Panel on Climate Change (IPCC), Climate Change 2007]. Paleoclimatic analysis made for the last one thousand years indicates that the magnitude of 20th-century warming exceeds that of any century during this period of time. The completion of drilling on the Vostok ice core in central East Antarctica reveals that present levels of CO₂ and CH₄ are unprecedented in the past 420,000 years [Cox *et al.*, 2000]. Arctic sea ice is being reduced in thickness at the rate of approximately 4 cm per year since 1958, and the low to mid troposphere has warmed by about 0.1°C per decade.

With a total volume-mixing ratio of less than 0.1% by volume (in dry air), greenhouse gases have a critical role in the Earth's radiation budget. Greenhouse gases absorb and emit infrared radiation in the Earth's atmospheric windows, trapping solar radiation in the environment and elevating the surface temperature. Without greenhouse gases in our atmosphere, the expected mean global temperature near the surface would be around -19°C instead of current +14°C [Engelen *et al.*, 2001]. An increase in greenhouse gases causes even more infrared radiation to be trapped and resulting in substantial temperature increase in the surface-tropospheric region. For example, doubling of atmospheric CO₂ concentrations (forecast to occur before 2050, assumed value) produces a positive forcing of approximately 3.7 Wm⁻² compared to the current estimate of Radiative Forcing (RF) of 1.66 ± 0.170 Wm⁻² for a 2005 concentration of 387 ppm [IPCC 2010, Chapter 2]. A summary of these gases' abundance and warming potentials is

presented below in Table 1. Assuming a planetary system in equilibrium with no net gain or loss of the energy to space, the Earth would need to warm by 1.2 °C in order to accommodate this change [Engelen *et al.*, 2001]. It is very likely that the actual effect would be greater [Yang and Wan, 2010]. Climate change prediction is complicated by feedback and non-linearities; the spatial distribution of forcing mechanisms is highly inhomogeneous [Friedlingstein *et al.*, 2001; Cox *et al.*, 2000; Dufresne *et al.*, 2002]. A complex and poorly understood coupling also occurs between the atmosphere and the land surface. The relative importance and risks of anthropogenic emissions can be better understood using the concept of Global Warming Potential (GWP) – a simplified index which describes the radiative impact per unit mass of a greenhouse gas compared with CO₂ over a specified time frame.

Table 1: Abundance, radiative forcing estimates since 1780 (15% uncertainty in total forcing) and projected additional forcing by 2050 (IPCC SRES A1b scenario), trend per year.

Gas	Pre-Industrial Level	Current level	Increase since 1780	Current Forcing	Additional forcing by 2050	Trend per year
CO ₂	280 ppm	387 ppm	107 ppm	1.46 W/m ²	1.9 W/m ²	1.46 ppm
CH ₄	700 ppb	1775 ppb	1075 ppb	0.48 W/m ²	0.22 W/m ²	7.0 ppb
N ₂ O	270 ppb	320 ppb	50 ppb	0.15 W/m ²	0.1 W/m ²	0.8ppb

Retrievals from space-based remote sensing instrumentation have the potential to overcome the limits including spatial coverage and local heterogeneity of a surface

network of in-situ measurements [Olsen *et al.*, 2004]. However, the retrieval of a long-lived and therefore well-mixed gas such as CO₂ is challenging, because only relatively small variations in the concentration distribution may contain the necessary information on potential surface sources and sinks [Reuter *et al.*, 2009]. Several sensitivity studies have evaluated the improvement in carbon flux inversions that would be provided by precise, global space-based column CO₂ data [Dufour and Breon, 2003; O'Brien and Rayner, 2002; Pak *et al.*, 2001; Rayner *et al.*, 2002; Schneising *et al.*, 2008]. The consensus of these studies is that satellite measurements with precisions less than 3.0% will reduce uncertainties in CO₂ sources and sinks due to uniform and dense global sampling [Miller *et al.*, 2007; Zhiming *et al.*, 2002].

2.1 Argus 1000 Measurement Objectives

The Argus instrument provides a means to make measurements of upwelling radiation reflected to space by the Earth and atmosphere. Reflection spectra of sunlight from the Earth's surface contain significant absorption features associated with the molecular absorption of radiation by particular gas species that can be used to infer the composition of the intervening atmosphere [Quine and Drummond, 2001]. Argus 1000 records the NIR signature of the surface-troposphere amounts of the significant greenhouse gases carbon dioxide (CO₂) and water vapour (H₂O) in order to monitor anthropogenic pollution and to identify significant sources and sinks in the atmosphere [Houweling *et al.*, 2005]. Methane (CH₄), Nitrous oxide (N₂O), carbon monoxide (CO) and hydrogen fluoride (HF) species also have absorption features in this spectral region of 1000 nm to 1700 nm, however they are relatively weak. The instrument operates from

space to record IR spectra of reflected solar radiation using a linear photodiode array that records the incident radiant energy. The measured spectra can be compared with IR absorption signatures obtained by linear path forward modeling of the atmospheric absorption process for various concentrations of absorbing species. In the absence of saturation or scattering effects, the amount of absorption depends on the density of the absorber gas along the path. Therefore the primary measurement objective of the instrument is to observe any changes in optical depth, associated with the variation of the following atmospheric gas species in the spectral interval 900-1700 nm (11,111-5,882 cm^{-1}). Table 2 shows the observed absorption in this spectral range and their typical absorption strengths.

CO_2 is widely considered as the main anthropogenic greenhouse gas despite speculations and uncertainties of its natural global sources and sinks [Shimada *et al.*, 1999]. In order to reduce such uncertainties, accurate measurements of atmospheric CO_2 concentration can be used as input for models [Rayner *et al.*, 2001]. Currently, there are several satellite instruments in orbit able to detect atmospheric concentration of CO_2 . The High Resolution Infrared Radiation Sounder (HIRS) [Cao *et al.*, 2005], the Atmospheric Infra Red Sounder (AIRS) [Pagano *et al.*, 2003], and the IASI [Matricard *et al.*, 1999] perform CO_2 sensitive measurements in the thermal infrared (TIR) spectral region [Rozanov *et al.*, 2006].

Table 2: Species observed by Argus

Observed Target Gas	Absorption wavelength and typical peak absorption strength	Comments
Carbon Dioxide (CO ₂)	1240 nm (10 ⁻²³ mol. cm ⁻²) 1420 nm (10 ⁻²¹ mol. cm ⁻²) 1570 nm (10 ⁻²¹ mol. cm ⁻²) 1600 nm (10 ⁻²² mol. cm ⁻²)	1600 nm features are well isolated
Water (H ₂ O)	900nm (10 ⁻²¹ mol. cm ⁻²) 1200 nm (10 ⁻²¹ mol. cm ⁻²) 1400 nm (10 ⁻¹⁹ mol. cm ⁻²)	Dominant IR absorber 900-1700 nm
Carbon Monoxide (CO)	1630 nm (10 ⁻²² mol. cm ⁻²)	Hard to observe due to abundance in this spectral band
Methane (CH ₄)	1660 nm (10 ⁻²⁰ mol. cm ⁻²)	Hard to observe due to 1700 nm cut off
Oxygen (O ₂)	1260 nm (10 ⁻²⁴ mol. cm ⁻²)	Very strong absorption due to O ₂ abundance

These instruments do not detect reflected solar radiation. Instead, they are designed to collect the thermal radiation emitted from Earth's surface and atmosphere. The ability of the instruments to detect the thermal radiation can be advantageous since the thermal radiation data can be obtained not only at day-time but also at night-time. However, the technique based on detection of the thermal radiation has a number of disadvantages including insufficient sensitivity in the lower troposphere where the strongest signals from the sources and sinks are typically expected and a sensitivity

outside the spectral range where the bulk of energy transfer occurs [Mao *et al.*, 2004]. Advantageously, the sensitivity of instruments measuring reflected solar radiation in the NIR/shortwave infrared (SWIR) spectral regions are more correlated (with atmospheric density) and, consequently, show maximum sensitivity near the surface [Kuang *et al.*, 2002]. Instruments utilizing NIR/SWIR measurements to measure carbon dioxide include Argus, SCIAMACHY and TANSO at GOSAT are discussed in the following section. Theoretical absorption spectra are computed recursively for each observation scenario by line-by-line radiative transfer code and will be discussed later in Chapter 5.

2.2 Review of Trace Gas Measurements from Space

In this section, we briefly review observations of trace gases from space using infrared absorption and emission measurements. A majority of nadir-viewing atmospheric sounder missions (prior to 2003) were not programmed to specifically detect the near-infrared (NIR) emission signatures of greenhouse gases such as CO₂. Consequently, these instruments were unsuitable for the observation of gas abundances in the surface-to-lower troposphere region at a surface resolution required to identify pollutants [Gottwald *et al.*, 2006].

2.2.1 Remote sensing instruments beyond Argus spectral range

GOME (Global Ozone Monitoring Experiment on board Europe Remote Sensing Satellite-2, 1995) made measurements from 340-790 nm in order to recover NO₂, O₃, CH₂O, SO₂ and H₂O columns with vertical resolutions approximately 6-8 km. MOPITT (Measurements Of Pollution In The Troposphere) [Drummond *et al.*, 1993] records pressure-modulated TIR spectra in order to recover CO profiles at a surface resolution of

20 km [Drummond and Mand, 1996]. Canada's MAESTRO (Measurement of Aerosol Extinction in the Stratosphere and Troposphere Retrieved by Occultation) consists of two independent spectrometers, one measuring UV and visible spectra from 280 to 550 nm at 1 nm resolution, the second measures visible and near-IR spectra from 525 to 1010 nm, at 2 nm resolution. MAESTRO retrieved concentrations of atmospheric species such as Ozone, NO₂, OClO, BrO etc. with a typical accuracy of approximately 10-20% for each species. TES (Tropospheric Emission Spectrometer, AURA satellite, 2004) deploys a Fourier Transform Spectrometer and MCT detector to record spectra 3200-15000 nm and measures H₂O, CO, CH₄ and O₃ profiles at a spatial resolution of 0.5x5 km. OMI (Ozone Monitoring Instrument, also on-board Aura, 2004) measures near surface concentrations of O₃, NO₂, SO₂, BrO and other species to a surface resolution of 13 km from spectra 270 nm-500 nm. IASI (Infrared Atmospheric Sounding Interferometer) [Phulpin *et al.*, 2002], records FTS (Fourier transform spectroscopy) spectra and retrieves CO, CH₄ and N₂O integrated content at a surface resolution of 10x10 km². MIPAS (Michelson Interferometer for Passive Atmospheric Sounding) is a high-resolution instrument designed to measure concentration profiles of atmospheric constituents on a global scale [Burkert *et al.*, 2007]. MIPAS is a limb emission sounding instrument operating in the spectral region between 4150 nm and 14600 nm with spectral resolution of 0.035 cm⁻¹. MIPAS measures a series of emission spectra from different tangent heights. The main target gases for MIPAS are O₃, CH₄, N₂O and HNO₃ plus 20 other species. MAPS (Measurement Air Pollution Satellites) instrument measured carbon monoxide levels in the troposphere. MicroMAPS, a successor to MAPS, but intended to observe over a

longer duration, is a gas filter correlation radiometer capable of detecting trace atmospheric gasses by remotely sensing their infrared (IR) absorption characteristics [Walberg *et al.*, 1999]. MicroMAPS is based on a commercial instrument called GASCOFIL(GAS COrrelation FILter) developed by Resonance Ltd. for pollution monitoring. The method can be used to detect a number of trace species (including CH₄, SO₂, and NO₂), with the current version of MicroMAPS able to detect CO and N₂O from a nadir viewing airborne or orbital platforms.

2.2.2 Remote sensing instruments within Argus spectral range

Fig. 4 shows the various space instruments working in the spectral region of 900 nm to 1700 nm where CO₂ and other species may be observed. AIRS is one of six instruments flying on board NASA's Aqua satellite, launched on May 4, 2002. AIRS measures trace greenhouse gases such as ozone, carbon dioxide, and methane [Pagano *et al.*, 2003]. It retrieves CO₂ in thermal infrared (TIR). Its spectral resolution is 0.5–2 cm⁻¹ and spectral range is 400-1000 nm and 3703-15384 nm [Barkley *et al.*, 2006b]. The Advanced Very High Resolution Radiometer (AVHRR) is a space-borne sensor that is embarked on the National Oceanic and Atmospheric Administration (NOAA) polar-orbiting platform (POES). The AVHRR instruments [Price *et al.*, 1984] are capable of measuring the reflectance of the Earth in 5 relatively wide spectral bands: the first two are centered around the red (600 nm) and near-infrared (900 nm) regions, the third one is located around 3500 nm, and the last two sample the thermal radiation emitted by the planet, around 11000 and 12000 nm, respectively. The first AVHRR instrument was a 4-

channel based radiometer. The latest version acquires the data in a 6th channel located at 1600 nm [Atkinson *et al.*, 1997].

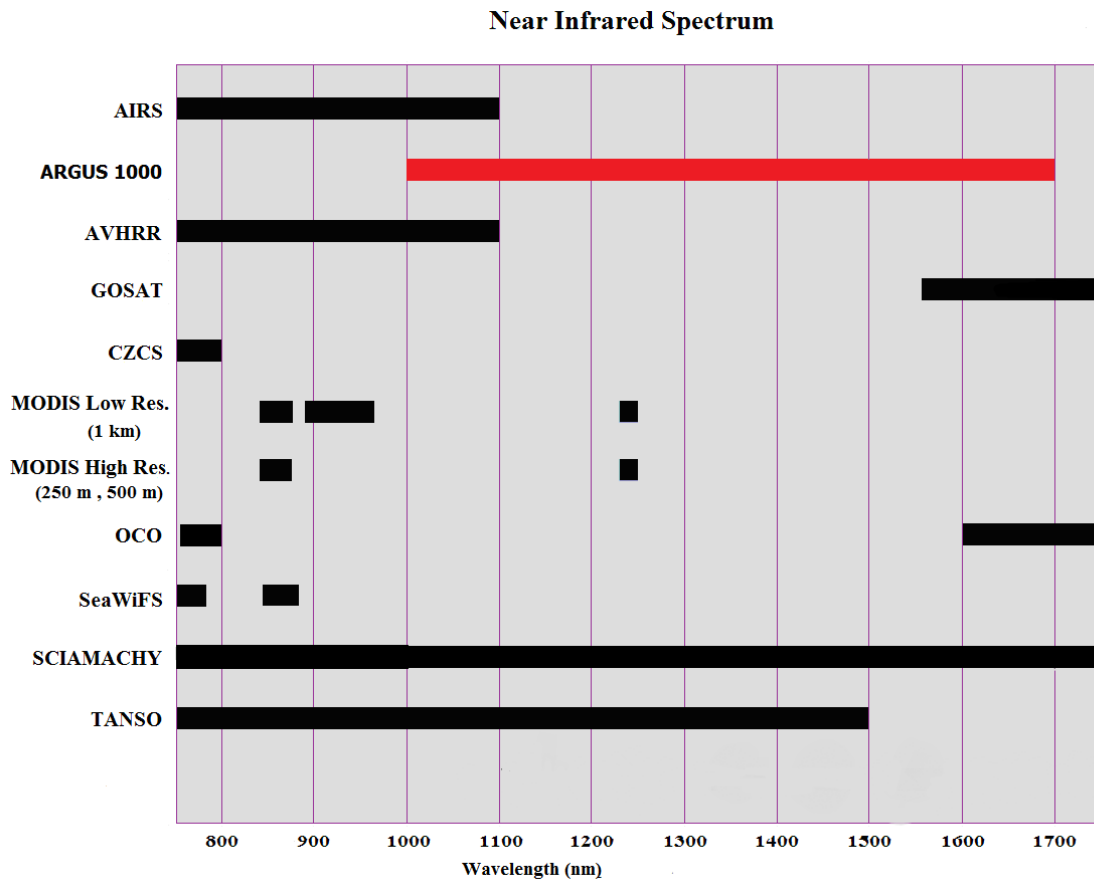


Fig. 4: Near Infrared space instruments (see text for source / references of estimates).

Moderate-resolution Imaging Spectroradiometer (MODIS) was launched into Earth orbit by NASA in 1999 on board the Terra [Barnes *et al.*, 1999] Satellite, and in 2002 on board the Aqua (EOS PM) satellite. Measurements were made in 36 spectral bands ranging in wavelength from 400 nm to 14400 nm at varying spatial resolutions (2 bands at 250 m, 5 bands at 500 m and 29 bands at 1 km). These two instruments were

designed to provide measurements of large-scale global dynamics, such as changes in Earth cloud cover, radiation processes occurring over the oceans, on land, and in the lower atmosphere. Three on-board calibrators—a solar diffuser combined with a solar diffuser stability monitor, a spectral radiometric calibration assembly, and a blackbody—are capable of providing in-flight calibration.

Another planned carbon dioxide observing micro-spectrometer was OCO (Orbiting Carbon Observatory) [Vijay *et al.*, 2007], which was planned to measure within the same NIR spectral region. Unfortunately, the satellite launch was not successful as the spacecraft and its payload were lost shortly after lift-off on 24 February 2009 [Crisp *et al.*, 2004]. The spectral range for OCO is 760-2060 nm with three spectral channels [Chevallier *et al.*, 2007]. The specified field of view is 14.6 mrad and spectral resolution specified is 20,000 which equivalent to 0.08 nm at 1600 nm. The measurement objectives of OCO are very similar to that of Argus; however, these instruments observe three specific bands only where as Argus observes the entire spectral range but at lower spectral resolution. There is a plan to re-launch OCO-2 in February 2013. OCO-2 will also operate in three specific NIR wavelength bands to observe the weak and strong CO₂ bands as well as the O₂ A-band. The weaker CO₂ band (1590-1621 nm) is most sensitive to the CO₂ concentration near the surface. The strong CO₂ band (2041-2081 nm) provides a second and independent measure of the CO₂ abundance. The O₂ A-band (757-772 nm) will provide the required absorption measurements and a proxy measurement of pressure.

Sea-viewing Wide Field-of-view Sensor (SeaWiFS) is the scientific instrument on GeoEye's OrbView-2 (AKA SeaStar) satellite that was a follow-on experiment to the

Coastal Zone Color Scanner on Nimbus 7 [Wang *et al.*, 2005], launched on August 1, 1997 on an Orbital Sciences Pegasus small air-launched rocket. SeaWiFS began operations on 18 September 1997. It has eight spectral band ranges from 370-1000 nm.

SCIAMACHY – SCanning Imaging Absorption spectroMeter for Atmospheric ChartographY- is a passive remote sensing spectrometer observing backscattered, reflected, transmitted or emitted radiation from the atmosphere and Earth's surface [Burrows *et al.*, 2000]. While SCIAMACHY was not designed to retrieve CO₂ with the precision and accuracy needed to enhance our knowledge about sources and sinks by inverse modeling [Houweling *et al.*, 2004], it still has the ability to measure CO₂ concentrations to a precision of less than 4% utilizing a Full Spectral Initiation Weighting Function and Modified Differential Optical Absorption Spectroscopy (FSI WFM-DOAS) algorithm [Barkley *et al.*, 2006b and 2007]. SCIAMACHY makes low spectral resolution measurements over a wide wavelength range between 240 to 2380 nm. The spectral resolution for 7th spectral band in the infrared region (1000- 1750 nm) is 1.48 nm. The instrument flies on the board ENVISAT that was launched on March 1, 2002. The primary goal of SCIAMACHY [Buchwitz *et al.*, 2004] was the global measurement of various trace gases in the troposphere and stratosphere retrieved from solar irradiance and Earth's radiance spectra. The large wavelength range is also ideally suited for the determination of aerosols [Gottwald *et al.*, 2006]. SCIAMACHY recorded nadir spectra in bands at a horizontal resolution of 30 km² and provides near real time H₂O, NO₂, CO, N₂O and CH₄ profile data [Buchwitz *et al.*, 2005a and 2005b].

TANSO (Thermal And Near infrared Sensor for carbon Observation) aboard

GOSAT (Greenhouse gases Observing SATellite) launched on January 23, 2009, from the Tanegashima Space Center [Kuze *et al.*, 2009]. The GOSAT (it is also referred in Japanese as Ibuki that means "breath" or "Vitality") [Yokota *et al.*, 2009]. GOSAT is used to measure the densities of carbon dioxide and methane from 56,000 locations on the Earth's atmosphere [Yokota *et al.*, 2005]. GOSAT flies at an altitude of approximately 666 km and completes one revolution in about 100 minutes. It was developed by the Japan Aerospace Exploration Agency (JAXA). It is a Fourier Transform Spectrometer (FTS) with spectral resolution of 0.2 cm^{-1} and spectral range for second spectral band which measures CO_2 is 1560-1920 nm. Over all 2 FTSs cover the wide spectral range from 760-15000 nm. The instrument measures interferograms of solar short-wave infrared spectra reflected from the ground and the atmosphere. The interferograms are transformed with the fast Fourier transformation (FFT) algorithm into spectra, which include the signatures of major greenhouse gases [Hamazaki *et al.*, 2005]. Results are intended for use in tracking gases causing the greenhouse effect.

Argus, SCIAMACHY and TANSO are currently the only orbiting instruments measuring NIR radiation with sufficient spectral resolution for CO_2 retrieval. TCCON (Total Carbon Column Observing Network) is a network of ground-based FTSs recording direct solar spectra in the near-infrared spectral region [Deutscher *et al.*, 2010]. This ground based instrument provides an essential validation resource for the space bound instruments. Its spectral range is 1100 nm to 2500 nm with spectral resolution 0.02 cm^{-1} .

Table 3 shows the basic parameters of the space instruments. Approximately 100

times smaller than other instruments, Argus 1000 is the lowest mass, lowest power space instrumentation package that can be used for location determination of CO₂ polluters.

Table 3: NIR Space Instruments and their basic parameters.

Spectrometer Parameter	SCIAMACHY	AIRS	Argus 1000	TANSO-FTS	OCO-2 (planned)
Satellite	ENVISAT-1	AQUA	CANX-2	GOSAT	OCO
Spatial resolution [km]	30x27 - 30x240	13.5	1.4	0.5 – 1	1.29 – 2.29
Field of view	0.045° x 1.8°	± 49.5°	0.125°	cross-tr. ±35° along-tr.±20°	0.8°
Spectral Range [µm]	0.2 – 2.4	0.4 -1, 3.74- 15.4	0.9 – 1.7	0.758 – 14.3	0.76 – 2.06
Size [m³]	1.8x0.9x1.0	1.4x1.5x.76	0.05x0.06x0.08	1.2x1.1x0.7	1.6x0.4x0.6
Mass [kg]	200	156	0.228	250	150
Power [W]	175	256	2.3	310	165
Developer	Alcatel Space Industries	BAE Systems	York University/Thoth Technology Inc.	ABB Inc/JAXA	Hamilton Sundstrand Sensor
Subject of interest	Measure CO ₂ Detect cloud system structure & aerosols	Measure H ₂ O vapour profiles	Detect and study CO ₂ , H ₂ O, O ₂ & CH ₄	Study the transport mechanism of CO ₂ & CH ₄	Measure atmospheric CO ₂

Table 4 shows the characteristics of the satellites carrying these space borne spectrometers shown above in the Table 3. The mission duration expectation of the satellites varies between 8-10 years.

Table 4: Characteristics of the space satellites carrying NIR instruments.

Satellite	ENVISAT-1	AQUA	CANX-2	GOSAT	OCO-2
Parameter					
Mass [kg]	8140	2850	3.5	1750	460
Dimensions	26×10×5 m ³	2.7×2.5×6.5 m ³	0.1×0.1×0.34 m ³	2.0×1.8×3.7 m ³	2.12 m long by 0.94 m diam. hexagonal
Developer	EADS Astrium	TRW Space & Electronics Group	UTIAS	Inc/JAXA ABB	Hamilton Sundstrand Sensor Systems
Expected mission duration [yrs.]	8	5	6	6	6
Estimated cost of mission [CAD]	230,000,000 [†]	No data	300,000 [†]	390,000,000 [†]	300,000,000 [†]
Flight heritage	1 flight	1 flight	1 flight	1 flight	None
Orbit	sun-synchronous polar orbit	sun-synchronous	sun-synchronous	Sun-synchronous circular orbit	sun-synchronous polar orbit

[†] See text for source / references of estimates.

Argus 1000 being very light, small and simple in electronic design aims to achieve an operating lifetime of more than 6 years in space. In comparison with other instruments, this table clearly indicates that CanX-2 and Argus have significantly reduced mass, cost and power requirements over other technologies currently deployed in space.

2.3 Argus 1000 Instrument Design

Operating in-orbit on the CanX-2 satellite, Argus serves as a working prototype to monitor surface-troposphere amounts of significant greenhouse gases, including carbon dioxide (CO₂) and water vapour (H₂O) in order to monitor anthropogenic pollution and to identify significant sources and sinks in the atmosphere. Argus is designed to make nadir observations of the surface at the sub-satellite point, scanning the Earth with an instantaneous surface resolution approximately 1.4 km., advancing at a ground speed of 7.5 km s⁻¹ as the spacecraft orbits the Earth. The instrument operates in the near-IR band in the 900 nm to 1700 nm range of wavelengths. These characteristics enable the identification of precise location of the pollution sources and their local variations. Argus includes a detector array of 1 × 256 elements that is actively cooled. Each pixel has a radiometric resolution of 12 bits with exposure time ranging from microseconds to seconds for data recording.

Argus is a nadir-pointing instrument located on the spacecraft face oriented towards Earth. A schematic of the Argus pointing geometry is shown in Fig. 5. The Argus 1000 looks downwards in the nadir direction, measuring radiation that leaves the atmosphere in the local vertical. While occultation and limb-view techniques typically offer better vertical resolution, the advantages of a high-surface resolution nadir view are:

- 1) Lower probability of cloud contamination because of small footprint and shorter atmospheric path.
- 2) A precise horizontal spatial resolution.
- 3) Enhanced sensitivity to absorption by the lower atmosphere (below 5 km).

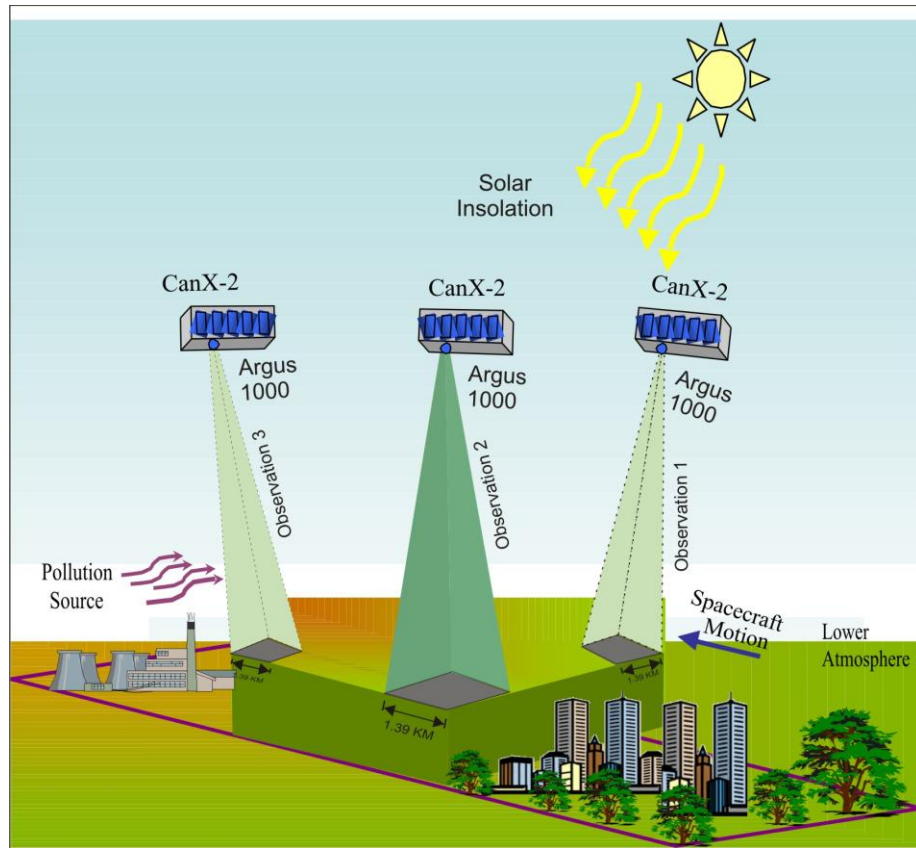


Fig. 5: Argus Observation Geometry for Pollution Detection.

The instrument's functional design is shown in Fig. 6. It includes a microcontroller that controls the device components and acquires the spectra. The command interface accepts commands via prime and redundant serial interfaces; spectra and engineering data are delivered via the same interface.

The instrument consumes a relatively low power of only 1.3 W and contains internal power isolation and regulation. Argus employs a triplet lens fore-optics to discriminate IR radiation onto a spectrally diffracting grating element. Then the signal is focused onto a linear $\text{In}_x\text{Ga}_{1-x}\text{As}$ photodiode array with 256 high-quantum efficiency pixels. The instrument's optical configuration is such that 136 pixels are illuminated.

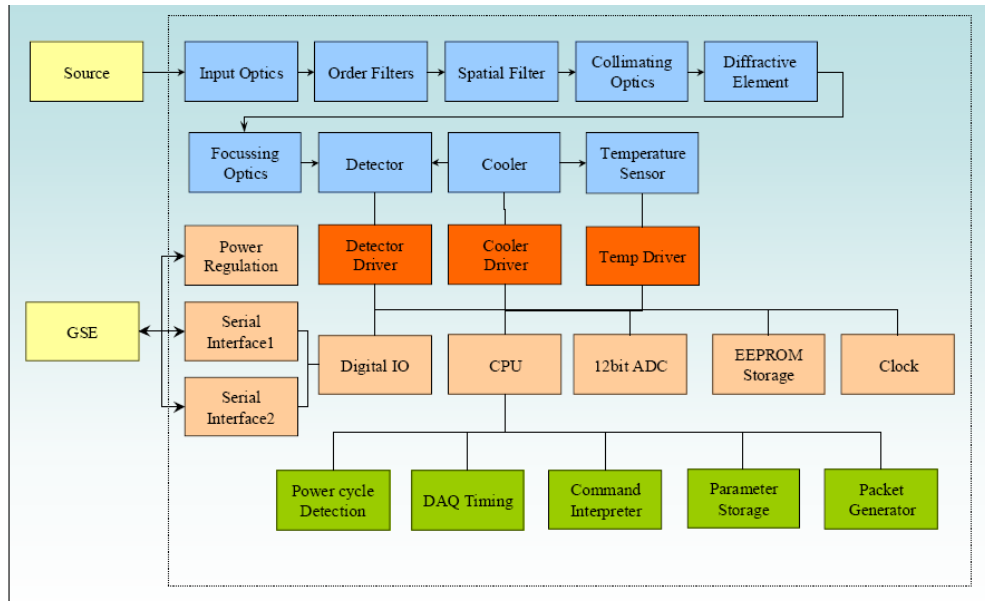


Fig. 6: Argus design functional diagram showing the various components: optics (blue), hardware layer (tan), driver layer (red), software layer (green), and ground-system electronics (yellow) [Thoth Technology. Inc., 2010].

This array represents a hybrid of $\text{In}_x\text{Ga}_{1-x}\text{As}$ and CMOS active-pixel readout electronics where the photo-current is buffered, amplified, and stored. The video channels are differentially sampled in a form of double correlated sampling, which enables the detection of radiation emitted by a 1.56 km^2 surface tile to high precision. An order filter, positioned after the fore optics, prevents the visible radiation (below 900 nm) from entering the spectrometer chamber. The instrument functions as a quantum detector, measuring directly spectrally filtered incident radiation and converting photonic flux into electrical charge in a high-efficiency process that conserves energy. Unlike other methods such as Fourier Transform Spectroscopy, the instrument can be calibrated to provide

Table 5: Argus Spectrometer Specifications (Argus Owners Manual).

Argus 1000	Specifications
1. Optics	Grating spectrometer
2. Configuration	Single aperture [spectrometer]
3. Field of View	0.125° or 2.18 mRad viewing angle around centered camera bore-sight with 15mm fore-optics
4. Mass	228 g
5. Accommodation	40 mm x 50 mm x 80 mm (base x height x length)
6. Operating Temperature	-50° to +50°C
7. Survival Temp	-70° to +70° C
8. Detector	256 element InGaAs diode array with Peltier cooler
9. Grating	12 mm × 12 mm plane gratings, 300 or 600 groves/mm
10. Spectral resolution	6 nm
11. Electronics	8-bit microprocessor with 12-bit ADC, 3.6-4.2V input rail 250mA-1000mA
12. Operational Modes	<ul style="list-style-type: none"> • Continuous cycle, constant integration time • Continuous cycle, adaptive exposure • Single shot
13. Data Delivery	Fixed length parity striped packets of single or co-added spectra with sequence number, temperature, array temperature and operation parameters
14. Integration Time	200 μs to 6.458 s
15. Calibration	Five-wavelength laser calibration and radiance calibration
16. Volatiles	Less than 0.1% volatile internals by mass
17. Exposure Environment	Clean-room class 10,000 or better recommended. Class 1,000 required for optical or internal inspection.
18. Vibration	Launch: 7.5 g, random and 10 g sinusoidal, 20-2000Hz
19. Handling	Factory shipping in double bagged, nitrogen-fill enclosure
20. Signal to Noise Ratio	120:1
21. Dark Noise	11 RMS counts
22. Power Consumption	2.4 W (max)

measurements of absolute radiance. The instrument's detailed specification is shown in Table 5.

2.4 Small is beautiful!

Miniaturized satellites are spacecraft of unusually low weights and small sizes, typically under 500 kg. While all such satellites can be referred to as small satellites, different classifications are used to categorize them based on mass (Gao *et al.*, 2009):

1. Mini-satellite (100–500 kg)
2. Micro-satellite (10–100 kg)
3. Nano-satellite (1–10 kg)
4. Pico-satellite (0.1–1 kg)
5. Femto-satellite (0.01–0.1 kg)

As the potential uses of nanosatellites increase nanosatellite missions will become a growing part of exploitation of space. Nanosatellites are now developed to carry science payloads, communications and tracking networks, or demonstrate the capabilities of new technologies on orbit. The appeal of a nanosatellite's capabilities is reduced mass, size, program duration and ultimately cost. Small satellites are specified as work-efficient, productive and promising. Larger satellites usually use monopropellants or bipropellant combustion rockets for propulsion and attitude control; however, these systems are complex and require spacecraft volume and surface area to dissipate heat. Micro/nanosatellites use typically electric propulsion, compressed gas, vaporizable

liquids such as butane or carbon dioxide or other innovative propulsion systems that are simple, cheap and scalable.

Microsatellites use conventional radio systems in UHF, VHF, the S-band and X-bands. These systems are often miniaturized using more up-to-date technology as compared to larger satellites. Tiny satellites such as nanosatellites and small microsatellites may lack the power or mass for large conventional radio transponders but various miniaturized or innovative communications systems have been proposed, such as laser receivers, antenna arrays and satellite-to-satellite communication networks that will likely mitigate communications issues in future.

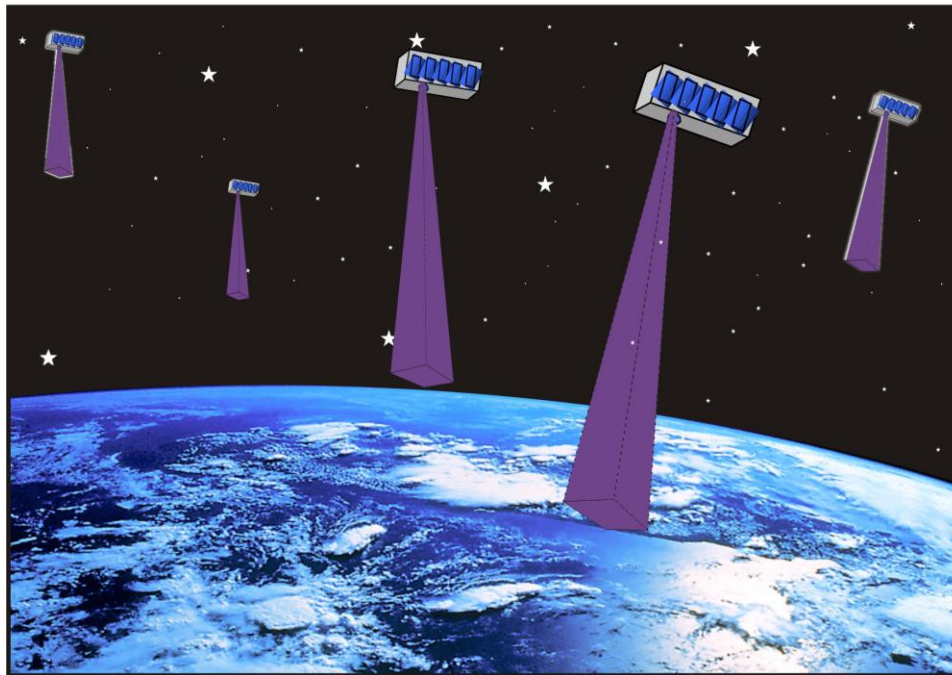


Fig. 7: Satellites flying in formation [Source UTIAS].

In common with larger space subsystems, electronics still needs to be rigorously tested and modified to be "space hardened" or resistant to the outer space environment (vacuum, microgravity, thermal extremes, and radiation exposure).

Miniaturized satellites allow for the opportunity to test new hardware with reduced cost in testing. Furthermore, since more overall risk can be tolerated in an inexpensive mission less space-proven technology can be incorporated into micro and nanosatellites than can be used in much larger, more expensive missions with less appetite for risk.

Miniature space systems can also perform experiments that larger single platforms cannot. A group of small satellites flying in formation, such as those shown in Fig. 7, have several geometrical viewing compared with when performing the same mission over a single, larger satellite. The loss or failure of a single satellite in the cluster network system does not terminate the entire mission. Furthermore, the individual inexpensive satellites in a constellation of satellites can be replaced over time by gradual upgrading the system. It should be noted that the most substantial advantage is the cost savings made feasible by "mass producing" the satellites used in the formation, thus spreading out the non-recurring engineering costs [Sarda *et al.*, 2006].

2.5 CanX-2 (Canadian Advanced Nanosatellite eXperiment-2)

In addition to Argus 1000, the CanX-2 nanosatellite includes a GPS occultation experiment, an advanced materials experiment, and technology demonstrations of new space communication protocols [Sarda *et al.*, 2006]. The CanX-2 spacecraft has dimensions $10 \times 10 \times 34 \text{ cm}^3$, with mass of about 3.5 kg. The spacecraft bus employs an Al 6061-T6 tray-based design to simplify assembly and integration. Fig. 8 shows the

overview of CanX-2 bus and location of its various devices. Most subsystems are directly mounted to a tray, as are most of the body panels that enclose them. Externally, four aluminum rails act as contact surfaces with a deployment system including a CubeSat deployer or an XPOD (X-Picosatellite Orbital Deployer).

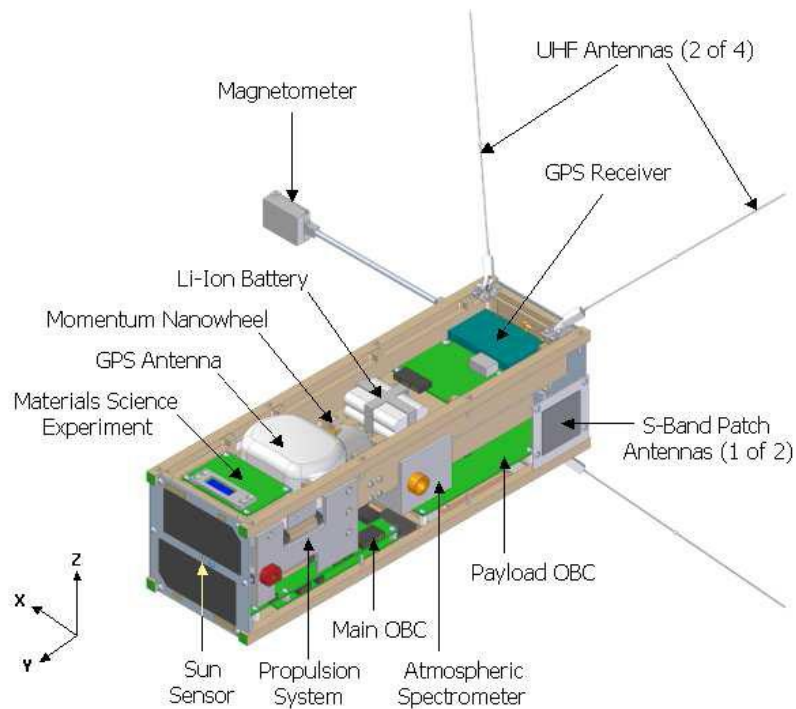


Fig. 8: Overview of the CanX-2 bus and device locations (image credit: UTIAS).

The power on CanX-2 is supplied by 22 surface-mounted triple-junction GaAs solar cells providing nearly 5W on an average that depends on spacecraft orientation. There is a single 3.6Ah Li-ion battery to store electrical energy. An unregulated satellite power bus operates nominally at 4.0 V. When Argus is turned on, it consumes approximately 330 mA of current corresponding to 1.3 W. Power is transferred from the battery and solar cells to Argus through switches on the spacecraft power board. The Argus team communicates with the instrument via scripts that the spacecraft apparatus

upload from the ground. The script turn on the spectrometer, tell the On Board Computer (OBC) to start logging data, configure the spectrometer to the command settings provided by Argus team, and turn off the spectrometer at a specified time, and complete logging. The data is stored in the computer's Static random access memory (SRAM) memory, which is downloaded on the first available communications pass. The size of the files is a maximum of 1Mbytes, which only takes approximately one minute to download at 128 kbits s⁻¹. The attitude control on CanX-2 is determined by a suite of sun sensors and a 3-axis magnetometer. The mission attitude goals are to achieve both attitude determination and pointing with an accuracy of $\pm 10^\circ$ and to maintain a pointing stability of $\pm 1^\circ$. Fig. 9 shows the both front and backend of CanX-2 configuration in real time view during the assembly process.

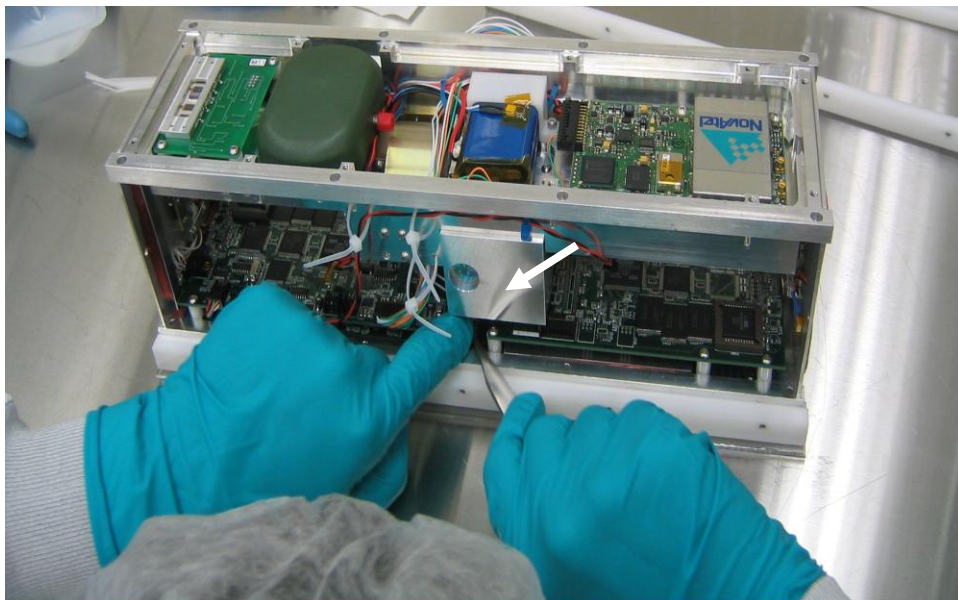


Fig 9: The front end view of engineering model Argus 1000 (pointed by arrow) attached with CanX-2 nano-satellite [Source UTIAS].

2.6 Launch of CanX-2 Satellite

CanX-2 satellite was launched on April 28, 2008 on a PSLV (Polar Satellite Launch Vehicle) of Indian Space Research Organization (ISRO), from the Satish Dhawan Space Centre (SDSC), Sriharikota, India (Longitude: 80.23° Latitude: 13.73°). The primary payload on this flight was CartoSat-2A, a high-resolution panchromatic imaging satellite for India's military, developed by ISRO. Included in the launch payload was ISRO's own microsatellite, IMS-1 (Indian Microsatellite-1), of 83 kg, in addition to eight other secondary payloads. The secondary payloads consisted of the following CubeSats or nanosatellites: CanX-2 of UTIAS/SFL; AAUSat-2 of Aalborg University, Denmark; COMPASS-1, University of Applied Science, Aachen, Germany; Delfi-C3 of the Technical University of Delft, The Netherlands; SEEDS-2 of Nihon University, Japan; CUTE-1.7+APD-2 of the Tokyo Institute of Technology (TITech), Japan; NTS (Nanosatellite Tracking of Ships) of COM DEV / UTIAS/SFL, Toronto, Canada; and Rubin-8-AIS (7 kg) an experimental space technology mission of OHB-System, Bremen, Germany.

The launch of the 8 nanosatellite payloads was executed under a commercial contract between the University of Toronto, COSMOS International (a company of the OHB Fuchs Gruppe, Bremen, Germany), and the Antrix Corporation of Bangalore, India (Antrix being is the commercial arm of ISRO). The location of the CanX-2 and other nanosatellite payloads are shown in Fig.10.

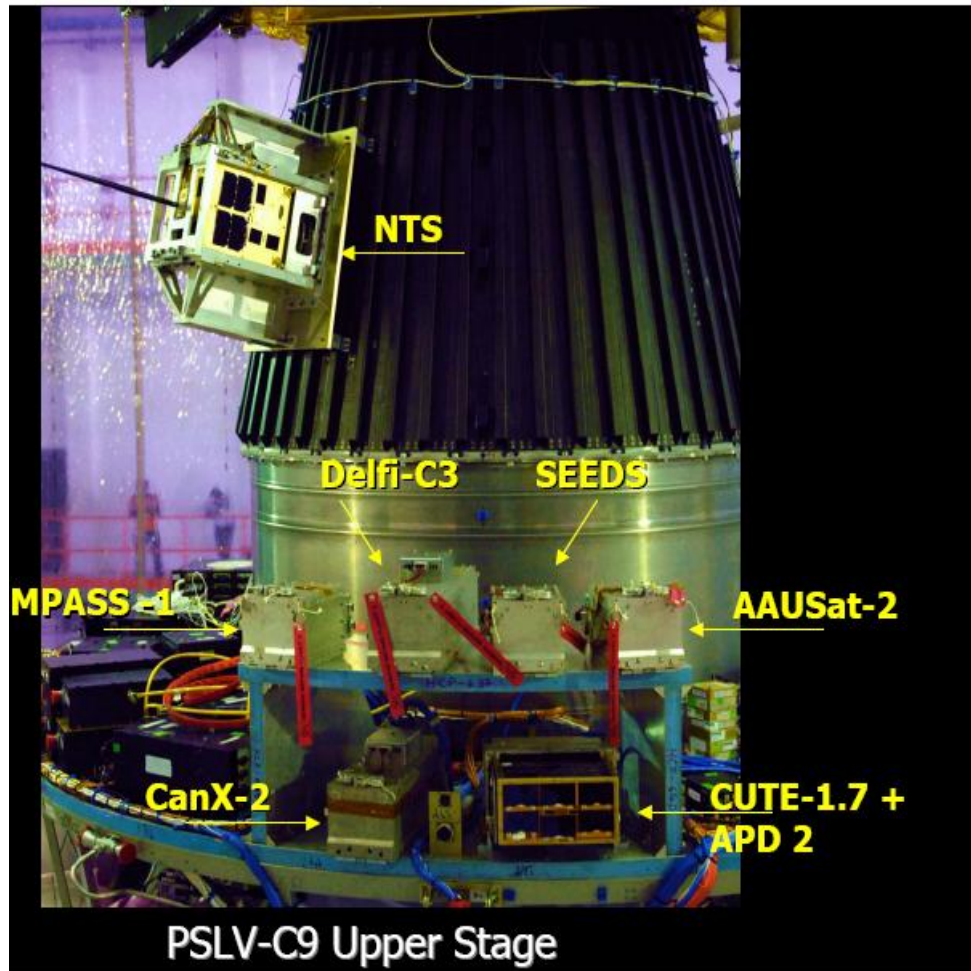


Fig. 10: The location of the CanX-2 in the upper stage of the rocket [Source ISRO].

The upper stage which includes CanX-2, the final assembly of the rocket in Satish Dhawan Space Centre, and the launch of the rocket, and the launch of the rocket are shown in the Fig. 11 a, b, and c, respectively.

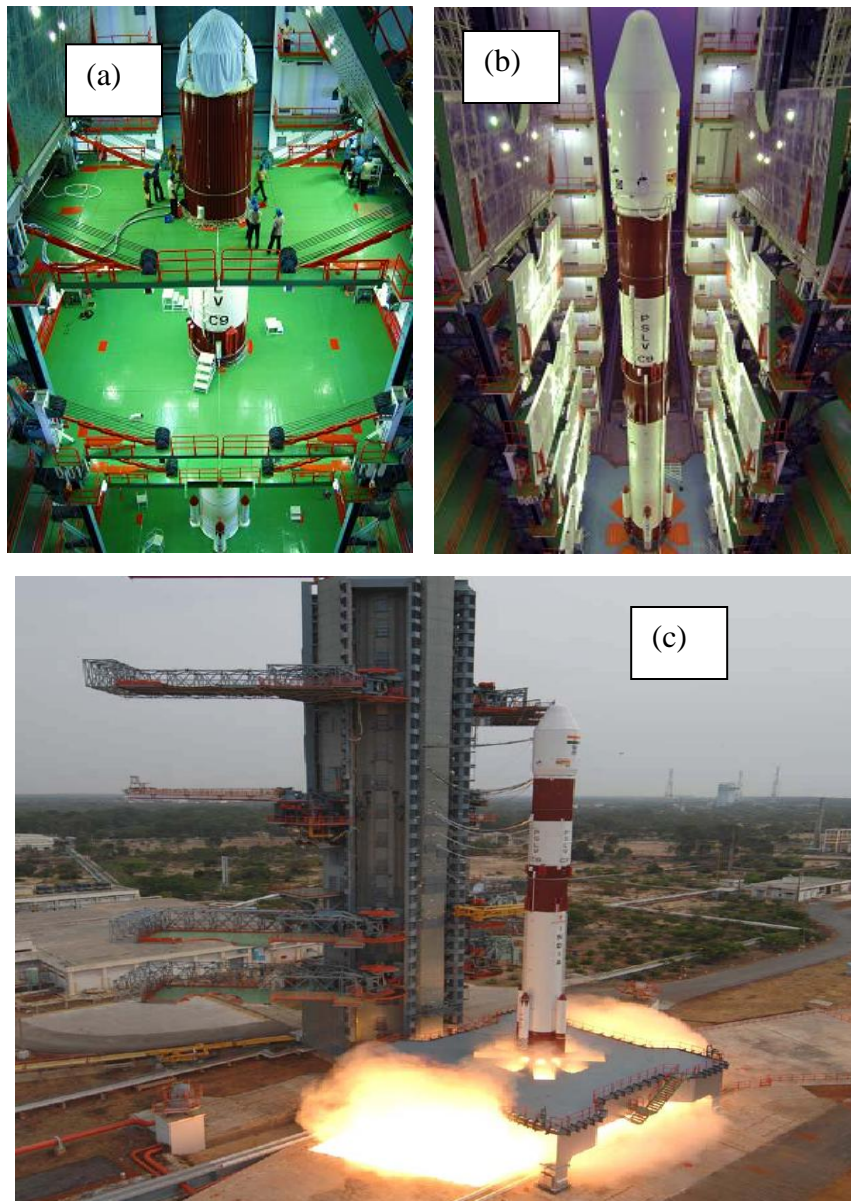


Fig 11: (a) CanX-2 & NTS integrated along with the rest of the small satellite to the upper stage (image credit: UTIAS/SFL), (b) the final assembly of the rocket in Satish Dhawan Space Centre, (c) the launch of the rocket, India, on 28 April 2008 [Source ISRO].

After the successful launch both CanX-2 and Argus 1000 were commissioned, and the first full operations began in March 2009. On September 23, 2008, the first set of scientific data was downloaded during the commissioning phase. Since then, the science team at York University has been working with the spacecraft operators from Space Flight Laboratory (SFL) at University of Toronto Institute for Aerospace Studies (UTIAS) to process the science data and the related spacecraft telemetry principally measurement timing and spacecraft pointing in order to properly analyze the spectrometer observations. The CanX-2 spacecraft is in a 930 am Sun synchronous orbit at an altitude of 640 km [Eagleson *et al.*, 2007]. This orbit was determined by the requirements of the primary launch payload. However, the resulting orbit is near optimal for Argus observations. A Sun synchronous orbit provides for consistent solar illumination conditions with similar solar hour angles during the orbit. Argus data is provided to us every three months for consecutive weeks on the instruction of York University Argus team. The orbital parameters of CanX-2 are given in Table 6.

Table 6: CanX-2 Orbital Parameters

NORAD ID	32790
CanX-2 International Code	2008-021H
Orbit type	Sun synchronous 0930 descending mode
Perigee	620.9 km
Apogee	641.3 km
Inclination	97.9°
Period	97.2 min
Semi Major Axis	7,002.1 km

3.0 INSTRUMENTATION

Argus is a micro-spectrometer with a mass 228 g and dimensions of $45 \times 50 \times 80$ mm³ [Quine *et al.*, 2006], is shown in Figs. 12 (a) and 10 (b). The instrument deploys an Indium Gallium Arsenide ($\text{In}_x\text{Ga}_{1-x}\text{As}$) infrared (IR) detector with diffractive optics. An instantaneous field of view (IFOV) 2.18 mRad provides a high resolution pollution mapping capability for this space based instrument. The device includes a programmable Peltier-effect cooler that enhances noise performance.

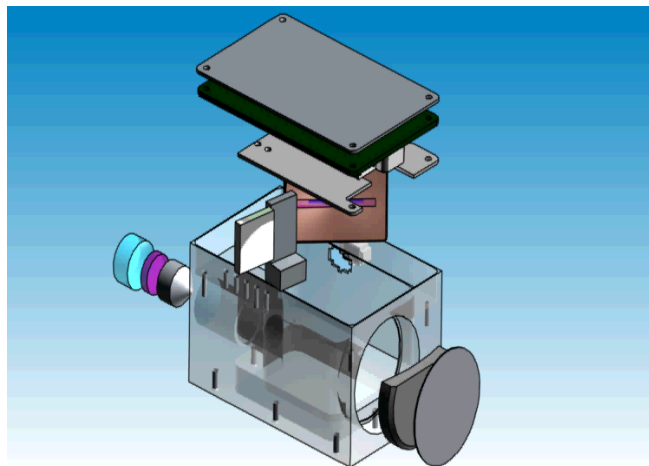
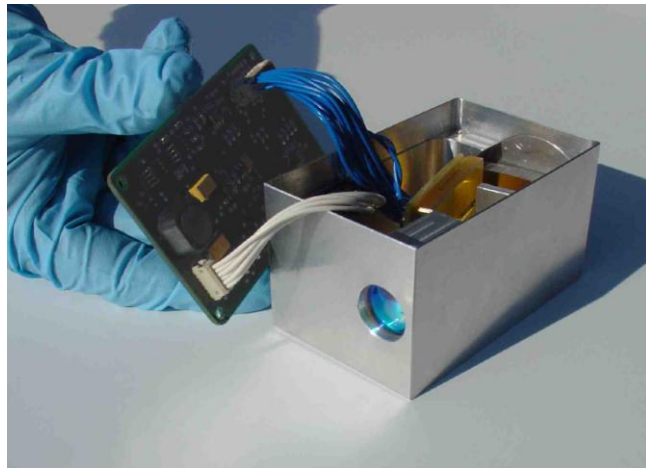


Fig. 12: Argus 1000 Spectrometer: (a) actual and (b) schematic representations.

output amplifiers are clamped to a DEADPOT potential of 3.25V supplied by external circuitry. LSYNC is generated by the user, other lines are generated internally.



Fig.14: Detector line sequence.

The typical device quantum efficiency of the raw detector is shown in Fig. 15. The array has a quantum efficiency of more than 80% between 1000 nm and 1600 nm.

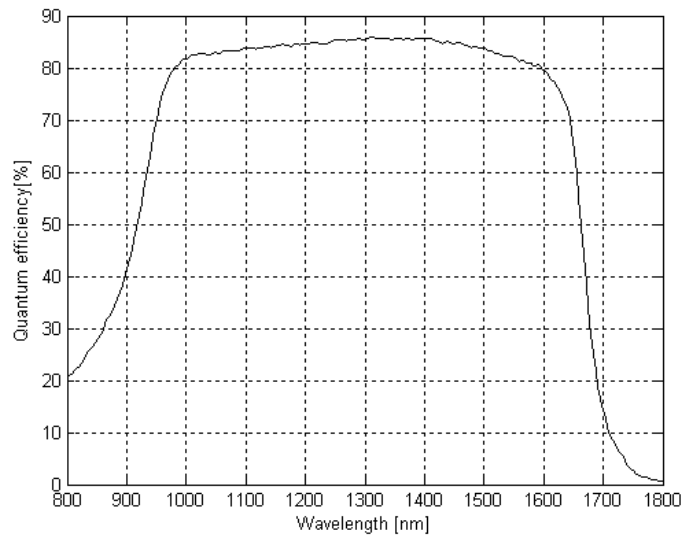


Fig. 15: Detector Quantum Efficiency (data from detector data sheet).

3.2 Optical Design

As an instrument to measure nadir Earth emission from space, the design criteria behind Argus included small size, mass, optical resolution and spectral range, and budgetary considerations. The fundamental components of any spectrometer include an entrance slit, a form of input illumination (in this case sunlight reflected by the Earth, absorbed by atmosphere), a method for discrimination of different spectral frequencies (for example a prism, etalon, diffraction or interference grating), and a method of focusing radiation onto a detector or eyepiece.

The wavelength range of the Argus spectrometer was based on a desire to observe at relatively high resolution (approximately 6 nm) Earth emission in the NIR. The wavelength and resolution requirements limited our choices of gratings (for resolution: lines per mm) and detectors. Gratings elements are given in units of lines/millimeter (l/mm) or grooves/mm, which determine the resolution of the spectrometer along with other factors such as focal length. The higher the l/mm value is the higher the resolution. Our choice of grating type was dictated by desire to observe CO₂, H₂O and O₂. CO₂ has an absorption at 1570-1580 nm and 1600 -1620 nm, where other gases do not absorb. CH₄ is a major absorber around 1640-1675 nm, although this signal is contaminated somewhat by CO₂ and H₂O at 6 nm. Carbon dioxide has three main vibrational bands in the infrared centered at 1400-1420 nm, 1580-1620 nm and 2240-2260 nm, but the 2240-2260 nm band is outside the range of current Argus infrared sensors and therefore is not considered here. The 1400-1420 nm band overlaps with the H₂O main vibrational band centered at 1400nm and this contribution to the observed spectral radiance makes it

difficult to disentangle the concentration of CO₂ from that of the other interfering gas. The band 1580-1620 nm is used since there is no other significant absorption overlap with CO₂ in this region. The optical depth of a molecule depends upon concentration and absorption cross-section of the molecule. Fig. 16 illustrates the absorption cross-section for CO₂ and O₂ with data taken from Rothmann *et al.*, (2006) at 6 nm resolution for the wavelength ranging from 900 to 1700 nm.

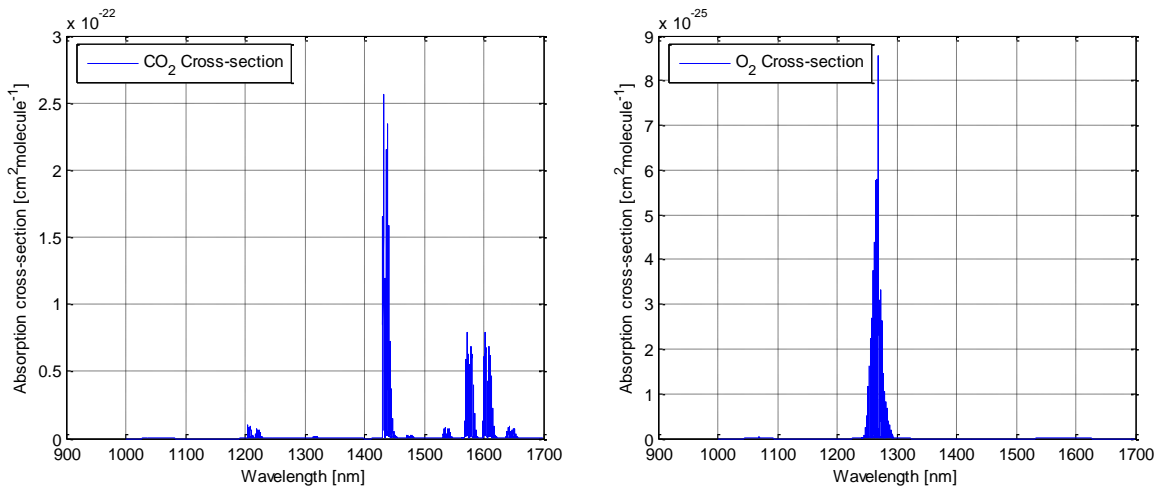


Fig. 16: Absorption cross-sections for CO₂, and O₂.

Fig. 17 shows the absorption cross-sections for H₂O and CH₄. Each atmospheric species has a unique absorption cross section spectrum, which is used widely to identify the species in atmospheric spectral measurements.

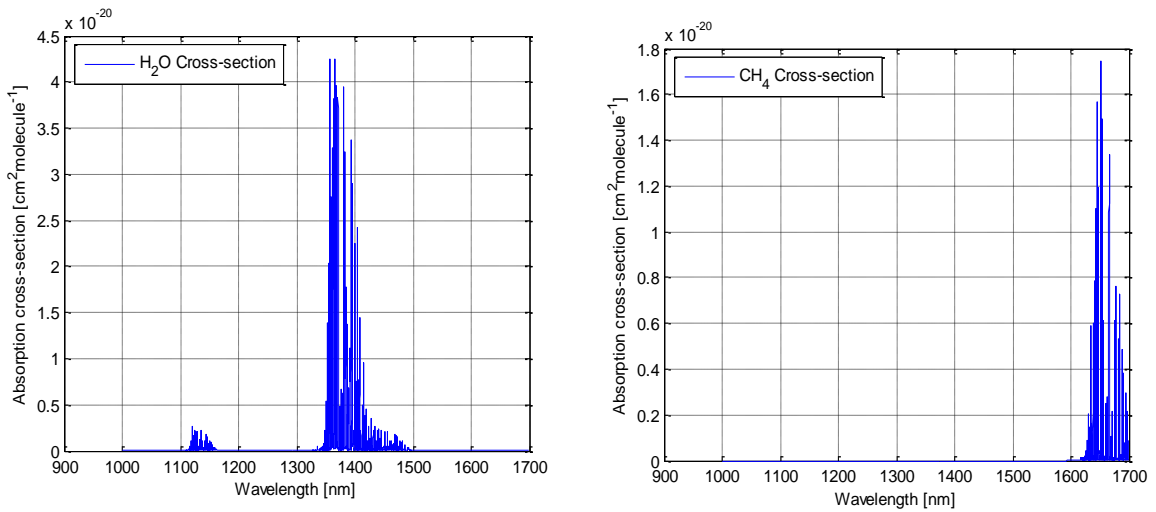


Fig. 17: Absorption cross-sections for H₂O, and CH₄.

The spectral sensitivity to these gas species is presented in Fig.18.

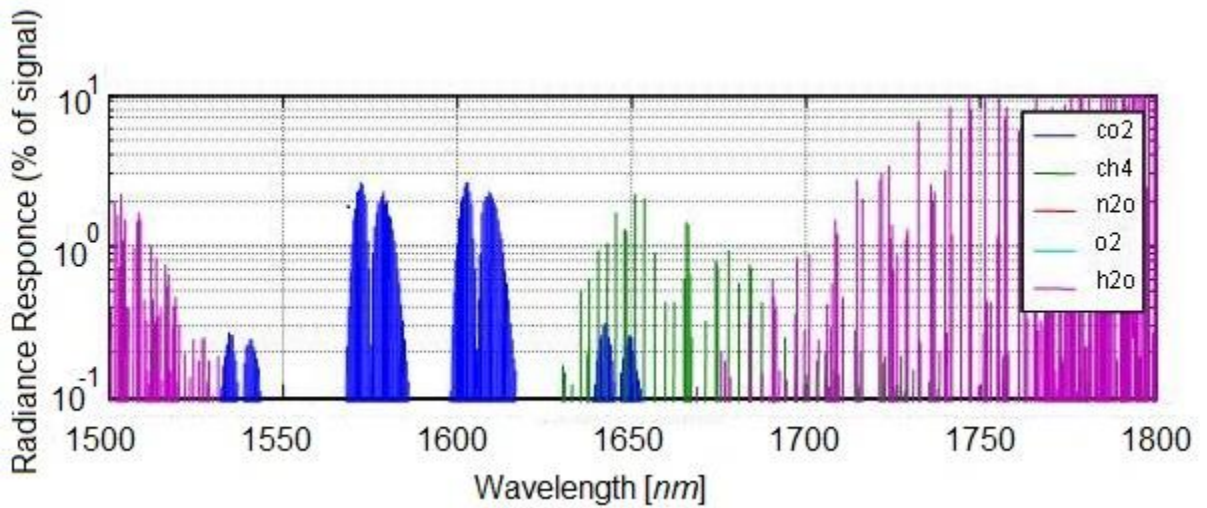


Fig 18: Sensitivity of upwelling radiance to a 1% change in concentration of the species shown in the legend. The figure was constructed using an atmosphere typical of June at 40N containing O₂, CO₂, N₂O, CH₄ and H₂O at typical volume mixing ratios and isotope values over 0-50 km altitude range. [Quine, B. M., private communication].

Trace gas species sometimes can be measured accurately with simple band-pass filter instruments tuned on and off absorption features. For example, the ozone (O_3) measuring Brewer has five pass-bands [Vanier and Wardle, 2006] and provides a global standard for ozone measurement instrumentation. Spectrometers and hyperspectral imagers can also be utilized for observations. Here, additional spectral channels provide more context on the radiative scene. Quine *et al.*, 2007 and Toohey *et al.*, 2007 have shown that the concentrations of up to six gas species can be retrieved from infrared spectra frequency modulated using a rotating constantly variable filter and collected by high-altitude balloon.

To individually discriminate spectral features, Wycisk *et al.* recommend as a guide, that the wavelength resolution of the spectrometer should be approximately 1/10 of the spectral band separation [Wycisk *et al.*, 2000]. Given that the two band-centre wavelengths of interest (CO_2 and CH_4) are 40 nm to 60 nm apart this empirical rule implies a need for a resolution of $5\text{ nm} \pm 1\text{ nm}$ for this range, and requiring a grating of several hundred lines/mm. The diffraction grating is an optical element that separates incident polychromatic radiation into its constituent wavelengths. The grating consists of series of equally spaced parallel grooves formed in a reflective coating deposited on a substrate and finished with a reflective gold coating. The dispersion of a grating is determined by the density of grating. We choose a 300 grooves/mm grating due to minimum light dispersion and to provide a free spectral range wide enough to obtain an O_2 feature and to provide for a broad observation of Earth emission 1000 nm to 1700 nm. Other options such as a 600 grove/mm gratings were modeled and tested experimentally.

The greater groove density was found to improve optical resolution but at the expense of a more truncated spectral range. These higher-resolution formats may be useful for future instrument derivatives however it was determined that for the CanX-2 mission a wider spectral range that included observation of the O₂ features was preferable to an enhanced spectral resolution.

Our optical design has a primary mirror of diameter of 35 mm in order to meet size constraints imposed by the spacecraft. A 15 mm diameter input beam (blue lines) has offset 13 mm from the mirror optical axis. The corresponding F- number is 2.0. The instrument utilizes a plane grating with 300 groves per mm in the second order to split infrared radiation by wavelength or frequency. The grating is offset by 15 mm from the mirror focal point towards the mirror.

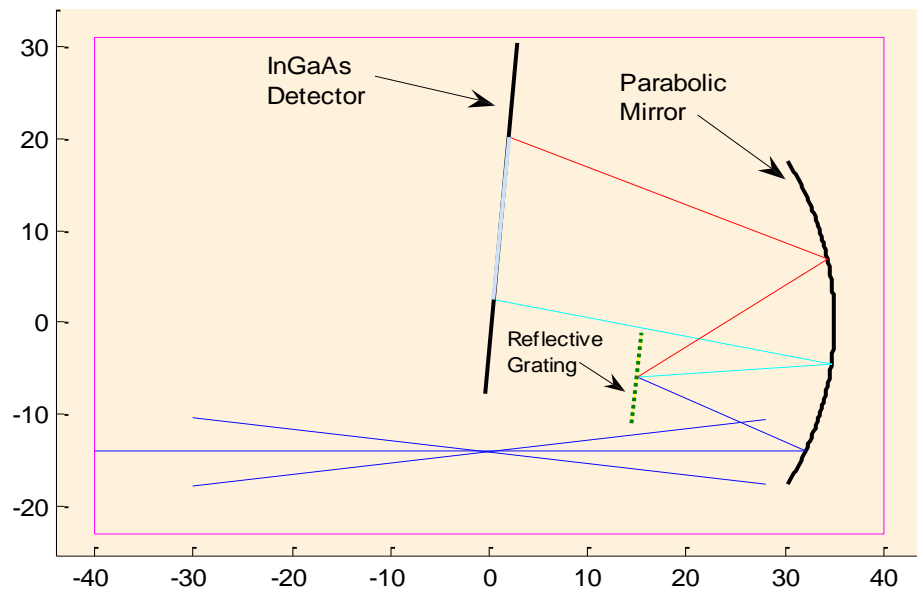


Fig. 19: Optical layout schematic (300 groves/mm), spectral range 900-1700 nm, 15 mm input optics, 35 mm main mirror.

The optical schematic layout generated using a MATLAB based Thoth Technology design tool is shown in Fig. 19. The simulation shows 900 nm (light blue line) and 1700 nm (red line) reflection paths.

3.3 Argus Interfaces

In this section the mechanical, electrical and command interface of Argus 1000 spectrometer are described.

3.3.1 Mechanical Interface

The dimensions and the mechanical axes of the Argus 1000 spectrometer are shown below in Fig. 20. The size of the package was determined by negotiation with the CanX-2 team and represents that largest volume that could be accommodated for the atmospheric science package.

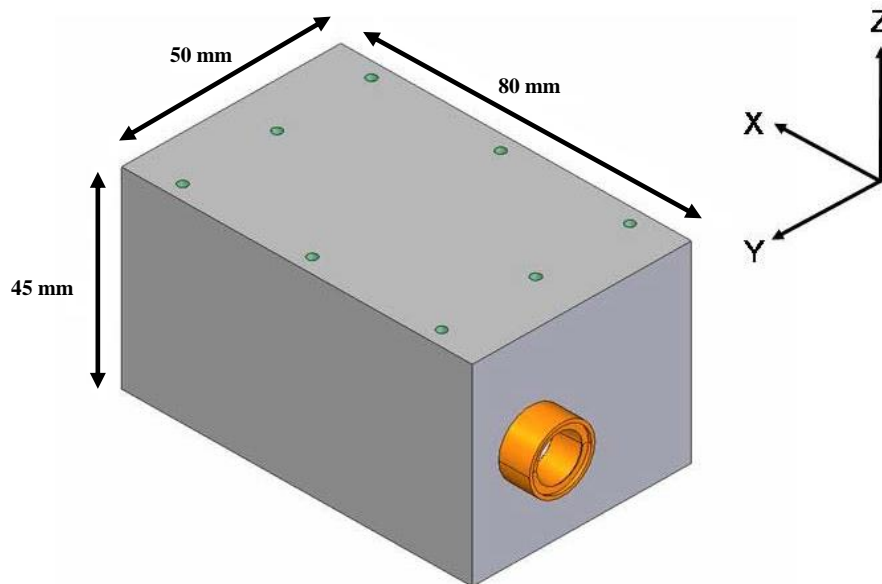


Fig. 20: Argus 1000 Spectrometer External Dimensions and Mechanical Axes (Argus User Manual, Thoth 2010).

3.3.2 Power Interface

Due to CanX-2 spacecraft power constraints, Argus may utilize a maximum continuous current feed of 572 mA delivered at between 3.5V and 5.2V, when the spectrometer is powered. This voltage is switched on and off by the main OBC. If the current drawn by the payload exceeds 572 mA, an over current circuit automatically switches off the instrument. Once triggered, the circuit can be commanded by a CanX-2 operator to reset it; however, such a reset is yet to be required in space operations. The spacecraft team is responsible to ensure that the power budget is maintained. This includes turning off the instrument if adequate power margins are not maintained. The instrument may be operated on a regime with maximum of 18 minutes a day activity during a scheduled data logging event day.

3.3.3 Communications Interface

The Argus 1000 features include two asynchronous serial ports with 3.0V TLL voltage levels (CanX-2 flight models). The protocol used to communicate between the instrument and both OBCs is RS-232 and the data format is 8N1 (eight bit characters, with one stop bit and no parity bit). On CanX-2 one serial port is connected to the main OBC and configured at 115,200 baud, 8 bits, one stop bit, and no parity. Commands are sent to the instrument from the main OBC through this port. The instrument also sends engineering data along with spectral data using this port. The second serial port is connected to the payload OBC and used by the instrument as a redundant means to send data to the payload OBC. The maximum data rate between the instrument and either

OBC is 230 kbps. The Argus electronics are designed to tolerate a constant logic high on its inputs, even when the unit was powered off. While Argus generates typically 21 kbps (assuming no co-adding and with an integration time of 102.4 ms), the maximum amount of data that can be stored aboard the CanX-2 satellite and downloaded is 500 KB per day (after data compression). This corresponds to approximately 6 minutes of Argus instrument operation.

3.3.4 Timing of Spectra Acquisition

Argus attains spectra for durations determined by the integration time setting. Once spectra are acquired they are transmitted in a subsequent 100 ms time slice. The number to be co-added scans setting can be set to between $n = 1$ and 9, the instrument acquires successive spectra co-adding them to a maximum precision of 16-bit before transmitting them in a subsequent 100 ms time slice.

3.3.5 Data Packet Format

On CanX-2 Argus provides data over a serial communications interface to an Onboard Computer in 532 byte unsigned 8-bit words. Following the timing described, data packets are transmitted continuously at a cycle period determined as (100 milliseconds + $T * \text{number of scans}$), where T is integration time setting. The electronics of the spectrometer also read the detector thermistor resistance and record this data with every spectrum. The thermistor reading is converted to a temperature in °C according to a simple conversion algorithm shown in Table 7 below [adapted from the Argus Owners

Manual, Thoth Technology, 2010]. Subsequent flight units have larger packet counts of 536.

Table 7: Argus 1000 Data Packet Format (CanX-2 flight models).

Word Number	Description
1-5	Synchronization Characters ‘(‘ and ’)’ provided to indicate packet start
6-7	Command acknowledgement and errors provided in two-character format: [6] [7] (see section 2.2).
8-11	Frame or Packet counter/ID computed as: [8]x(256 ²)+[10]x(256)+[11].
12	Integration time for exposure in seconds computed as: 2 ⁹ [9] x 0.0002.
13	Number of scans to co-added before data transmission.
14	8-bit binary word comprising; [11 Bit 1] Cooler Temperature Setting 0 = High Temp., 1 = Low Temp. [11 Bit 2] Dynamic Range Setting 0 = High Sensitivity, 1 = High Dynamic Range. [11 Bit 3] Auto-exposure Time Setting 0 = mode OFF, 1 = mode ON.
15-16	Detector temperature (DT) computed in degrees Celsius as $V0=3.25*([15]*256+[16]./1023; Rtc=26.7e3*(3.22-V0)./(V0+1.78);$ $DT=1/(1.289e-3+2.3561e-4*\ln(Rtc)+9.4272e-8*(\ln(Rtc)^3));$
17-18	Lifetime power ups computed as: [17]*256+ [18].
19-531	Spectral data encoded as 512-bytes in repeating unsigned MSB and LSB 8-bit words [MSB]*256+ [LSB].
532	Parity word computed bitwise as $\Sigma (I=1\dots 531) \text{ XOR}(\text{byte}_i, \text{byte}_{i+1})$

3.3.6 Command format

Argus may be commanded using command string consisting of five bytes arranged as follows:

Header	Header	Parameter	Setting	Parity
--------	--------	-----------	---------	--------

The header is two bytes in length and is the characters ‘(, ’)’. The parity byte is the

logical XOR of the bytes making up the command string, excluding the parity byte. The commands which are passed on to the spectrometer are formatted in hexadecimal characters. Once the command is sent in Hex characters, Argus responds with a message, which demonstrates the command has been received and executed. If an error occurs during the command reception/execution process Argus will respond with an error message such as "Error due to Invalid parameter" or "Error due to scan count out of range" [Argus Owners Manual, Thoth Technology 2010].

3.3.7 Argus Commands

The following sections describe the commands that may be passed to Argus while it is operating. The instrument team designs scripts that configure Argus for operation at initialization for a particular observation. Configurations can also be programmed into the instrument for observation sequences requiring the same operating parameters.

3.3.7.1 Exposure Time

The exposure time settings range is between 200 μ s to 6.458 s. The selection of exposure time is chosen according to the brightness of the source. In the laboratory during laser and radiance calibration, most of the results were obtained over a range of exposure times. However the space data results are obtained at higher exposure time with typical value ranges around 102.4 ms to 204.8ms. Longer integration times may be utilized to study strongly absorbing features and the expense of saturation at other wavelengths.

3.3.7.2 Capacitor Selection

There are two capacitor settings. The capacitance selection 0.4 pF is for high

sensitivity (low dynamic range) measurements while 10 pF is for regular measurements. Consequently, the majority of the space data measurements and calibration results are obtained at 10 pF.

3.3.7.3 Cooler Temperature Setting

The cooler temperature settings can be utilized either at high power or low power mode. In case of high power mode the current supplying the Peltier cooler is 100 mA, whereas for the in case of low power mode it is fed with 30 mA.

3.3.7.4 Scan Count

The number of spectra co-added or counted together before data transmission may range from 1-9. The typical value used for the scan count for the space data obtained is either 1 or 2.

3.3.7.5 Auto-exposure

The auto-exposure setting is used for the automatic setting of the exposure time settings. Mostly for the space data collection, the auto exposure command is turned OFF as the timing of data is more difficult to determine from data returned in current instrument telemetry.

3.3.8 Connectors

The Argus spacecraft connector is located on the -Y face of the instrument. The instrument has a bulkhead mounted Hirose DF13 type connector with 6 pins. The instrument connectors supply the external power and communication lines.

4.0 SPECTROMETER CALIBRATION METHODOLOGY

The Argus 1000 on-board CanX-2 is calibrated in a three-step process, described previously in Jagpal *et al.*, [2010]. The following sections describe the wavelength, radiance and gas absorption calibration methodologies.

4.1 Wavelength Calibration

First, a wavelength calibration is conducted using five infrared lasers. Fig. 21 shows the calibration setup with an IR laser source, which passes through collimator optics that fills the instrument's instantaneous field of view (IFOV). This simulates radiation emitted by a ground tile and received by the spectrometer. The spectrometer is mounted on an adjustable vernier kinematics mount with five degrees of freedom.

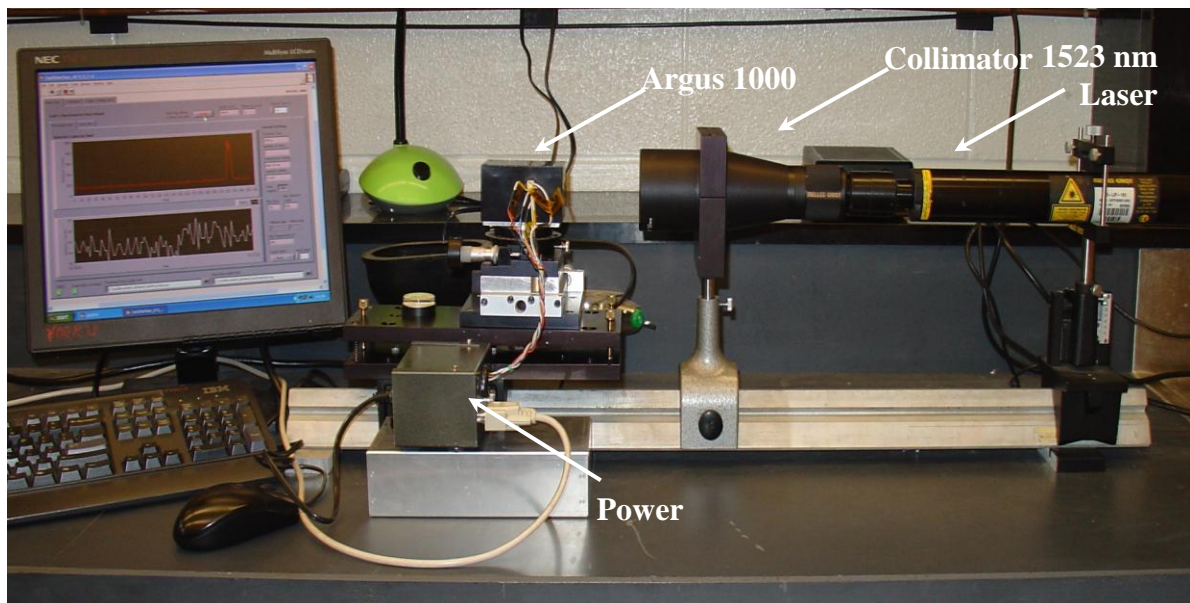


Fig. 21: Setup for wavelength calibration of the Argus 1000 spectrometer.

Table 8 shows the type, centre frequency and make of all these five lasers.

Table 8: Laser types used for calibration.

Centre Frequency	Type	Make
969 nm	Diode	Delta Photonics
1064 nm	Semiconductor laser	GMF-1064-XFYCZ
1150 nm	Gas	Melles Griot
1265 nm	Diode	EOSI
1523 nm	Gas	Melles Griot

4.2 Radiance Calibration

Following wavelength calibration, the device is calibrated for absolute radiometric accuracy using a calibrated standard illumination source, mounted at the distance of (0.5 ± 0.001) m in front of the white screen. A schematic for the setup is shown in Fig. 22 [Walker *et al.*, 1987]. The circular aperture is needed to cut out stray light.

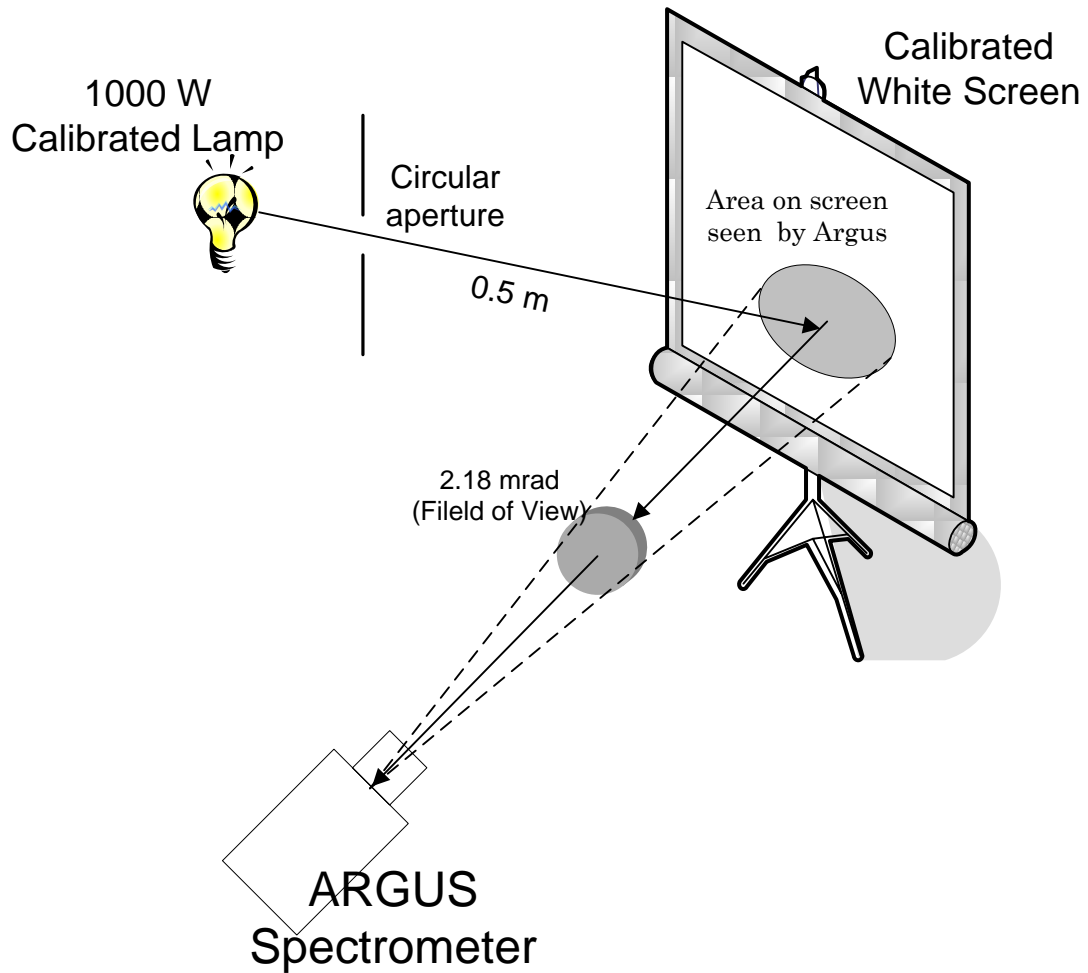


Fig. 22: Block diagram for radiance calibration of Argus 1000.

The white screen used in this experiment is an ORIEL SRT 99-120 (Calibration Report Number 33251-1-1). The National Laboratory Traceable Standard is SRS-99-020-REFL-48 (NIST). The mean value and standard deviation of the reflectance factor for the white tile are 0.9877 and 0.0141, respectively. Lamp irradiance is computed as

$$Y = \frac{1}{\lambda^5} \exp\left(A + \frac{B}{\lambda}\right) \times \left(C + \frac{D}{\lambda} + \frac{E}{\lambda^2} + \frac{F}{\lambda^3} + \frac{G}{\lambda^4} + \frac{H}{\lambda^5}\right), \quad (1)$$

where Y is the spectral irradiance of the etalon lamp measured in SI units $[\text{mW m}^{-2} \text{nm}^{-1}]$,

λ is the wavelength covering the spectrometer range from 900 to 1700 nm, ,
 $A = 4.46057 \times 10^1$, $B = -4.61546 \times 10^3$, $C = 1.01797 \times 10^0$, $D = -3.57175 \times 10^2$,
 $E = 6.08109 \times 10^5$, $F = -3.43963 \times 10^8$, $G = 8.2966 \times 10^{10}$, and
 $H = -7.52124 \times 10^{12}$. The calibration constants are determined with reference to NIST
traceable standard for the 10^3 watt calibrated lamp ORIEL (Model 63350), which was
used in this radiance calibration [Suemnich *et al.*, 1998].

The radiant power in SI units [W] entering into the spectrometer can be
computed by following equation

$$P = 0.989 \frac{Y \Omega A \Delta \lambda_{pixel}}{\pi} \quad (2)$$

where $A = \pi r^2$ and $r = 0.0075$ m are the area and radius of the spectrometer lens,
respectively, Ω is the solid angle and $\Delta \lambda_{pixel}$ is the pixel in nm. Fig. 23 shows the
reflectance factor as a function of wavelength for the white screen using this data.

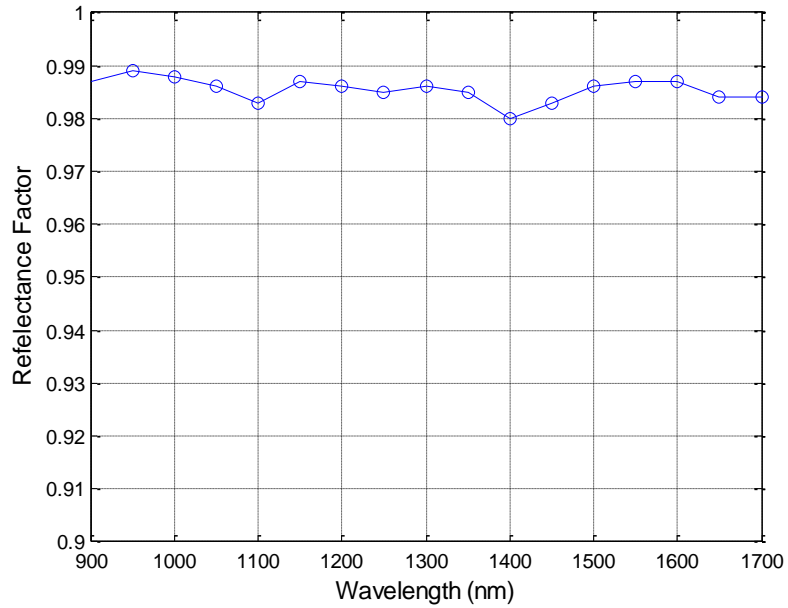


Fig. 23: Hemispherical spectral reflectance of white tile for calibration of Argus 1000 micro-spectrometer.

4.3 Gas Absorption Calibration

Absorption by a gas cell containing carbon-dioxide was measured in order to validate the radiant response of the instrument to gas absorbers. The setup for absorption measurements of the gases consists of a 1-m long glass cell that is flushed continuously with CO₂ at approximately standard temperature and pressure conditions as shown schematically in Fig. 24. The cell when containing 100% CO₂ gas at one atmosphere has a linear number density of CO₂ that is computed using GENSPECT as equivalent to a 2.604 km atmospheric ground level path for the June 40° latitude 1971 standard US atmosphere [McKernan, *et al.*, 1999].

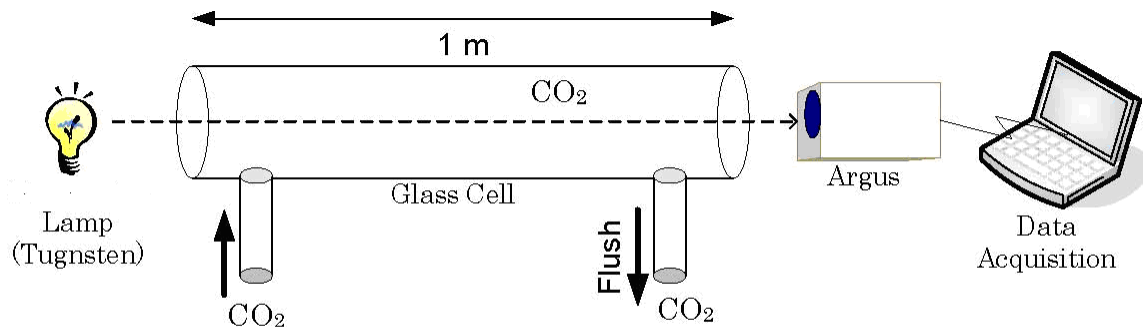


Fig. 24: CO₂ absorption measurement set up.

As the scale height of the Earth's atmosphere is 8.5 km (assuming a temperature of 290 K) and reflected solar radiation must pass through the atmosphere twice, the 1-m cell provides a sensitive means to validate response to carbon dioxide column amount with the optical depth inside the gas cell with CO₂ comparable to approximately 15 % to that of the real atmosphere.

In order to see the comparison between experimental measurement and theoretical data, a MATLAB code to simulate the radiative transfer process of light passing through the laboratory setup is used. The code computes the radiation emission and transfer path over a large grid of spectral points, accounting the absorption and emission processes resulting from the cumulative line spectra of the gas at each spectral interval. The process for obtaining the synthetic detector counts from radiance results is shown schematically in flow-chart in Fig. 25.

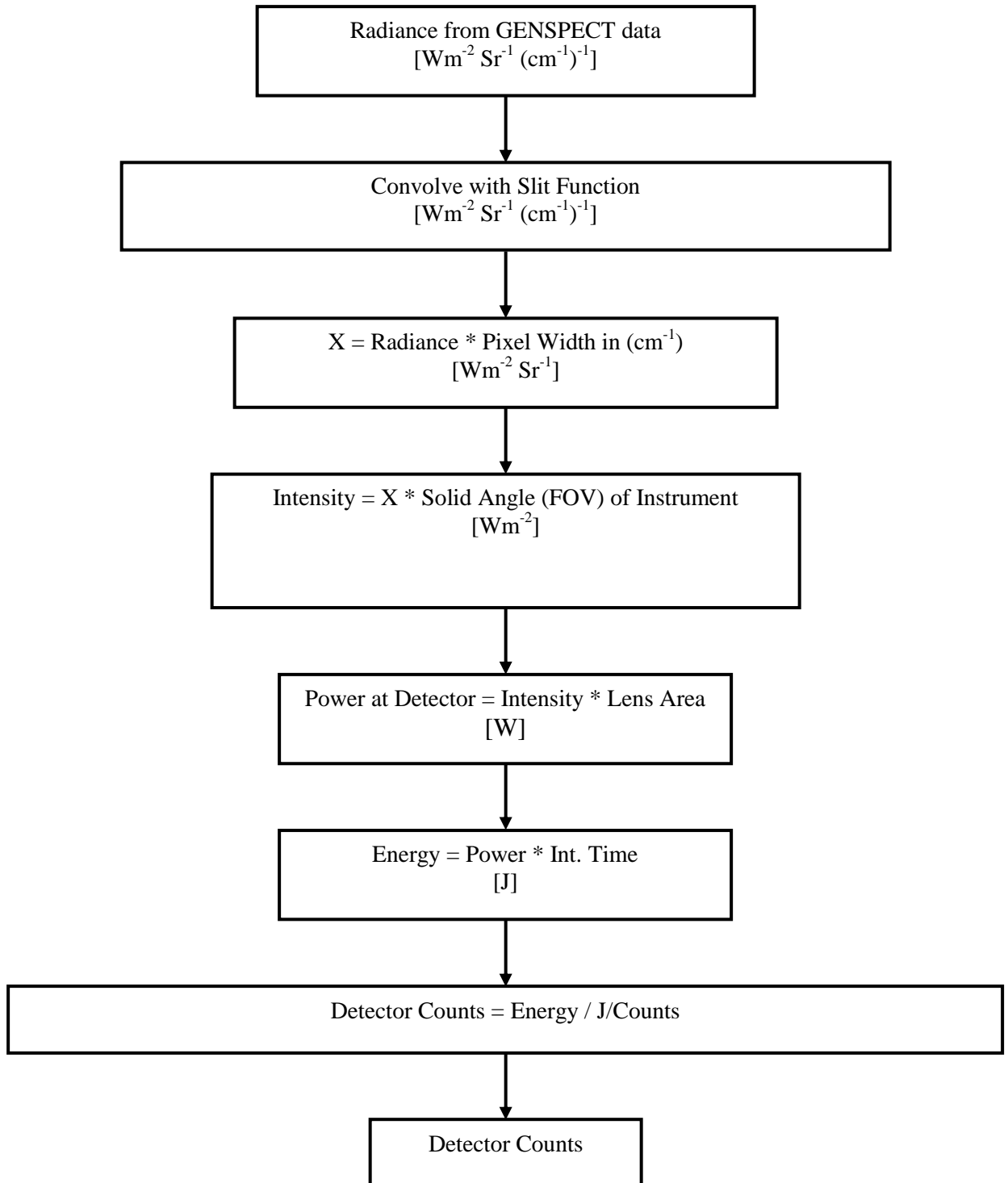


Fig. 25: Flow-chart for conversion of synthetic radiance into detector counts.

The synthetic detector counts and radiative transfer results presented in this thesis are generated using the HITRAN database [Rothmann *et al.*, 2004] and the spectral simulator GENSPECT, [Quine and Drummond, 2001]. The toolbox contains the basic functions required for line-by-line code computation of massive input data with selectable interpolation error tolerance as well as the radiation transfer functions needed to convert spectral radiance into instrumental counts. This toolbox was utilized to analyze Argus calibration data as well as space data from CanX-2 and is discussed further in section 4.7.3.

4.4 Space Qualification Testing

In order to examine and certify that the instrument is robust enough to withstand the events during and after launch, and subsequent reliable operation in space environment, Argus was successfully subjected to a comprehensive set of instrument and spacecraft qualification tests in the laboratory. These are described in the next two subsections.

4.4.1 Vibration Testing

Vibration testing is necessary to determine how Argus hardware, structure, and functionality would react to the launch loads. Both, low and high levels of sinusoidal testing up to 10.0 g loads at the frequency range 20-2000 Hz were performed. In addition, random vibration test up to 7.5 g within the same frequency range were conducted on Argus flight and flight space models for CanX-2. To ensure that Argus can withstand any positional configuration inside the launching vehicle, vibrations tests were carried out in

both longitudinal as well as vertical modes. Fig. 26 illustrates the vibration test facility at York University. The accelerometer is attached on the vibration mount (near the front lens of the spectrometer).

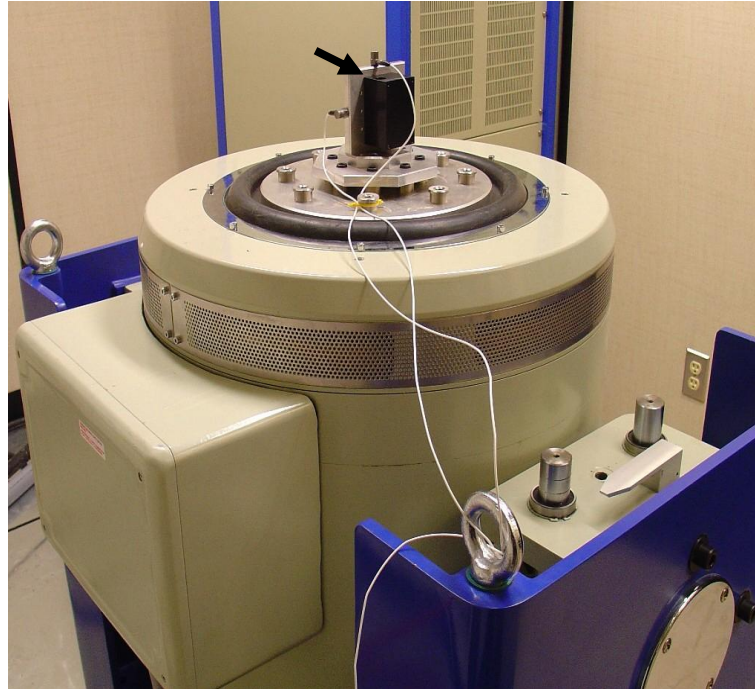


Fig. 26: Argus, (shown by arrow), is attached to the vibration system at York University, Toronto.

4.4.2 Thermal Vacuum Test

In low Earth orbit, the instrument is periodically exposed to the sunlight and the shade of the Earth multiple times in the span of 24 hours. Thus the spectrometer is expected to experience temperature variations. In order to analyze the behavior of the instrument over broad temperature changes, a thermal vacuum test was performed over a 72 hour period. The primary purpose of the thermal vacuum test was to verify reliable

operation of the electronics and optics used in Argus. The secondary purpose of the test was to verify component operation over a wide temperature range that includes the extremes of thermal environmental conditions that might be experienced during the CanX-2 flight.

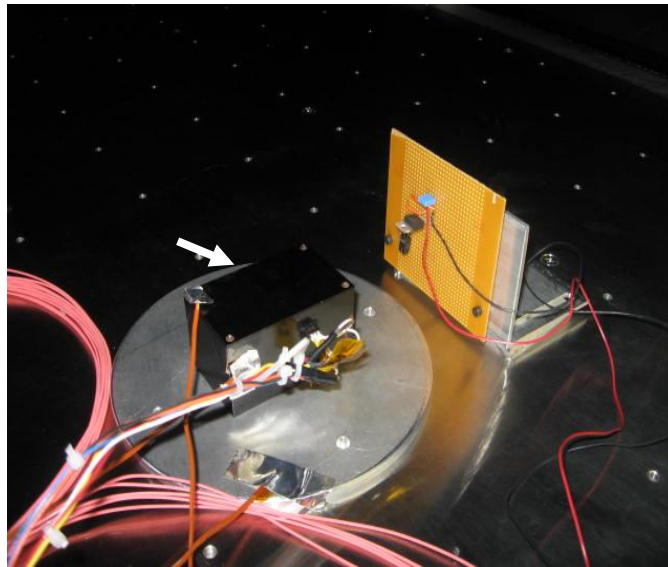


Fig. 27: Argus 1000 (shown by arrow) is attached for thermal vacuum test setup.

Fig. 27 shows the thermal vacuum test setup for Argus with an external current-regulated circuit for IR light emitting diode (LED), which enabled us to observe the variation in detector counts as a function of temperature. On day one the thermal vacuum test was performed, the ambient temperature was 25°C. On day two it was continued at a hot soak temperature of 60°C. On day three, the thermal vacuum test was completed at -50 °C cold soak. The instrument and chamber temperatures were recorded using type-K thermocouples attached at the various positions on the test article and fixtures. One thermocouple was fixed on top of Argus while others were attached to the base plate

close to the both sides of the instrument. In order to avoid the direct contact with chamber chassis, we applied an electrically isolated interface between the thermocouple and plate surface.

4.5 Geolocation of Argus data

The basic geolocation software for Argus 1000 spectrometer was developed using North American Aerospace Defense Command (NORAD) two-line element sets that consist of two 69-character lines of data which can be used together with NORAD's SGP4/SDP4 (Simplified General Perturbations Satellite Orbit Model 4) orbital model to determine the position and velocity of a satellite. Attitude quaternion and Earth orientation parameters are also used to calculate other parameters such as nadir angle, latitude, longitude, and solar angle at every time step of an Argus dataset where attitude information is available. This work was conducted in collaboration with Prof. Hugh Chesser and Prof. Regina Lee who developed geolocation algorithms for Argus data assimilation using the STK (Satellite Tool Kit) toolbox and in MATLAB.

4.5.1 Satellite Coordinate system

The coordinate of the CanX-2 spacecraft is analyzed using three frames of reference: Earth-centered inertial (ECI) frame, Earth-centered Earth-fixed (ECEF) frame, Spacecraft Body Frame. The brief explanation of this coordinate system is given in the following sections.

4.5.1.1 Earth-centered inertial (ECI) frame

The ECI frame is a convenient inertial frame for which Newton's second law is valid, and thus this frame is widely applied for determination of the spacecraft position, velocity and attitude. By convention, the x -axis of ECI frame is taken along the vernal equinox of epoch, the z -axis is directed along Earth axis of rotation and the y -axis is defined according to the right handed system.

4.5.1.2 Earth-centered Earth-fixed (ECEF) frame

ECEF is a Cartesian coordinate system used to identify the longitude and latitude of the Argus 1000 spectrometer foot print on Earth. By convention, the x -axis of ECEF frame is along the Greenwich meridian, from which the longitude is measured. The z -axis of ECEF coincides with the z -axis of ECI frame and the y -axis is also conventionally defined according to the right handed system.

4.5.1.3 Spacecraft Body Frame

The Argus 1000 spectrometer is mounted on the yz -plane (facing negative x -axis) of CanX-2 nanosatellite as shown Fig. 28. The y -axis of the body frame is along the minor axis of spin. Note that CanX-2 has a thruster that is on the same surface (facing $-x$ axis) as the spectrometer to induce the major axis spin. The attitude of the spacecraft is defined in quaternion that represents the rotation from ECI frame to the body frame [Wertz *et al.*, 2003]

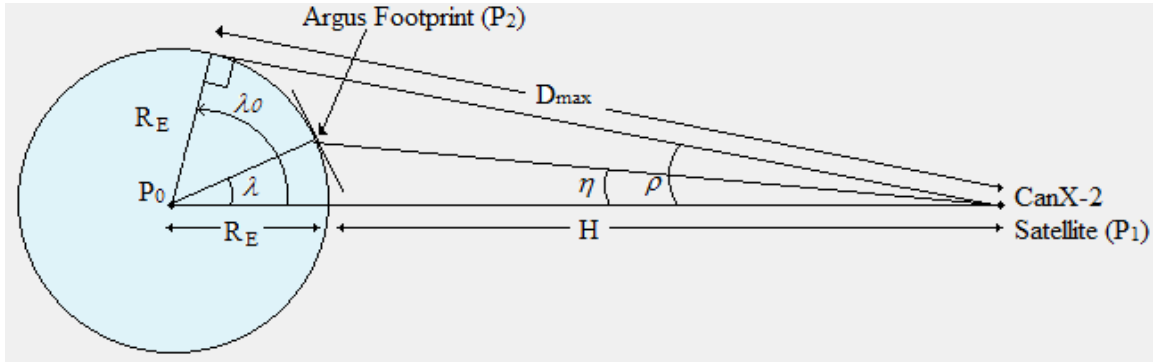


Fig. 28: Argus Footprint and Earth-Centered-Earth-Fixed frame determination.

The parameters in Fig. 28 as are as follows:

η = nadir angle, λ = Earth central angle, ρ =angular radius of Earth, λ_0 = angular radius measured at the centre of Earth, D_{\max} =Distance to the horizon, R_E =Radius of Earth, H = altitude of the satellite.

4.5.2 Satellite Attitude Determination

While the Argus spectrometer is collecting data, ideally, the spacecraft points nadir. The exact look angle of the instrument must be computed in order to provide precise targeting information. In addition to specified maneuvers, other factors effecting spacecraft dynamics are experienced that have to be accounted for in radiative transfer analysis. Attitude data is provided in as a time evolving quaternion 4-vector form by the CanX-2 team for correlation with Argus data.

4.5.2.1 Geolocating the Argus Footprint

The geolocation of Argus data is determined by first determining the CanX-2 ground track and then applying the attitude information to compute the instrument look

angle and footprint geolocation. A ground track or sub-satellite point is the path on the surface of the Earth directly below a spacecraft. It is the projection of the satellite's orbit onto the planetary surface. For the purpose of this thesis, we can modify conveniently this definition to be the set of points on the Earth that negative x -axis of the CanX-2 spacecraft intersects. In other words, if the spacecraft maintains nadir pointing during an observation, the ground track would be the precise location on the Earth where the observation would be made.

The actual footprint or tile that Argus measures on the Earth is corrected for the orientation of the spacecraft at the moment of each observation. Observation where the nadir angle (η) is less than the corresponding arc radius of the Earth (ρ) will return scientific data, however, good datasets have nadir angles less than $\pm 20^\circ$.

4.5.3 Correlation CanX-2 geolocation information with Argus Data

Attitude and control is provided by the by the CanX-2 nanosatellite platform. Attitude estimates are provided to the Argus science team at sixty-second intervals. The attitude data is interpolated to estimate the attitude for each observation profile [Sarda *et al.*, 2008].

In order to compute the precise location of the Argus footprint (P_2), we first compute the position of the spacecraft (P_1) using the latest Two-Line-Elements (TLE) and Simplified General Perturbations Satellite Orbit Model 4 (SGP4) propagator. The orientation of the spacecraft with respect to the inertial frame is estimated in three dimensions. The quaternion values obtained during the observation are first converted into a rotation matrix from the body to inertial frame (C_{ib}) then the instrument axis $(-1,$

0, 0) is multiplied to calculate the instrument pointing vector (defined as $\mathbf{P}_{12} = \mathbf{P}_2 - \mathbf{P}_1$) in the inertial frame [Chesser *et al.*, 2009]. Ultimately, the nadir angle (η) can be found as the angle between \mathbf{P}_{12} and \mathbf{P}_2 .

\mathbf{P}_2 is computed using simple geometry on the assumption that $|\mathbf{P}_2| = \text{arc radius of the Earth}$. The coordinates of both \mathbf{P}_1 and \mathbf{P}_2 are then converted to the Earth-Centered-Earth-Fixed frame and the corresponding longitude and latitudes are calculated according to Fig. 28. Also as a reference, the angle between \mathbf{P}_{12} and the Sun vector is computed. Finally, this Sun angle (denoted as β) is also accounted for in radiative transfer path analysis.

4.6 Observation Timing and Location Methodology

Argus observations were available via CanX-2 telemetry (courtesy of the CanX-2 team) beginning June 2008. The first two month's of data obtained could not be used due to poor quality caused by technical issues with the satellite management and telemetry. The first good quality data were obtained in the month of the December 2008. More than 100 data sets have been obtained during this period, mostly over ocean surfaces. Some of these data sets locations are shown in world map along in Fig. 29 below.

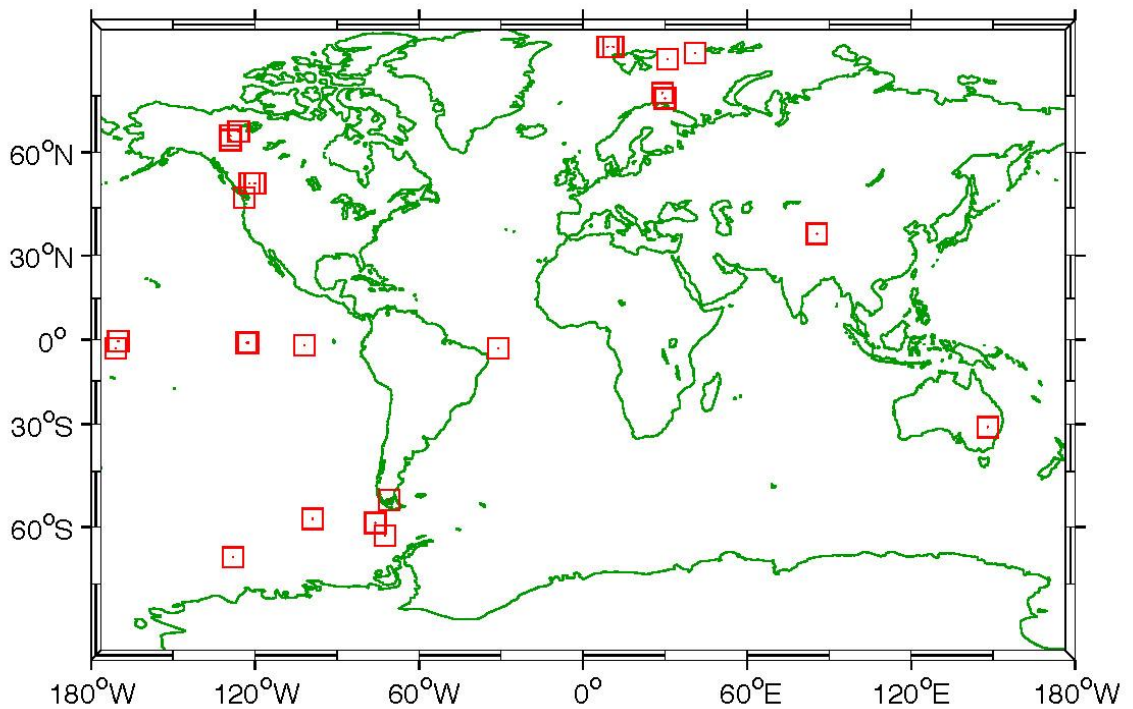


Fig. 29: September 2010, recorded Argus data (locations shown in red squares).

The Argus instrument on CanX-2 is operated in a time-sharing arrangement along with other spacecraft instruments and systems. The operation windows are typically of one month duration with an opportunity to schedule special observations to collect data over events of special scientific interest (forest fires, volcanism, oil spills). Currently ocean data is preferred as spectra are uncorrelated with ground albedo. The Argus science team has also targeted large cities in order to provide a catalogue of urban IR emissions. STK tools have been developed that automatically generate lists of desirable targets as well as a parameter weighting the importance of event that is utilized by CanX-2 spacecraft team to provided for effective observations campaigns with Argus. Table 9 shows the various data parameters for an actual space based observations.

Table 9: Typical Argus 1000 data parameters for a sampling of different profiles.

File Name	Packet Length	Capacitance [pF]	Scan Count	Max. Detector Count	Max/Min Chip Temperature, [°K]	Exposure Time, [ms]	Power Ups
2008May29_033135_2010000_0_129024.CX2MEM	239	10	2	71	286.8/281.5	1.6	844
2008June03_015314_2010000_0_253260.log	472	10	2	266	284.7/281.3	1.6	848
2008June03_133804_2010000_0_126252.CX2MEM	234	10	2	72	287.7/284.5	1.6	849
2008June03_134050_2010000_0_126504.CX2MEM	233	10	2	72	288.5/285.5	1.6	850
2008June03_165346_2010000_0_126504.CX2MEM	235	10	2	72	290.4/287.4	1.6	851
2008June09_020826_2010000_0_252756.CX2MEM	472	10	2	78	285.3/281.9	1.6	852
2008June09_021445_2010000_0_253008.CX2MEM	472	10	2	71	284.6/281.4	1.6	853
2008June09_135459_2010000_0_253008.CX2MEM	471	10	2	75	288.2/285.1	1.6	854
2008June09_135822_2010000_0_253008.CX2MEM	472	10	2	84	289.4/286.4	1.6	855
Spectrometer-20080905-032900-033130.CX2MEM	1108	10	2	69	286.8/283.5	1.6	870
Spectrometer-20080923-032900-033130.CX2MEM	141	10	2	79	288.5/284.8	102.4	871
Spectrometer-20080927-030800-031300.CX2MEM	1961	0.4	2	78	288.7/285.5	102.4	873
Spectrometer-20081212-155557-160103.CX2MEM	181	10	2	1624	289.7/286.4	204.8	875
Spectrometer-20081212-155557-160103.CX2MEM	137	10	2	718	291.4/285.7	204.8	977
2010August13_160719_20100000_73080.CX2MEM	31	10	1	471	288.3/284.8	204.8	984
2010September15_163632_20100000_151704.CX2MEM	284	10	1	387	289.6/284.4	204.8	1004
2010September20_145626_20100000_155988.CX2MEM	292	10	1	477	289.2/285.1	204.8	1008
2010September21_164909_20120000_152712.CX2MEM	285	10	1	295	289.7/284.5	204.8	1012

As an example, the data file taken on September 20, 2010, shows us the packet length of 292 with the capacitance settings of 10pF, and scan count equal to 1 and having maximum detector count 477 with the chip temperature varies from 289.2 K to 285.1 K which indicates that the detector operating temperature using the Peltier cooling system. The exposure time used in this observation is 204.8 ms. Comparing initial set of data which are not useful the integration time is 1.6 ms. The power ups for this set of data is

1008 which indicates the number of times instrument has been powered. Argus 1000 observations for some successful profiles are presented and discussed in Chapter 5.

4.7 Overview of Radiative Transfer and Forward Modeling

The spectral distribution of solar radiation, or extraterrestrial solar spectrum, incident on the top of the Earth's atmosphere is shown in Fig. 30. The interaction of this radiation with the surface and atmosphere is the source of the reflected radiation measured by Argus. The fraction of incoming radiation that is reflected back from the surface is partially a function of the atmospheric absorption and scattering processes [Armstrong *et al.*, 1972] but is also affected by the surface albedo. Absorption and scattering must be accounted for along the incoming and outgoing atmospheric paths that depend on the sun-Earth-satellite geometry includes solar zenith angle, satellite viewing angle and relative azimuth with respect to the point of observation.

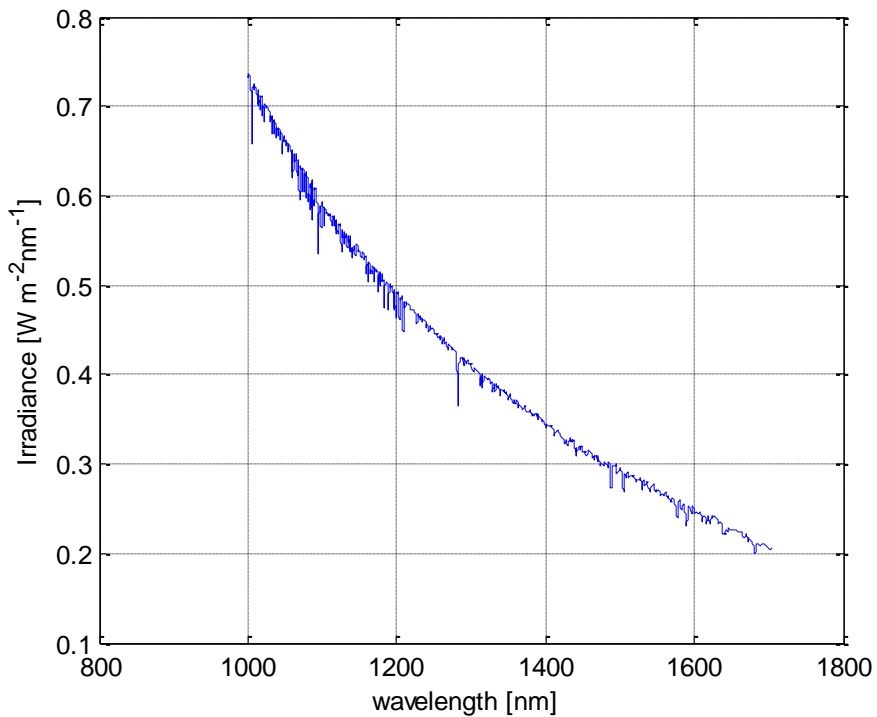


Fig. 30: Solar Spectrum for Argus spectral window Reproduced from the 2000
ASTM Standard Extraterrestrial Spectrum Reference E-490-00.

The absorption, emission and scattering of radiation by atmospheric molecules provide a means of identifying and measuring the composition of the atmosphere. There are four main methods in which electromagnetic (EM) radiation can interact with atmospheric gases. These methods are 1) ionization, 2) electronic transitions, 3) vibrational transitions, and 4) rotational transitions. The IR spectrum in a real gas typically contains many millions of molecular transitions. As a result of the combination of vibrational and rotational transitions, the gas retrieval of the measured spectra requires a sophisticated analysis, based on radiative transfer modeling. The gases CO_2 and H_2O

are the most important absorbers in the IR region observed by Argus [Buchwitz *et al.*, 2000a and 2000b].

Photons incident on a molecule undergo extinction by one of the two processes - absorption or scattering. A photon can also be emitted as thermal radiation. Solar radiation corresponding to UV, visible and NIR wavelengths comprises of approximately 99.1% of the total upwelling radiation in the wavelength region of interest, with thermally emitted photons comprising less than 1%.

The transport of energy, occurring as a result of the absorption and emission of photons is dependent on quantum state changes of the molecule. The electron is excited to the next higher orbital energy level in the process of absorption while the electron falls to a lower orbital energy level during process of emission.

Vibrational quantum change occurs in molecules with two or more atoms that can vibrate relative to each other. The bond between atoms behaves as a "spring" resisting any changes to the distances between two or more atoms. Rotational-Vibrational Quantum changes associated with the change in the angular momentum of the molecule are the predominant transitions observed in the IR region measured by Argus.

Fig. 31 shows the various processes as radiation crosses a gaseous medium. The first beam of radiation (a) does not interact with molecules. The second beam (b) undergoes extinction by scattering as the photon is scattered away from the original direction of the incident beam. The next beam (c) shows an example when the photon is completely absorbed by a molecule of the medium. The beam (d) is an example of multiple scattering whereby a beam is scattered once away from the original direction of

the incident beam but is scattered again by the second particle. Finally, beam (e) illustrates an example of EM radiation (secondary emission) from a particle after absorption from a previous photon.

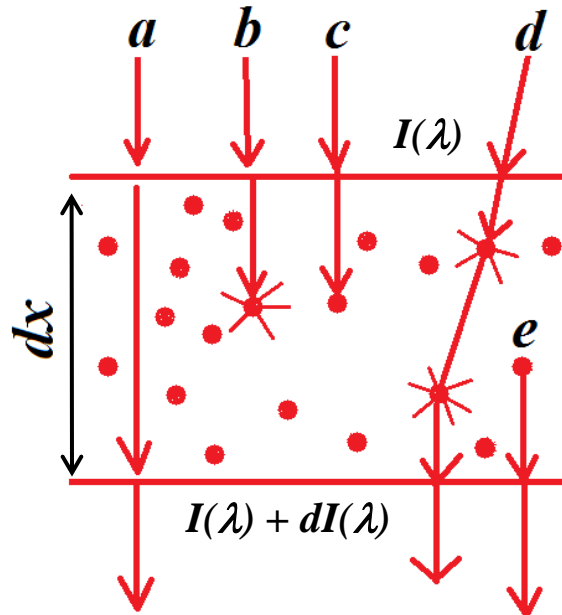


Fig. 31: Energy exchange processes occurring as radiation traverses a medium.

The absorption cross-section $\sigma(\lambda)$ describes the ability of a particular molecule to absorb a photon at a particular wavelength λ . Absorption cross-sections are associated with a particular atmospheric molecule and have units of area (m^2). The mass absorption cross-section $k(\lambda)$ is given in unit of area per mass ($\text{m}^2 \text{kg}^{-1}$). When the absorption cross-section is multiplied by the particle number density, its unit becomes (kg m^{-1}) whereas when the mass absorption cross-section is multiplied by the density the unit is (kg m^{-3}). The absorption cross-section is associated with the absorption coefficient with units of inverse length (m^{-1}).

4.7.1 Radiative Transfer Equations

If we denote the radiance as $I(\lambda)$, it becomes $I(\lambda) + dI_{ext.}(\lambda)$ after having travelled a thickness dx in (m) in the direction of its propagation, it follows by application of the Beer-Lambert law that

$$dI_{ext.}(\lambda) = -k(\lambda)\rho I(\lambda)dx \quad (3)$$

where $\rho(x)$ is the mass density of the material (kg m^{-3}) and $k(\lambda)$ is the mass extinction cross-section ($\text{m}^2 \text{kg}^{-1}$) for radiation of wavelength λ . The mass extinction cross-section is defined as a sum of the mass absorption and mass scattering cross-sections (represented by beam (b) and (c) in Fig.32). The term $dI_{ext.}(\lambda)$ is the decrease in radiance due to absorption by the material and due to scattering by the material. The negative sign shows that the radiance decreases as the beam passes through a medium. This radiance may also change due to emission from the material which may include multiple scattering from all other directions into the beam (shown by beams (d) and (e) in Fig. 31)

$$dI_{emis.}(\lambda) = j(\lambda)\rho dx. \quad (4)$$

The term $j(\lambda)$ is the emission coefficient. Combining equations (3) and (4), results in the equation of radiative transfer which is given by

$$dI(\lambda) = -k(\lambda)\rho I(\lambda)dx + j(\lambda)\rho dx. \quad (5)$$

The source function $J(\lambda)$ is the ratio of source function coefficient to the extinction coefficient, $J(\lambda) = \frac{j(\lambda)}{k(\lambda)}$. Equation (5) may thus be rearranged as

$$\frac{dI(\lambda)}{k(\lambda)\rho dx} = -I(\lambda) + J(\lambda) \quad (6)$$

where $J(\lambda)$ has units of radiance. Equation (6) is known as the general radiative transfer equation, fundamental to any radiative transfer process. This equation illustrates how a beam of radiation loses energy to the atmosphere by absorption and gains energy by atmospheric emission, and redistributes energy by scattering. If we assume that the atmosphere is plane-parallel (i.e. variations in the intensity and atmospheric parameters are allowed only in the vertical direction), then we can measure the depth of the atmosphere as distances along the normal to the plane of stratification of the atmosphere.

A beam of radiation traversing the atmosphere will experience a reduction of radiance due to absorption and scattering by the atmospheric species and an increase of radiance by emission from the atmospheric species plus scattering from other directions. The standard form of the equation of radiative transfer for plane-parallel atmospheres [Chandrasekhar, 1960] is:

$$\mu \frac{dI(\tau; \mu, \phi)}{d\tau} = I(\tau; \mu, \phi) - J(\tau; \mu, \phi), \quad (7)$$

where $\mu = \cos \theta$ (θ is the angle with respect to the normal of the plane of stratification and ϕ is the azimuth angle), and τ is the optical depth as a function of the vertical depth normal to the plane of stratification ($\tau = 0$ at top of atmosphere). $I(\tau; \mu, \phi)$ is the

intensity at depth τ , in the direction μ and ϕ , and $J(\tau; \mu, \phi)$ is the source function which contains terms due to multiple scattering as well as emission.

As there is, in general, no analytical solution to the equation except for simple cases, one way that it can be solved is numerically [Chedin *et al.*, 2002a]. In order to produce synthetic radiance profiles, it is necessary to devise a method to simulate the relevant optical properties of the Earth's atmosphere. A forward model provides expected (synthetic) radiance at the detector for a specified state of the atmosphere. Forward models are an important part of any retrieval or inverse-modeling process [Koner *et al.*, 2008]. The associated inverse problem provides a method to estimate the state of the atmosphere from measured radiances.

For the purposes of this study, and in common with approaches used by other instrument teams, transmission through clouds has not been considered, and a simple linear path model has been used. Consequently, retrievals are attempted on observed profiles where the presence of macroscopic clouds is visibly absent. Solar radiation passing through the atmosphere may be scattered by its constituents; this may take one of two forms: Rayleigh and Mie scattering. When the size of atmospheric particles with which the incoming radiation interacts is close to, or greater than, the wavelength of the radiation Mie scattering becomes significant, which is the case with aerosols and clouds. Rayleigh scattering describes the interaction of light with particles whose sizes are small compared to the wavelength of the radiation molecules in the atmosphere. For example, the optical depth due to Rayleigh scattering for the Earth's atmosphere from the surface to 4 km altitude at 1500 nm is approximately 0.00165 [Frohlich and Shaw, 1980]. The

effect is small and largely uniform over the Argus spectral range but is included in the analysis.

The most obvious way to accurately represent atmosphere change with height is to divide the atmosphere into a large number of thin homogeneous layers where the value assigned to each property of interest in each layer is equal to the value of that property in the real atmosphere at the height of the mass weighted mid-point of that layer, using the Curtis Godson approximation. A forty layer atmosphere with layer thickness of 2 km is utilized in this analysis.

4.7.2 Atmospheric Retrieval Methodologies

Several approaches have been used to retrieve trace gas concentrations from radiance spectra. They can be roughly grouped into four categories.

1. Optimal or Physical Retrievals

These use the forward calculation in an iterative process. The objective function is defined as the sum of squares of the difference between the simulated and measured spectra. The optimal retrieval is that which minimizes this objective function [Toohey *et al.*, 2007]. These use forward computation with full synthetic calculations which has the following advantages compared to the other retrievals:

- a) The residual provides a measure of the quality of determination.
- b) The method models directly the physics of line by line code from data derived from laboratory studies.
- c) The method provides a proper noise analysis.

- d) The method provides a means for a proper accounting of errors and uncertainty as parameters may be perturbed by their expected error and a worst-case analysis can be performed to quantify the effect of the uncertainty on the assimilated results.

2. Statistical Retrievals

These do not use radiative transfer equation directly. Instead, they rely on statistical relationships between ground- and space-based measurements. The method utilized is typically as follows:

- a) A training data set of ground-based measurements nearly coincident in time and space with the satellite soundings is compiled.
- b) This data set is used to calculate a statistical relationship between the satellite radiances and the radiosonde temperatures.
- c) These relationships are then applied to other radiances to retrieve temperature profiles.

This method can provide the most rapid retrieval results but is usually dependent on a more accurate radiative transfer treatment for validation.

3. Hybrid Retrievals

- a) These combine elements of physical and statistical retrievals. They do not require a large training data set and do use weighting functions.
- b) The Radiative Transfer Equation (RTE) is first initialized about a standard temperature profile and is converted into a matrix equation.

- c) This equation is used to obtain a matrix relating the temperature profile to the radiances, and including the weighting functions. A variety of optimisation approaches can be taken to solve the problem.

4. **Differential Optical Absorption Spectroscopy (DOAS)**

The basic principle used in DOAS to extract trace gas concentrations in the atmosphere or gas cells is by dividing spectral radiance collected under varying viewing geometries. Results are determined from the ratio of observations recorded at different zenith angles [Barkley *et al.*, 2006a and 2006c].

In the DOAS approach, effects that vary smoothly with wavelength including Rayleigh and Mie scattering are approximated by low order polynomials. Absorption cross-sections are then separated into a high (“differential”) and a low frequency part, the latter of which can also be included in the polynomial. This technique is commonly utilized in ground-based measurements where solar motion provides multiple data sets. As measurements that include observation noise are used as ratios, the technique can corrupt model assumptions leading to unexpected results in the presence of significant observation noise.

For this study, method (1) or physical retrieval has been utilized. This approach uses a forward model to output simulated radiance profiles. Firstly we computed the fraction of emitted radiation arising from different pressure levels (altitudes) at temperatures estimated for the Earth and the Sun. We also account for nadir angle for Argus and Solar Zenith angle in the calculation. Another major factor for the change in the value of radiance is albedo. The estimated albedo is adjusted recursively to match

with the experimental radiance. The RTE is then solved at each wave number to obtain the simulated radiance. This is convolved with the instrument's slit function and the radiance calibration is applied.

If the calculated radiances match the observed radiances within the typical noise levels of the spectrometer, then the current atmospheric profile (mixing ratio of the gases) is accepted. If the calculated and observed radiances do not agree, then the iterated (updated trial) profile is adjusted and the above steps are repeated. This method has the advantage that the process is transparent at each stage of the retrieval and no other database of coincident radiosonde data is needed. It is however computationally expensive.

4.7.3 The GENSPECT Radiative Transfer Model

GENSPECT uses a variable frequency grid to compute absorption parameters to a specified accuracy [Abrarov et al., 2010a and 2010b]. HITRAN line strengths [Duggan *et al.*, 1993] are pre-adjusted for normal isotopic abundances and tabulated, to model an Earth atmosphere with natural abundance.

Fig. 32 shows the typical GENSPECT computation points near line centre. The pre-computed points are denser near central part of the Voigt function [Abrarov *et al.*, 2009] and sparse at its wings where the points at the corresponding grids are linearly interpolated. After processing of all the required lines, the total absorption coefficient is derived by summation over all grids. Error tolerances provided by GENSPECT are 1%, 0.1%, and 0.01% [Quine and Drummond, 2001]. GENSPECT has been used to compute synthetic spectra for comparison with data collected by Earth observing instruments

deployed in the air, in space and on the ground including MOPITT-A, MOPITT, ACE-FTS, and MAESTRO.[see Quine *et al.*, 2007, Jounot and Drummond, 2002, McKernan, Quine and Drummond, 2002, Dufour *et al.*, 2006, Dufour *et al.*, 2005]. GENSPECT has also been used to simulate the radiative environment of Mars and Jupiter's moon Io [see Drummond *et al.*, 2002, Zhang *et al.*, 2003].

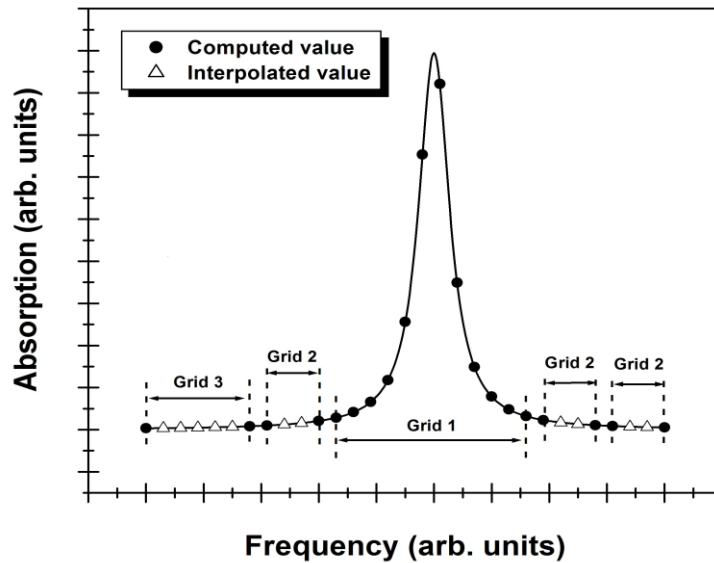


Fig. 32: Typical computation points near line centre.

Previous work [Quine *et al.*, 2005] introduced the use of a non-linear global optimization algorithm used to search for a global minimum by iteratively perturbing the full state vector of instrument parameters and trace gas species on the full vertical grid. While this technique produced reasonable results, it required large amounts of computing resources, and time. In order to produce results on a faster time scale a modified approach is used here.

An optimization routine is used to obtain a best fit between the simulated and measured spectra by adjusting the instrument parameters and trace gas amounts. The main advantage of this technique is the incorporation of instrument parameters into the retrieved state vector, which allows the analysis of flight data without pre- and post-calibration data. The main features of the retrieval algorithm are summarized below.

4.7.4 Instrument Slit Function

Every spectrometer has a unique instrument function or geometric slit function that defines the resolution of the device. Ideally, the size of the slit is infinitely narrow. Practically, however, the slit size cannot be too narrow due to the resulting decrease of the light intensity transmitted to the spectrometer detector inside the instrument and other physical limitations. As a result of the finite size of the slit, the slit function determines the spectral resolution as the spectral intensity distribution is distorted to some extent by the physical characteristics of the instrument. The spectral resolution was optimized to 6 nm and an individual slit function is computed for each spectral pixel.

For the inversion (retrieval) presented in this thesis, a two-sigma truncated Gaussian function [Quine, 2003] has been implemented, given by:

$$F(z) = \frac{1}{\sqrt{2\pi}} e^{-\frac{z^2}{2n^2}} \quad (8)$$

where z is the wave number.

4.7.5 Instrument Forward Model

The aim of the instrument forward model is to accurately simulate the true mapping between input radiance and detector response. While it is assumed that the

individual instruments are for the most part functionally identical, a few instrument parameters defining unique properties of each instrument are necessary, and are included in the forward model. Two parameters that define the value of the radiance obtained from the instrument are affected by selecting the different values of capacitance setting and exposure time.

For a nadir viewing instrument measuring, the atmospheric properties near the surface and surface reflectivity principally determine the nature of radiance profile measured by an instrument (except for absorption by certain species such as ozone). A single spectral line at a particular spectral position is fully characterized by its strength. The expression for the strength S (cm^{-1} molecule $^{-1}$ cm^{-2}) is given by

$$S(T) = S_0 Q(T) \exp(c_2 E_L (1/T_0 - 1/T)) \frac{1 - \exp(-c_2 \nu_0 / T)}{1 - \exp(-c_2 \nu_0 / T_0)}. \quad (9)$$

This term has temperature dependence where S_0 is the strength at room temperature, $Q(T)$ is the internal partition function ratio parameterized as a third order polynomial, E_L is the lower state energy (cm^{-1}), $c_2 = hc/k_B$, T is the temperature, and $T_0 = 298\text{ K}$ is room temperature [Quine and Drummond, 2001].

4.7.6 Retrieval Code and Library Functions

The main procedure to run the retrieval process is divided into three steps. The first step is to specify atmospheric mixing ratios and compute absorption coefficients for all the gases at all spectral points and heights using the MATLAB script *argus_atmosphere.m*. After successful running of this code, the absorption coefficients of all the gases in the “synthetic” atmosphere are obtained. The second step is to run the

argus_analyze.m module, which reads the raw Argus data, calibration, and background files. After execution of this code, we generate plots of counts as a function of wavelength and radiance as a function of wavelength. The next step matches this absolute radiance with the simulated radiance using the GENSPECT *argus_synthetic.m* module that outputs synthetic radiance. If this theoretical radiance does not match the experimental radiance, then we adjust the different variables (*e.g.* albedo) recursively until the theoretical radiance is a good agreement with the experimentally measured radiance.

The basic GENSPECT modeling [Quine and Drummand, 2002] runs the following library function files: *paths.m*, *path_source.m*, *path_atmosphere.m*, *path_reflect.m*, *atmospheric_cell.m*, *atmospheric_read.m*, and *cell_mixing_ratio.m*.

The *paths.m* function generates a viewing path through a set of gas cells using function cells. The path is a linear path through the set of gas cells (the order and cells used is determined by the start and stop altitudes) at a specified incidence angle. To generate the outputs the function calls on the structure cells and returns structure paths containing all the required information for radiance calculations. The *paths.m* function defines a path segment corresponding to a reflecting surface in the reflectivity of the Earth's surface. The *paths_radiance.m* calculates the radiance through a path. It uses library functions called *path_gas.m*, *path_source.m*, and *path_reflects.m* to form a path and generates the radiance after each path segment. Atmospheric cell generates a set of atmospheric cells that represent the atmosphere specified by structure atmosphere. Cells are divided on the basis of height as pressure increments according to choice of input

division. The function then performs the Curtis-Godson approximation and finds mean pressure, temperature, and number density values for each cell.

The *atmospheric_read.m* reads and saves out an atmospheric profile. The radiances obtained are given in the units ($\text{Wm}^{-2}\text{sr}^{-1}(\text{cm}^{-1})^{-1}$).

In order to implement the radiance vs. wavelength/wavenumber calculations, two script files, *argus_analyse.m* and *argus_synthetic.m* were developed. Some of the parameters (*e.g.* albedo) needed to be adjusted either manually or through optimization. The optimization was implemented through looping by consecutive increment/decrement of the corresponding parameter. If the difference between observation and synthetic mean values are smallest (the mean value is required as the radiance is wavelength dependent), the program interrupts calculation and returns the optimized parameter. Though this technique is efficient, the optimization is computationally expensive, especially when two or more parameters have to be adjusted. For instance, the computation time required for determination of only two parameters may vary from 30 min to 2 hours in a typical desktop computer. Once computed, the verification is performed to verify that the smallest error sum exists between observation and theoretical results.

4.8 Effect of Surface Albedo

To account for the total radiance measured at the Argus detector, the surface albedo must be estimated. The amount of reflected radiance from different surfaces is plotted as a function of wavelength. Initially, data taken over ocean has been preferred as the albedo is constant over the Argus spectral range as shown in Fig. 33. Analysis of albedo can also provide some limited estimate of ground cover.

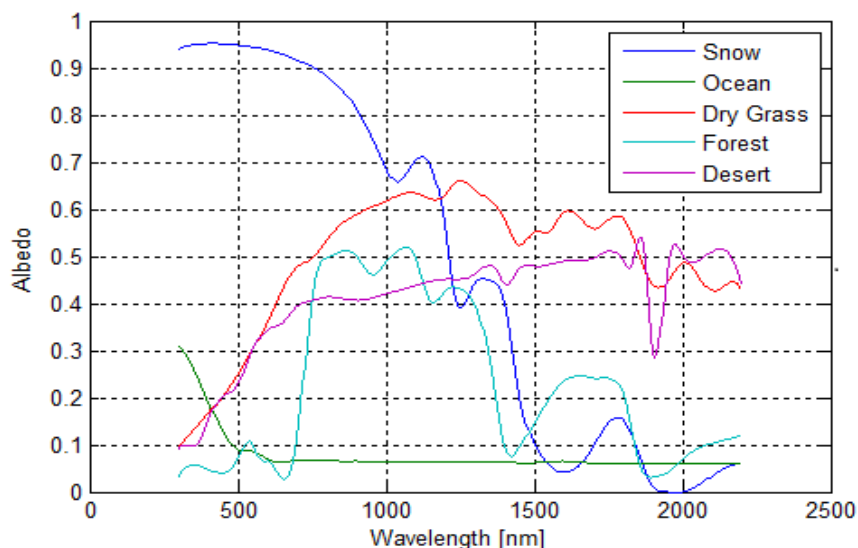


Fig. 33: Spectral signatures of some typical backgrounds encountered by Argus observations. Reproduced from the ASTER Spectral Library through the courtesy of the Jet Propulsion Laboratory, California Institute of Technology, Pasadena, California and the Digital Spectral Library 06 of the US Geological Survey.

Fig. 33 indicates that albedo for ocean is less than 7% between 1000 nm to 1700 nm where as other surfaces show high albedo values with more variability.

4.9 Cloud Process Method

At this time, the atmospheric impact due to multiple scattering within cloud is under development and has not been included in the current analysis. It is known that scattering by clouds can potentially introduce errors in the retrieved column amount of trace gases by modifying the radiation path length. Clouds (and other airborne particles) can either (a) scatter photons into the instrument FOV – which would have otherwise not

contributed to the additional radiance measured at the detector, (b) scatter photons away from the instrument FOV which would have contributed to the radiance measured at the detector, and (c) absorb or scatter sunlight back to space before it traverses downwards the full atmospheric column, precluding full-column CO₂ measurements in regions occupied by opaque clouds. Fig. 34 schematically describes this process.

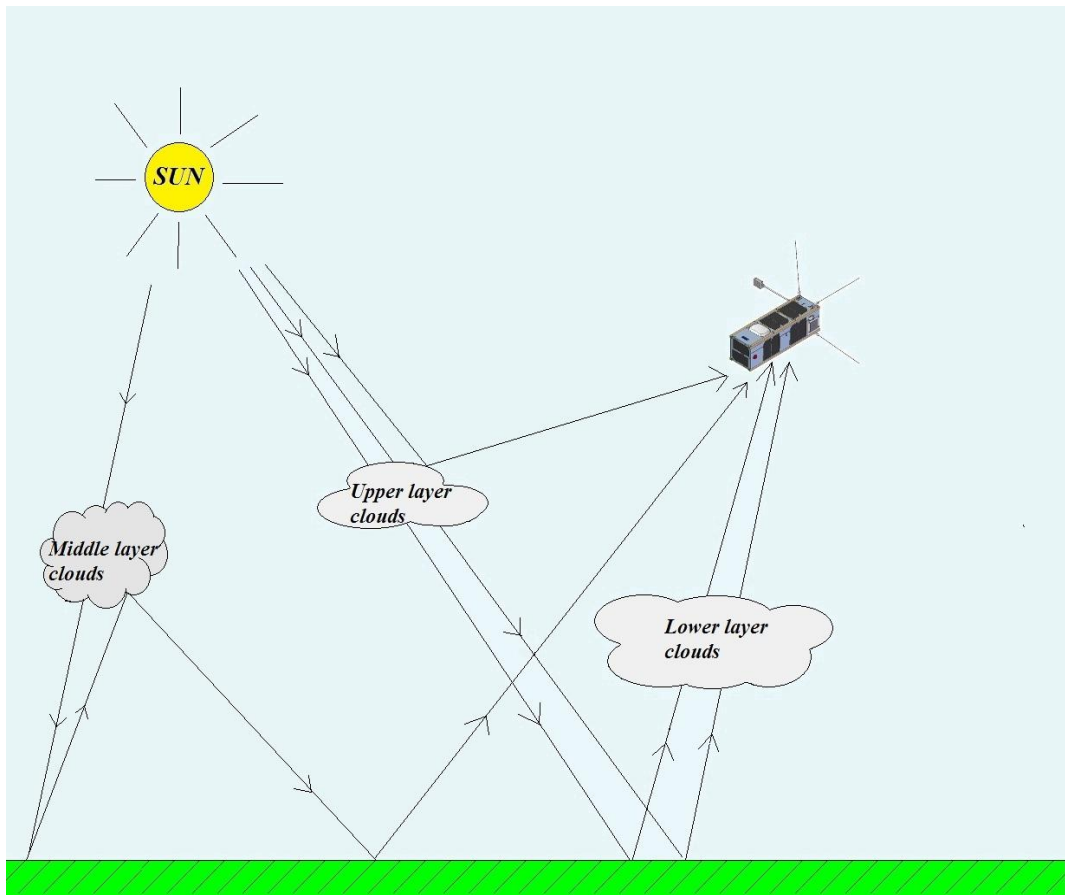


Fig. 34: Radiation path length through the clouds.

The current version of GENSPECT uses linear paths and photons that have undergone primarily single scattering. Because multiple scattering in the IR spectral region is not regarded to be as significant as in the shortwave spectral region, this

complex process is often simplified, or neglected, in most IR remote-sensing applications [Zhang *et al.*, 2007].

As a consequence of the higher albedo properties of clouds, we expect spectra partially or completely observed over clouds to be easily distinguishable from cloud free observations by the significant enhancement of total radiance in cloudy scenes. Further, observations where significant portions of photons reflected directly off cloud tops will exhibit significant absorption feature near 1400 nm.

4.10 Simulated Instrument sensitivity to CO₂

Our full forward model allows us to predict instrumentation sensitivity to variation in atmospheric composition. The upper panel of Fig. 35 shows a typical expected upwelling radiance field computed for the Argus spectral range under US standard atmospheric conditions and fitted for Argus observations recorded on February 24, 2009 at 45 °25'18" N, 75 °44'24" W latitude, longitude respectively. The lower panel of Fig. 35 shows the difference between this atmosphere and an atmosphere that has a 1% elevated CO₂ amount but is in other ways identical. From this analysis we estimate that the approximate sensitivity of radiance to a 1% change in CO₂ column is 0.12 %. For the same model, we can now generate a synthetic Argus spectrum in order to compute the CO₂ enhancement effect on our measurements. Fig. 36 shows the difference that would be recorded in counts between the two atmospheres according to our synthetic model. Using this analysis we also estimate that the 1% CO₂ enhancement causes an equivalent change of 0.41 detector counts. These Figures 35 and 36 clearly indicate that 1%

enhancement of CO₂ shows maximum sensitivity near 1580-1600 nm which is the target spectral window for our instrument in space.

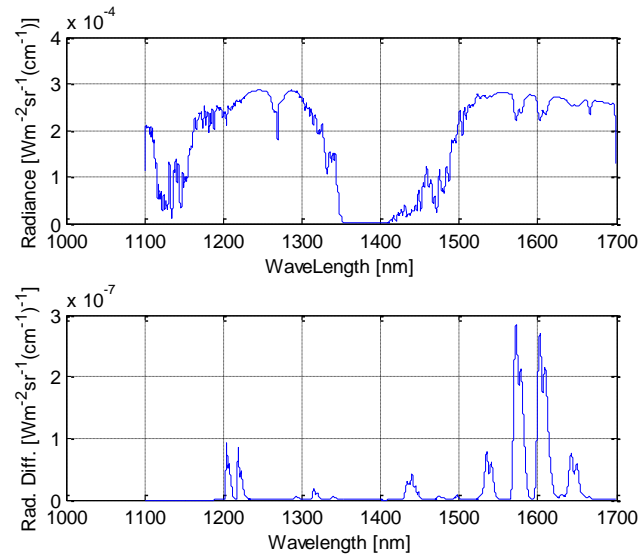


Fig. 35: Expected Radiance (Synthetic Model Prediction using GENSPECT) (upper panel) and difference in radiance at +1% change of CO₂ (lower panel).

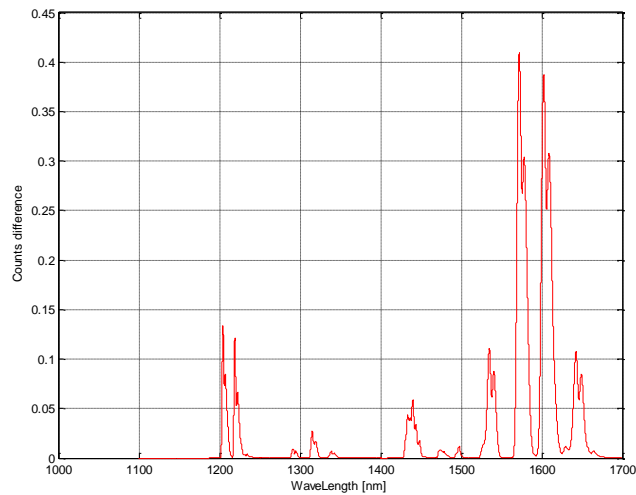


Fig. 36: Difference in Spectrometer Counts as simulated for a 1% CO₂ enhancement.

5.0 RESULTS AND DISCUSSION

The following sections present the results obtained for the calibration processes and space flight using the methodologies identified in Chapter 4.

5.1 Wavelength Calibration Results

Fig. 37a illustrates the spectral response of Argus under illumination by collimated monochromatic laser sources at the five wavelengths, when aligned with the spectrometer bore-sight. The linear variation of laser wavelength with respect to pixel number is shown in Fig. 37b. The indication of the accuracy is given in legends of Figs 37a and 37b. The non-linearity factor, obtained with second order polynomial fit, is less than 1%.

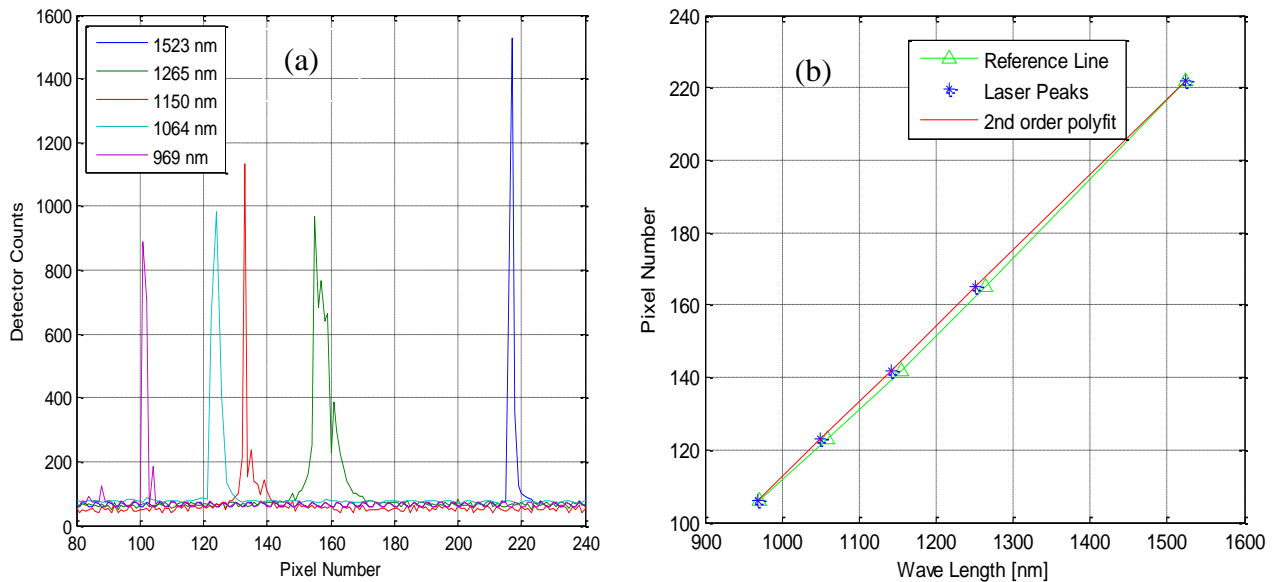


Fig. 37: (a) Argus 1000 spectrometer laser calibration, (b) Argus 1000 spectrometer laser calibration with five Lasers.

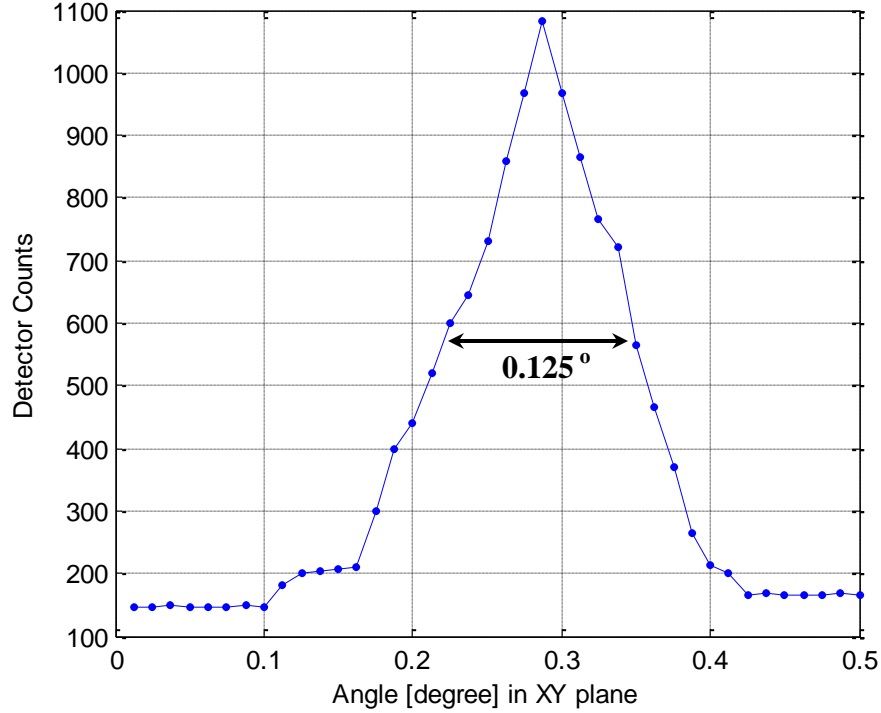


Fig. 38: The Argus 1000 angular sensitivity obtained by using milli-Watt collimated laser source at 1064 nm.

Fig. 38 shows the sensitivity of the laser peak response as a function of angle for the 1064 nm in x - y plane. We estimate the peak response at full width half maximum (FWHM) to be approximately 0.125° giving a spatial tile of 1.4 km on the ground at a 640 km mean orbital altitude. Fig. 39 shows the sensitivity to angle in the y - z plane. It is clear from both Fig. 38 and Fig. 39 that the FWHM is similar for both x - y and y - z plane.

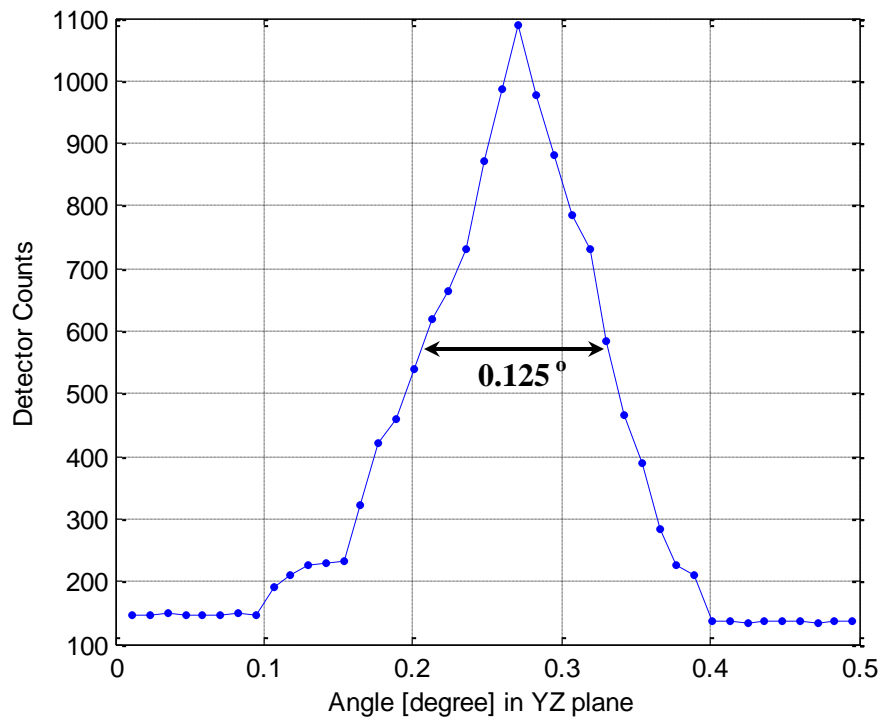


Fig. 39: The Argus 1000 vertical sensitivity obtained by using milli-watt collimated laser source at 1064 nm.

Fig. 40 shows the lasers bandwidths for these laser sources. The normalized area plots at scaled FWHM for different lasers 1064, 1150, 1265 and 1523 nm are respectively shown in Fig. 41. The Y-axis shows detector counts scaled such that the area under the curve is 1. These figures indicate that the gas lasers provide the best calibration sources, whereas 1265 nm diode laser has side bands (known from experience with other spectrometers) and has the largest bandwidth.

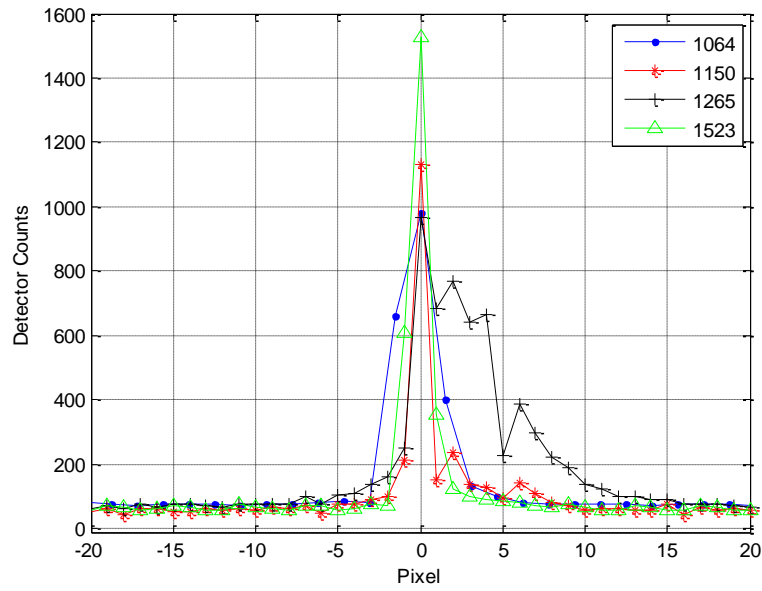


Fig. 40: Four lasers bandwidths for the Argus 1000.

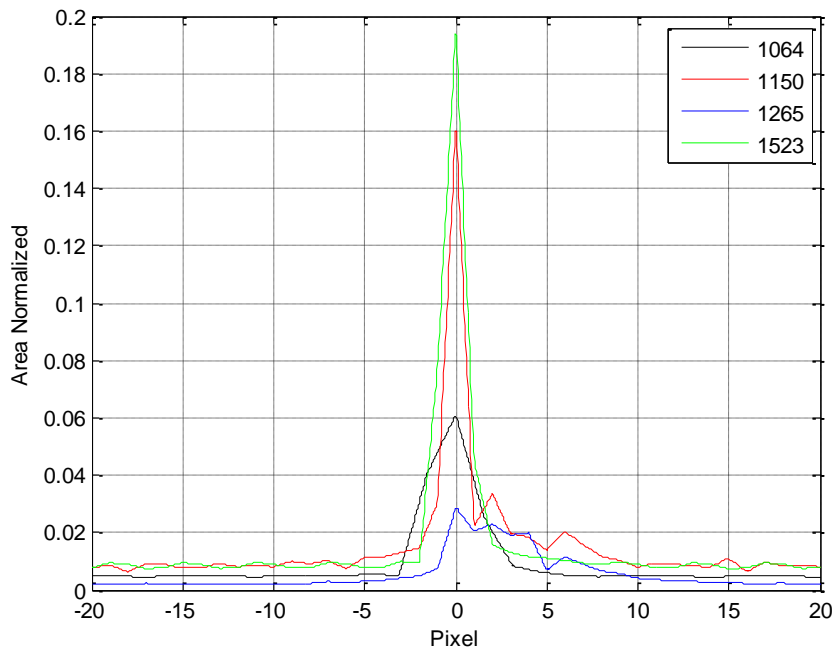


Fig. 41: Normalized area plots at scaled FWHM using four lasers of four different wavelengths.

5.2 Radiance Calibration Results

The variation of photons per count and joules per count as a function of wavelength for the calibrated lamp is shown in Fig. 42. The photons per count of the instrument are highest in the range between 900 to 1000 nm where its value reaches a maximum because of order filter cut-off. Above 1000 nm the photons per count gradually decreases with minimum at 1280 nm. The variation in joules per count arises because Argus has constant quantum efficiency over this wavelength range as shown in Fig. 15.

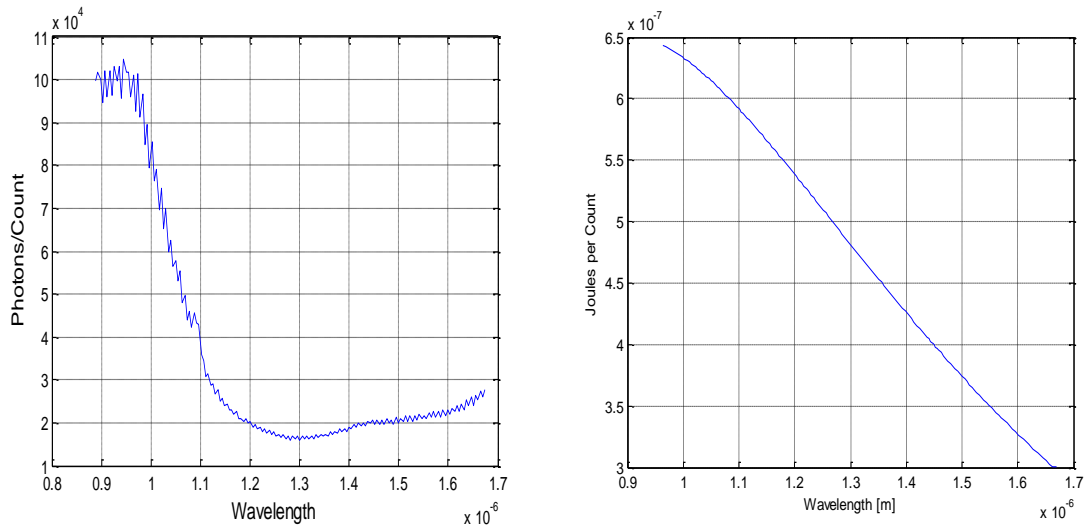


Fig. 42: The variation of (a) the photons count (b) joules count with respect to the wavelength for 1000 W calibrated lamp.

5.3 Gas Cell Calibration

Fig. 43 shows a comparison of results for radiation passed for the 1-m test cell containing 100% CO_2 compared with results for a cell filled with air at STP. This graph indicates about 10 absorption of CO_2 around $1.42 \mu\text{m}$ (7000 cm^{-1}).

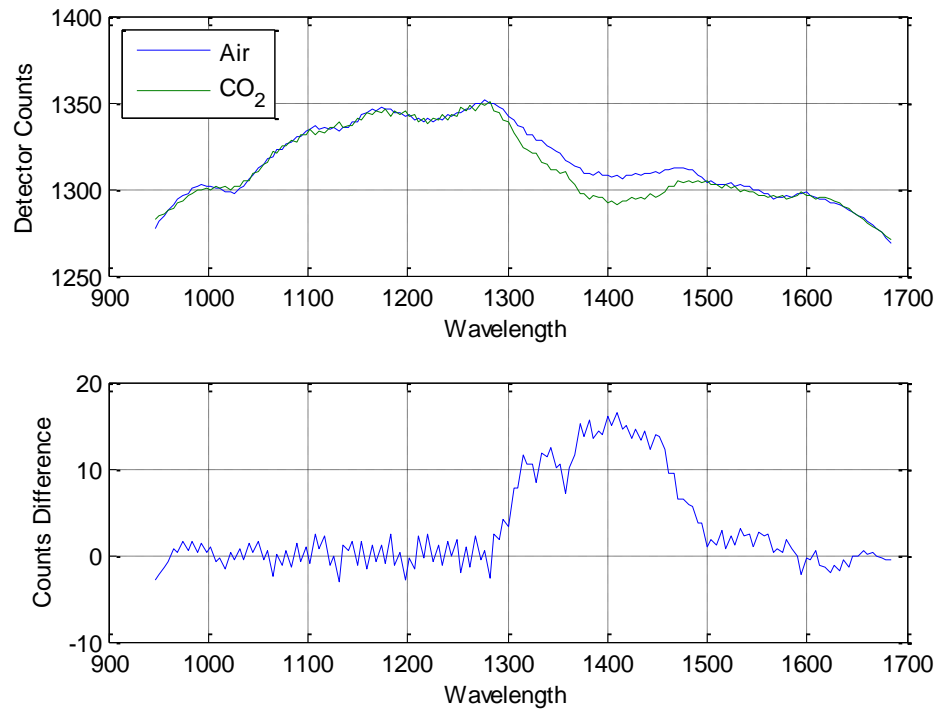


Fig. 43: (a) Comparison of spectra acquired when source illumination is transmitted through a 1-m CO₂ path compared with a 1-m air path (b) Counts difference of CO₂ compared to air.

Fig. 44 shows the comparison of experimental and modeled (using GENSPECT) detector counts as well as their absolute difference between these two detector counts for Argus using this procedure. It can be seen that the two curves are in good agreement throughout the entire range of the wave number spectrum. In particular, the discrepancy appears less than $\pm 2\%$. In the modeling of synthetic absorption, significant fitting parameters [Benner *et al.*, 1995] are cell pressure, cell temperature and blackbody radiation temperature, which were set as 101.3 kPa, 298 K and 2940 K, respectively. The

blackbody radiation temperature of the test lamp was calculated according to Wien's displacement law.

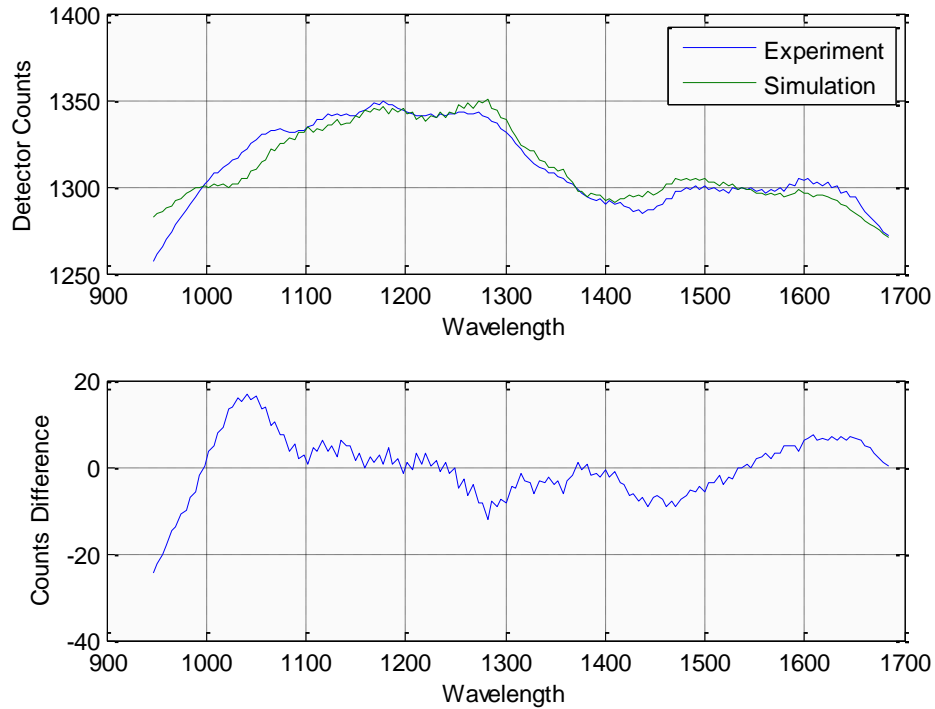


Fig. 44: (a) Comparison laboratory observed (gas cell flushed with CO₂ for 20 minutes and forward model (GENSPECT) equivalent detector counts and (b) the difference between these two Detector counts. The forward model assumes pure CO₂ in a 1 m long glass cell at STP.

Fig. 45 shows the variation of transmitted intensity of incident radiation through the gas cell as a function of time. Detector counts are shown to decrease until the gas cell becomes fully saturated with CO₂.

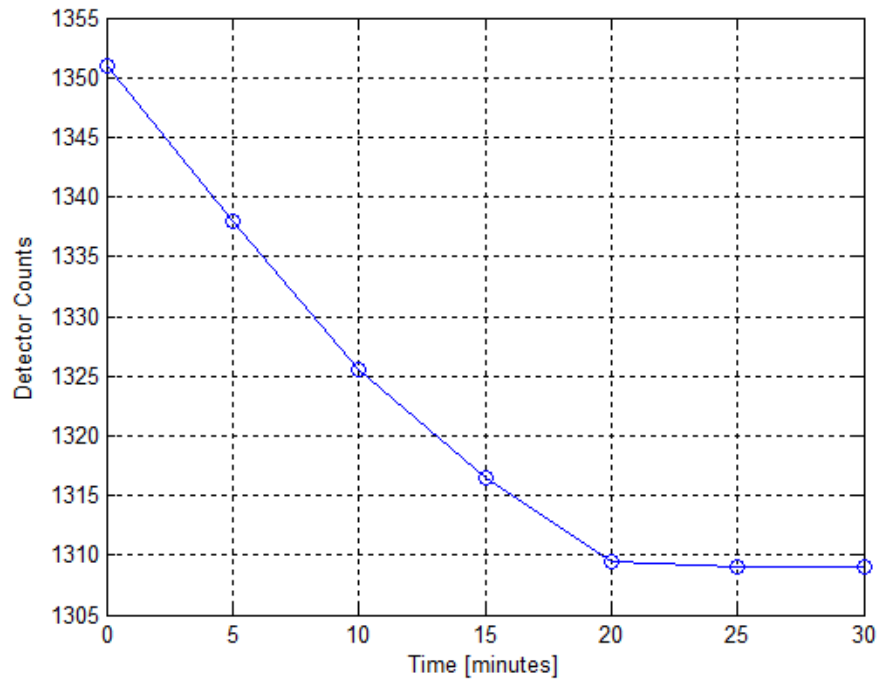


Fig. 45: Variation of detector counts showing decrease in transmittance of incident radiation as the concentration of CO_2 in the gas cell increases with time as CO_2 replaces the laboratory air.

Figures 46 through 48 show varying absorption as a function of wavelength when the glass cell filled with CO_2 , compared with an instance of detector response when the Argus is pointed towards the Sun (Fig. 46). We can clearly see that as expected, CO_2 (and H_2O) absorption features are prominent around 1420 nm, as well as near 1600 nm (where absorption due to CO_2 dominates). Fig. 48 indicates that a 1m STP path is equivalent to 40 detector counts in this region. Since this path is nearly 15% of an atmospheric path a CO_2 noise resolution of approximately 270:1 may be expected in the atmosphere.

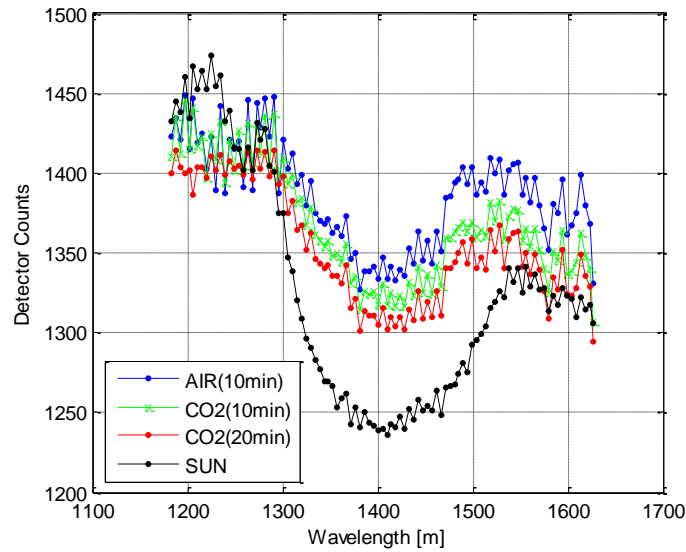


Fig. 46: Variation of Detector counts for Sun, glass cell filled with CO₂ after 20 min., glass cell filled with CO₂ after 10 minute, glass cell filled with air after 10 min.

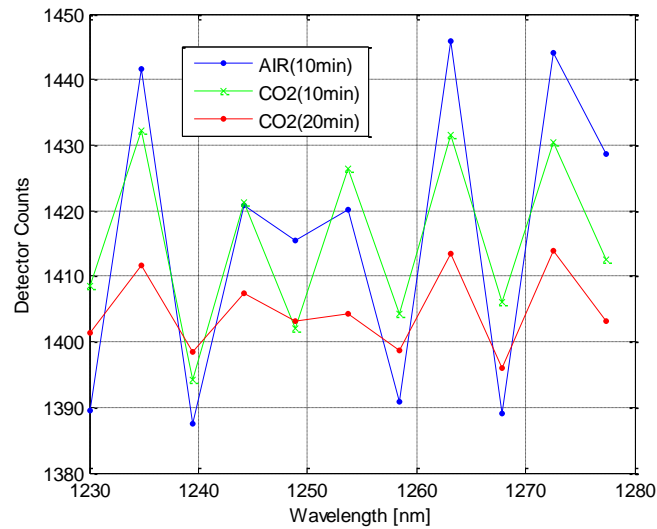


Fig. 47: Variation of Detector counts for glass cell filled with CO₂ after 20 min., glass cell filled with CO₂ after 10 min., glass cell filled with Air after 10 minute near O₂ window (CO₂ has limited absorption effect).

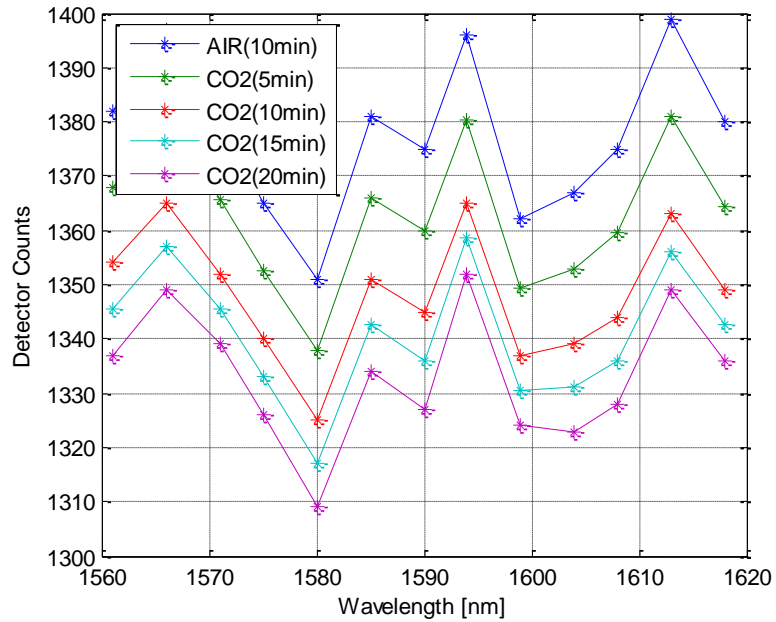


Fig. 48: Variation of Detector counts for glass cell filled with CO₂ after 20 min., glass cell filled with CO₂ after 10 min., glass cell filled with Air after 10 min. near CO₂ window (CO₂ has strong and well isolated effect).

5.4 Space Environmental Test Results

The resonance behavior of the spectrometer attached horizontally and vertically is shown in Figs. 49 a and b, respectively. The peak g forces experienced by the instrument during launch are estimated to be approximately 7-8 g lasting 135 seconds. The Q factor is calculated according to formula

$$Q = \frac{g_{peak\ load}}{g_{load}} \tag{10}$$

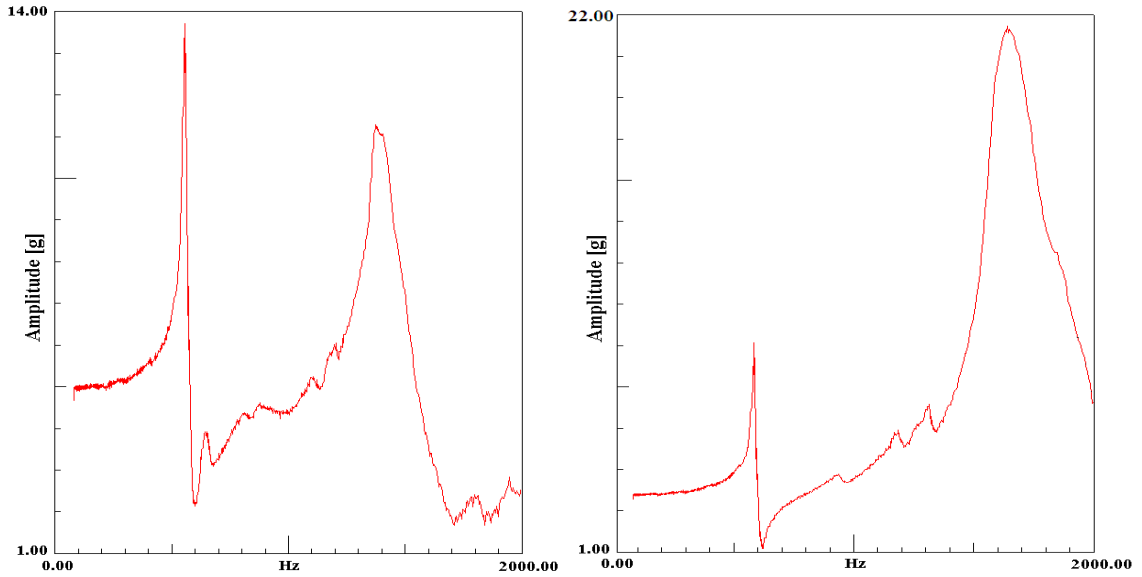


Fig. 49: Sinusoidal vibration test results with spectrometer attached (a) lengthwise horizontally and (b) vertically. The lens looks out of the longer side of the instrument.

where $g_{peakload}$ is the maximum acceleration experienced by accelerometer, g_{load} is the actual acceleration applied to the instrument. The g_{load} used in both the cases for this sinusoidal vibration test is $7.5g$. The $g_{peakload}$ values for horizontally and vertically attached position of the spectrometer to the vibration system are $14g$ and $22g$, respectively. The Q factors obtained in both cases are 1.87 and 2.93, respectively. Two main resonances are observed at 0.51 and 1.53 kHz. The magnitude of the first resonance is most significant in horizontal position while the magnitude of the second resonance is most significant in vertical position. In both cases the resonances are not regarded as a significant risk for space flight.

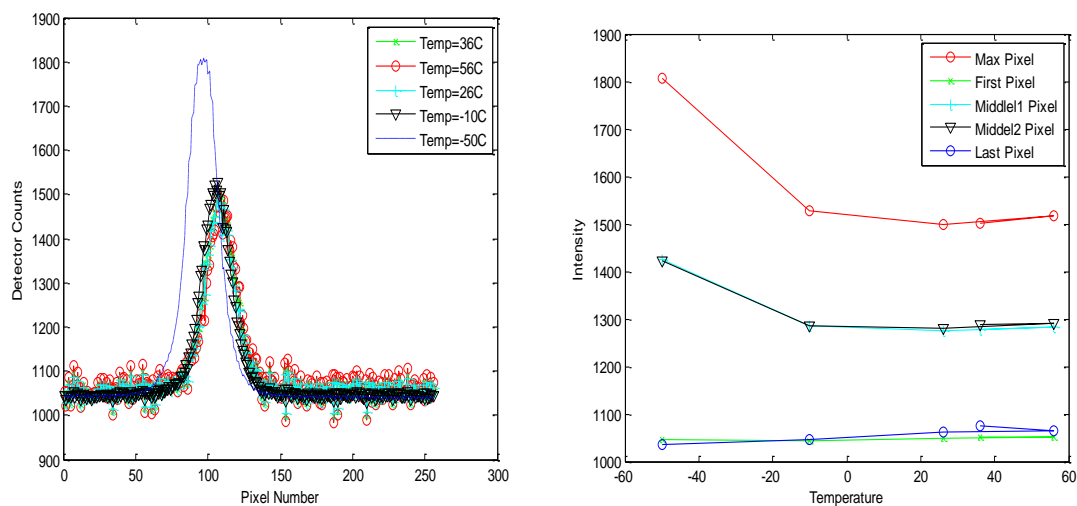


Fig. 50: (a) Detector counts of the Argus at different temperature, (b) Variation of the Intensity for different pixel positions at different temperature.

Fig. 50 (a) shows the variation in detector counts of Argus for five different temperatures during thermal vacuum test recorded at pressures of less than 10^{-6} Torr (1.3158×10^{-9} atm). A small increase in the detector counts is observed with decreasing temperature. The response is most non-linear at the lowest soak temperature of -50°C where a blue-shift of 12 nm is observed. However, the observed shift may not be related to the spectrometer characteristics for two reasons. First, the intensity of IR LED, used in test, exhibits an abrupt blue-shift at this temperature. Second, the thermal contraction of the base plate may also contribute an alignment error to this shift. Nevertheless, it is not desirable to operate the spectrometer at such low temperatures and the minimum operating temperature is recommended to be -15°C . This value is derived from Fig. 50b.

Fig. 50b shows the intensity for different pixels as a function of temperature. The variation of intensity was maximal at pixel 103, which has maximum detector counts

while variation was minimal at the first and last pixel. The intensity variation of two middle pixels exhibits an average of that for the maximum and minimum pixel variations. We can also observe that the variation in the intensity increases below 0°C temperature while it is almost unchanged at temperatures above 0°C.

Fig. 51 shows the variation of temperature for different thermocouples attached to the Argus and the plate over which instrument is placed during the thermal vacuum test. This figure indicates that up to 800 minutes, the temperature, except Eurotherm control temperature, at various points on the spectrometer and chamber are relatively close to each other. However, after 800 minutes the temperature of the chamber is controlled so as to decrease whereas the temperature of the thermocouples attached to the Argus 1000 spectrometer are almost unchanged. This signifies that there is no substantial temperature gradient on body of the spectrometer. This can be explained by the fact that the body of the spectrometer is made of aluminum alloy with high thermal conductivity. Such a design is necessary to prevent a temperature gradient for durable and reliable operation of the instrument working in the extreme space conditions.

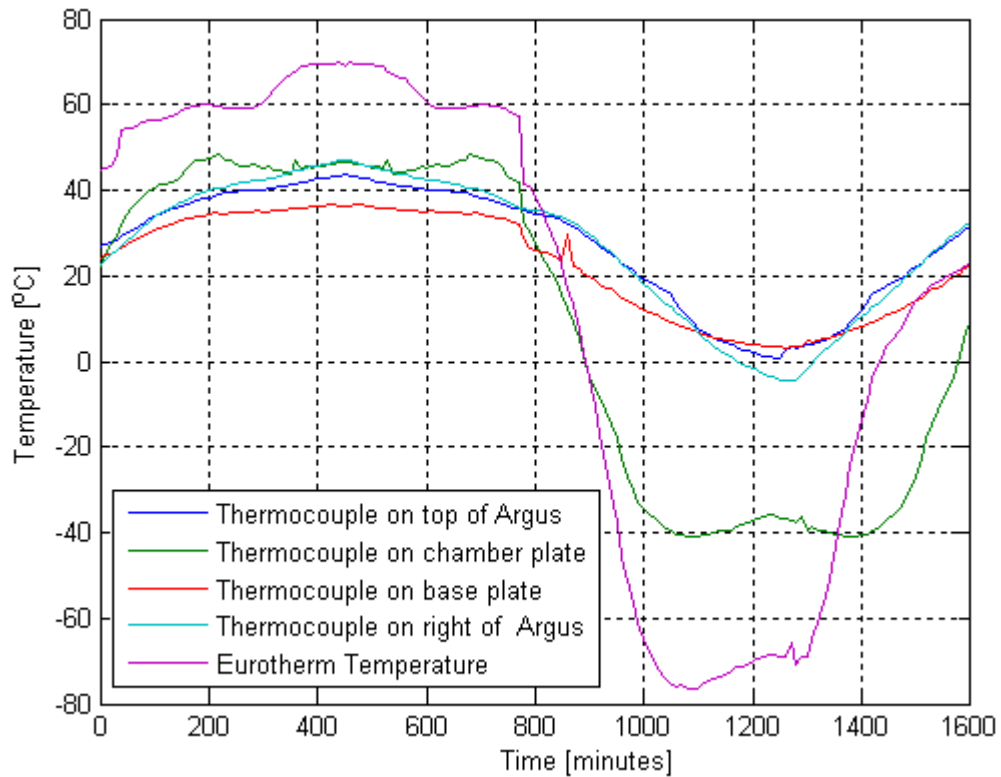


Fig. 51: Temperature variation with respect to time of thermocouples attached at different locations inside the chamber during the vacuum test of Argus.

5.5 Geolocation Results

Spacecraft position is determined using SGP4 propagation of two line elements, supplied by NORAD [Sarda *et al.*, 2006]. Fig. 52 shows the Argus 1000 footprint overlaid on two geographical data sets provided by Google Earth tools and accounting both the position and attitude estimates. The points on the ground during the observations of Fig. 52 are shown along with basic geography as well as cloud information that were also required for proper data interpretation [Jagpal *et al.*, 2010]. A significant issue for Argus was the availability of local cloud data for each measurement. Pseudo-true color

AVHRR cloud imagery was applied to assess the quality of the instrument data. In Fig. 52 an ellipse has been placed around the geolocated measurements of interest to indicate the uncertainty region.

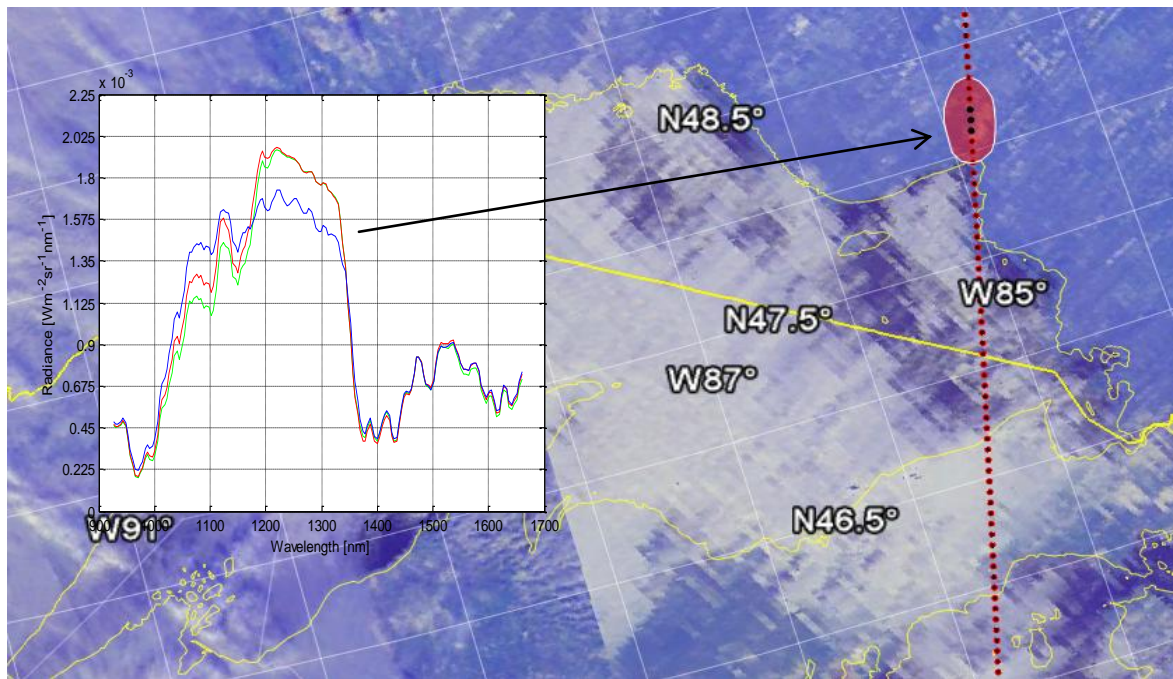


Fig. 52: Geolocated Argus observations using Google Earth with geography and cloud data overlaid. Inset illustrates three consecutive radiance spectra for these locations. Red ellipse shows the corresponding location as dots with an uncertainty zone.

Fig. 53 shows the nadir angle before and during the 4 minute spectrometer observation period of December 12, 2008 data. The nadir angle is approximately $7.7^{\circ} \pm 0.5^{\circ}$ for the duration of the observation.

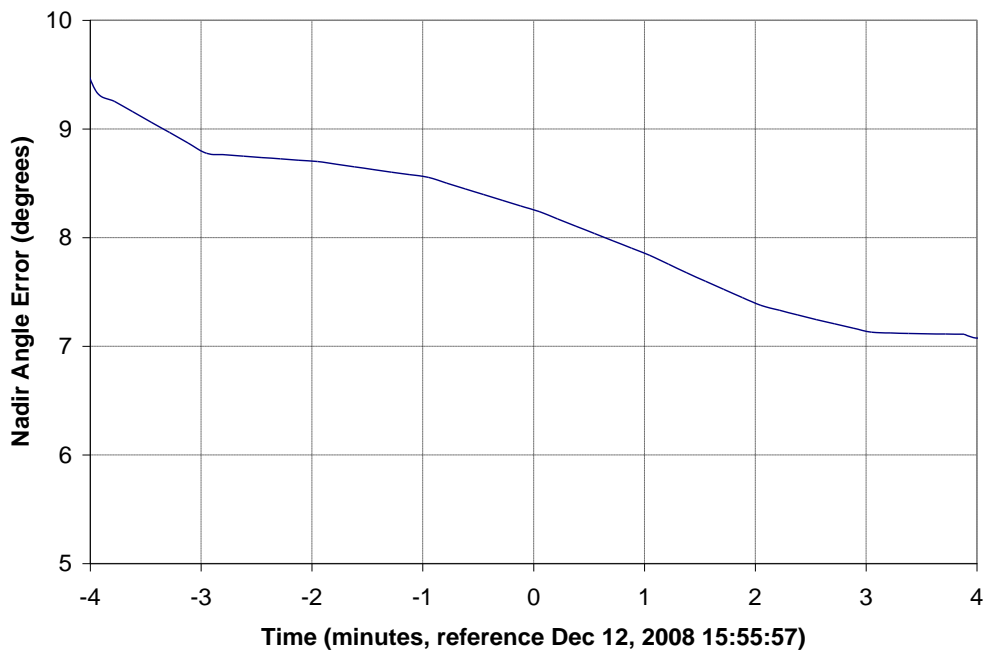


Fig. 53: Deviation from nadir view of Argus obtained using spacecraft telemetry.

Fig. 54 shows a KML (Keyhole Markup Language, used in Google Earth applications) file loaded in Google Earth containing part of Argus target point trajectory in blue, with yellow tack as a marker containing their latitude and longitude values. The red line shows the CanX-2 Sub satellite point path. This plot represents the geolocation of the 5 profiles shown in Fig. 64. The KML file writes the latitude, longitude, and height at each time step in which they are computed as a single coordinate triple in a line structure. The trajectories are created because this mapping software connects each subsequent latitude and longitude coordinate to the previous coordinate with a straight line along Earth's surface. The advantage of using KML is the ability to use mapping software to add layers of additional important information to the computed geolocation trajectories. For example, the date and time of the Google Earth satellite imagery can be manually set

in order to see the location of clouds at the date and time of acquisition [Chesser *et al.*, 2009].

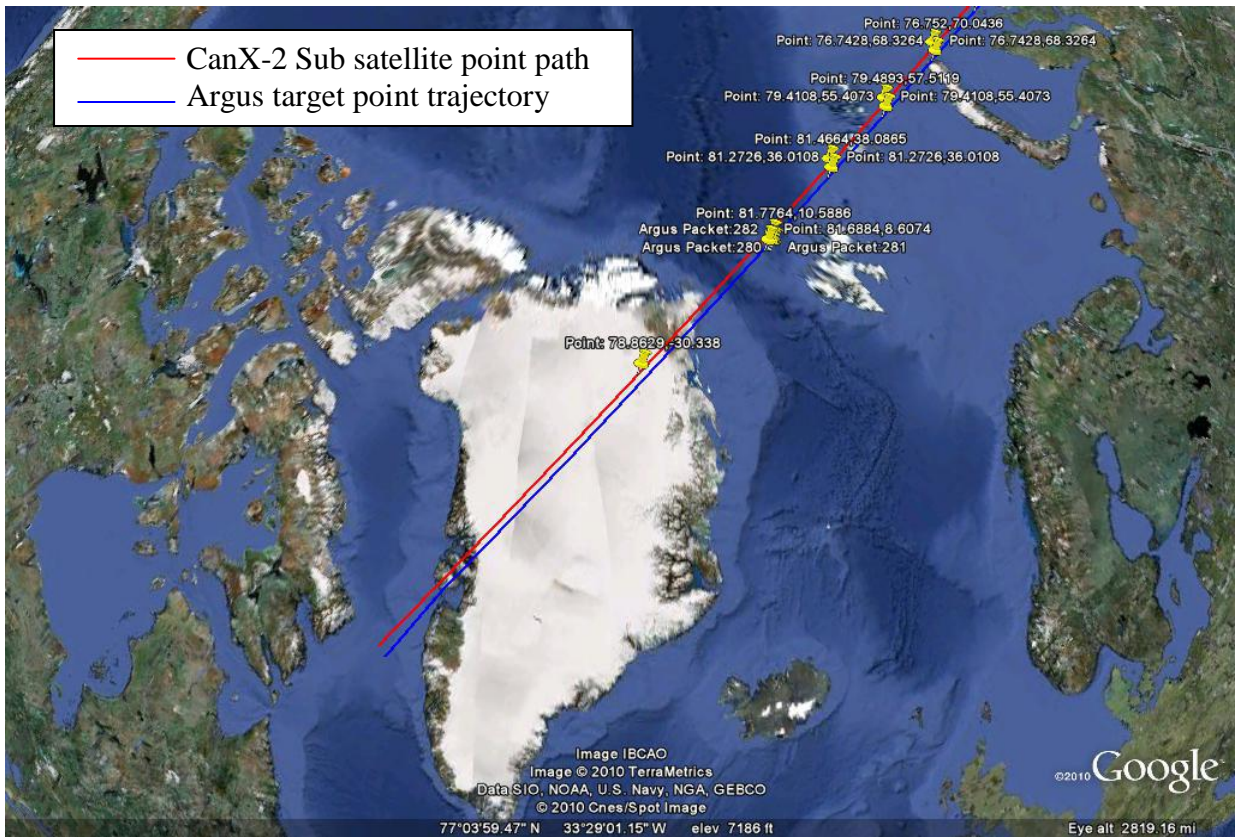


Fig. 54: KML Output in Google Earth of Argus Observations acquired over Arctic Ocean, on September 15, 2010.

A data set of observations over ocean and land has been recorded by Argus. Fig. 55 shows the frequency of nadir angle during that period for 90 profiles. This plot shows that the nadir angle deviation is between 2° to 4.5° which can be accounted for in geolocation analysis.

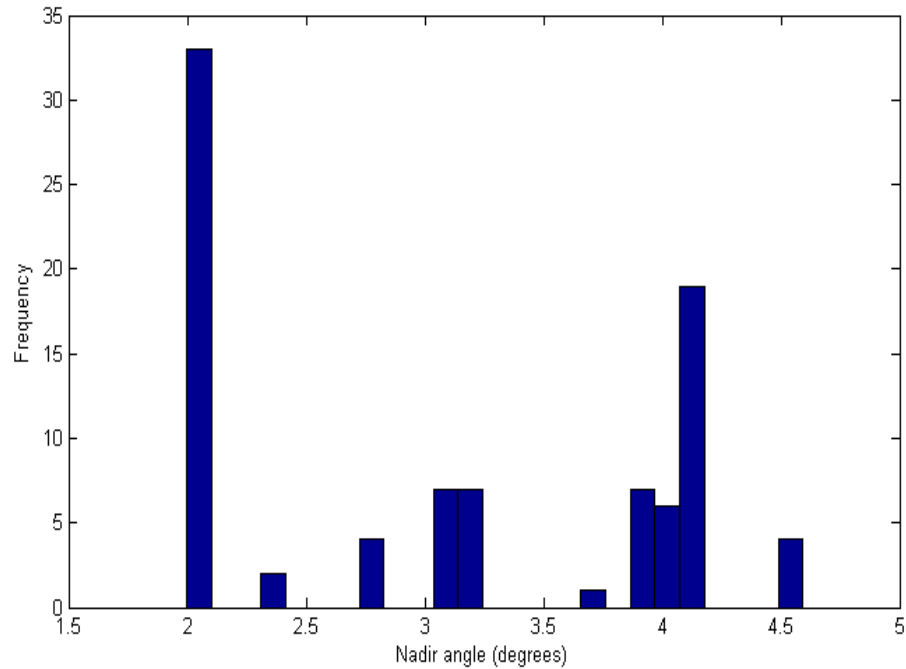


Fig. 55: Distribution of nadir angles (deviation from true nadir) for Argus observations – for approximately 91 sample profiles.

5.6 Space Results

Space data results for the Argus instrument are presented and discussed in the following sections.

5.6.1 December 12, 2008 (First Data)

The spectrum shown in Fig. 56 was observed by Argus over Ontario, Canada on December 12, 2008 having latitude and longitude ($44^{\circ}21'18''$) N and ($78^{\circ}22'32''$) W respectively. We can observe water vapour absorption near 1400 nm. Whereas carbon dioxide absorption is found near 1600 nm, we can also observe the signature of oxygen around 1260 nm.

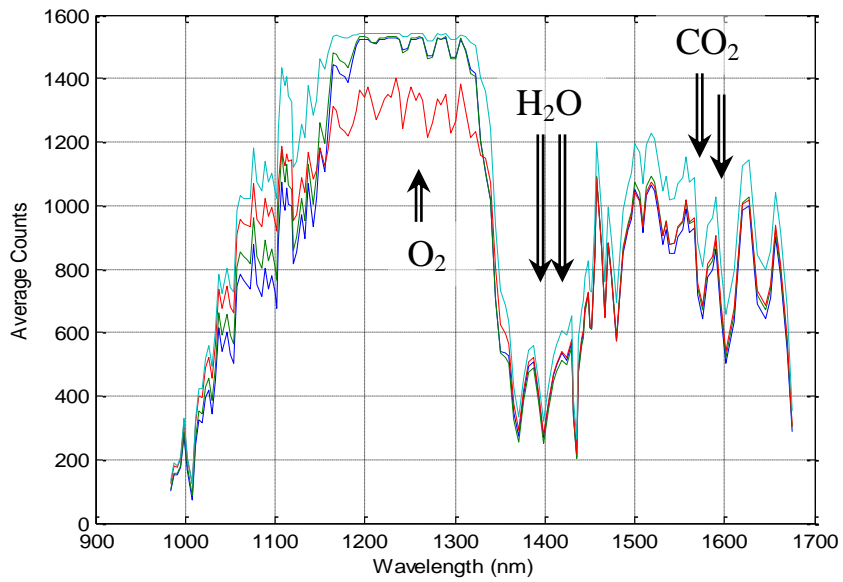


Fig. 56: Average detector counts of Argus on December 12, 2008. Different colors represent spectra numbers 160,161, 162.

Fig. 57 shows the temperature variation 289.5 K to 286.5 K within the detector with a Peltier cooler. We can see the variation from power up at 290 K to 287 K during Argus data observation.

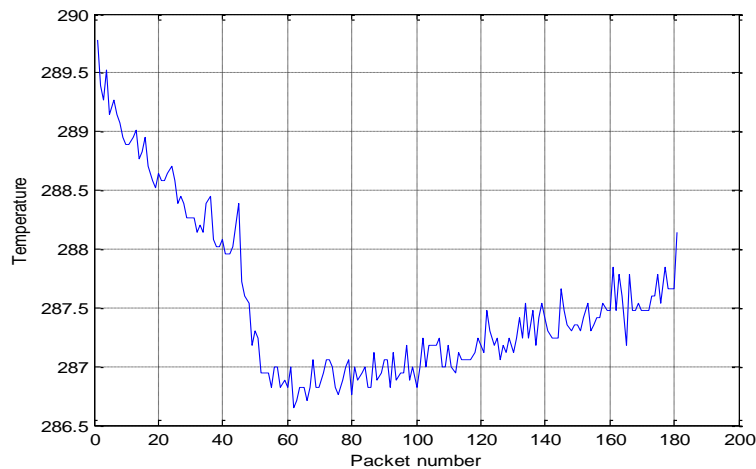


Fig. 57: Temperature variation of Argus 1000 for 3 minutes data taken on December 12, 2008.

Figures 58 and 59 show respectively raw and smoothed absolute radiance variation of Argus data taken on December 12, 2008. The CO₂ band near 1600 nm is clearly visible.

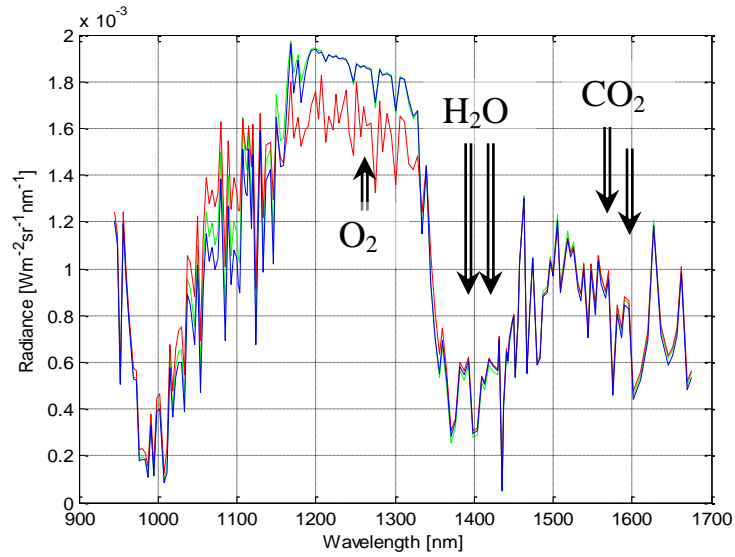


Fig. 58: Raw (unsmoothed) radiance spectra from Argus1000 observation on December 12, 2008. Different colors represent profile number 160, 161, 162.

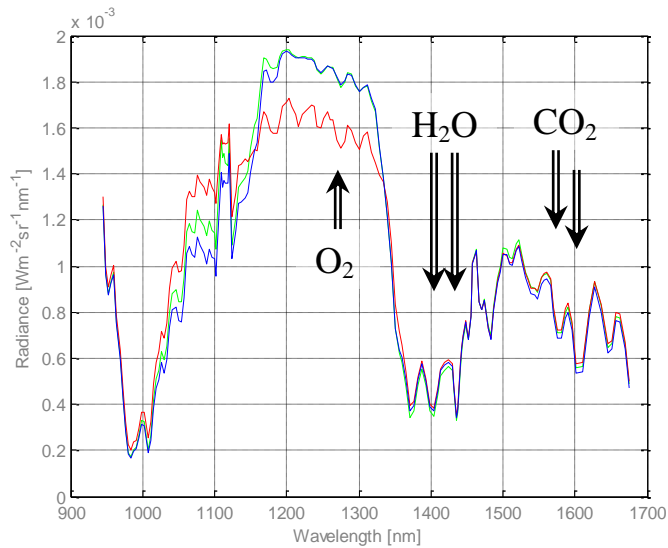


Fig. 59: Smoothed radiance spectra obtained from raw radiances in Figure 58.

5.6.2 June 11, 2010 (Vancouver, Canada)

Figures 60, 61, and 62 show the observed spectra (average counts) and corresponding radiance recorded near Vancouver, Canada having latitude and longitude (49°12'48") N and (122°57'54") W, respectively. We can clearly observe water vapour absorption, prominent near 1400 nm, CO₂ absorption 1600 nm and signature of O₂ at 1260 nm.

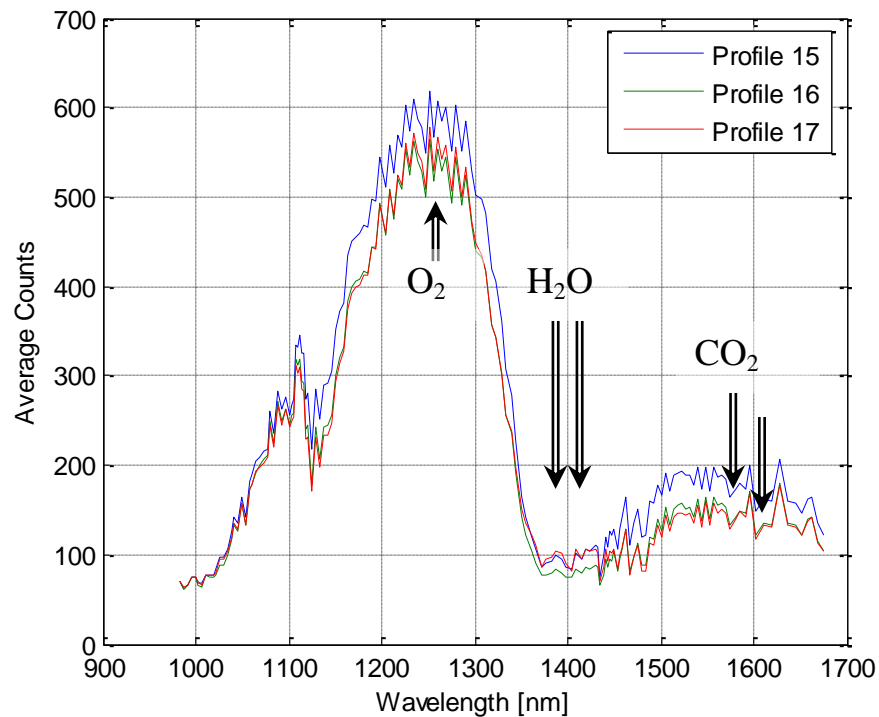


Fig. 60: Average Counts (Raw detector counts) recorded by Argus 1000 on June 11, 2010. Different colors represent profile numbers 15, 16, 17.

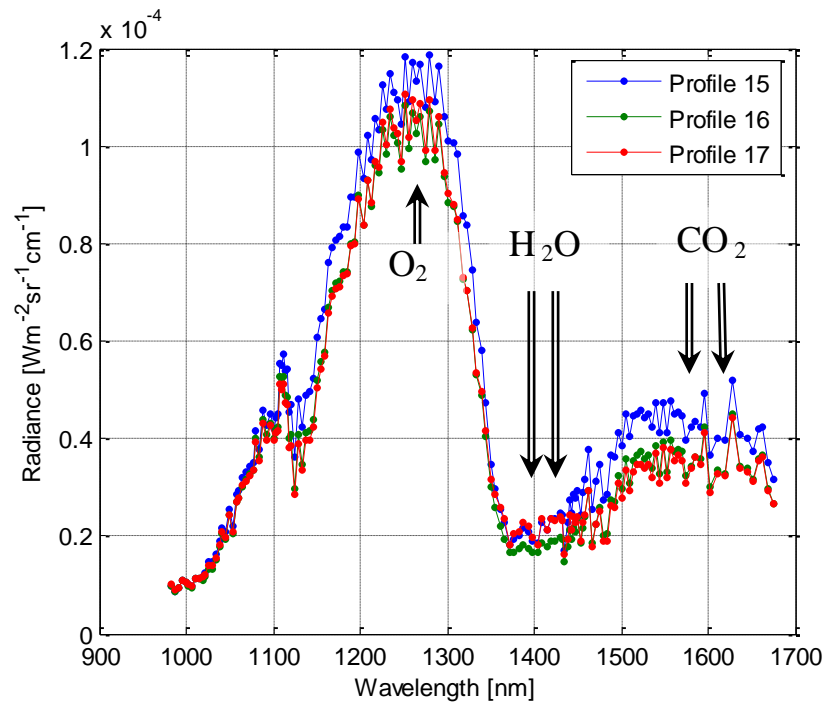


Fig. 61: Raw radiance spectra from Argus1000 on June 11, 2010.

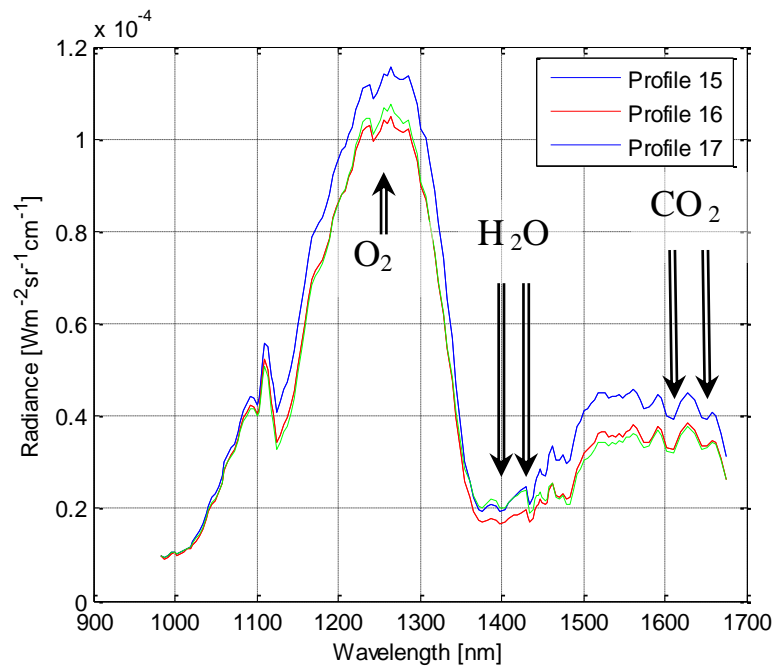


Fig. 62: Smoothed radiance spectra obtained from raw radiances in Fig. 61.

5.6.3 Space Observation Results over Ocean & Land

Fig. 63 shows the raw radiance plots taken on September 20, 2010 near Buenos Aires, Argentina at a latitude and longitude ($33^{\circ} 55' 49''$) S and ($58^{\circ} 42' 30''$) W, respectively. The profile numbers in this plot are 129, 130, 131 and 132 out of total profiles 284 for this data file.

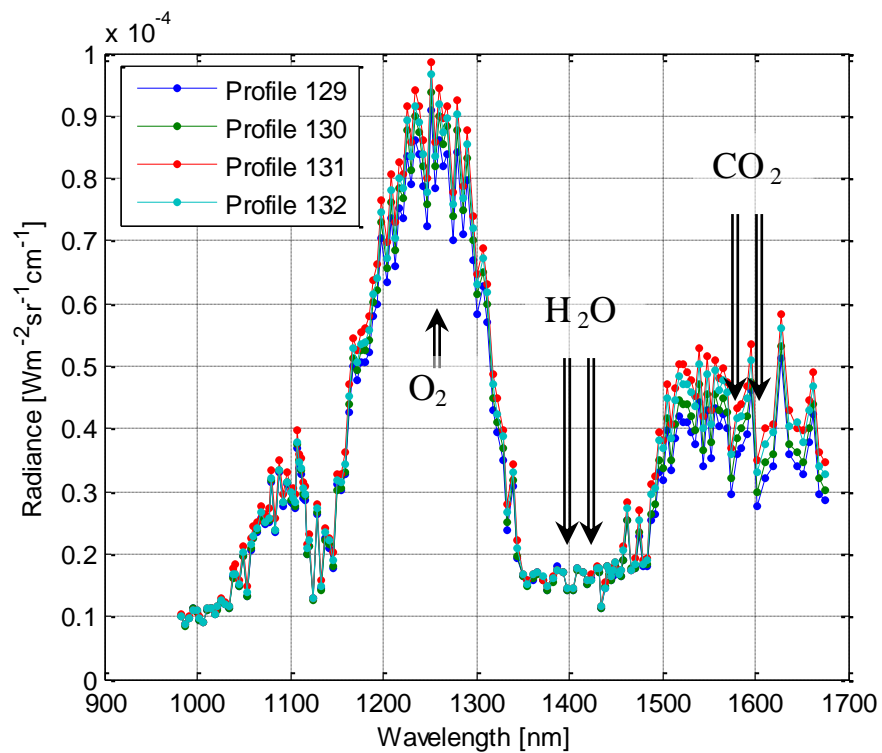


Fig. 63: Raw (unsmoothed) radiance spectra from Argus1000 on September 20, 2010. Different colors represent profile numbers 129, 130, 131, 132.

Fig. 64 shows the different observations taken on September 15, 2010 for five sets of data. There is about 1 hour between each data set which covered and latitudes from 58° to 81° . The absolute radiance varies by latitude because of solar geometry (two highest are at mid-latitudes in the Southern hemisphere) of the observations.

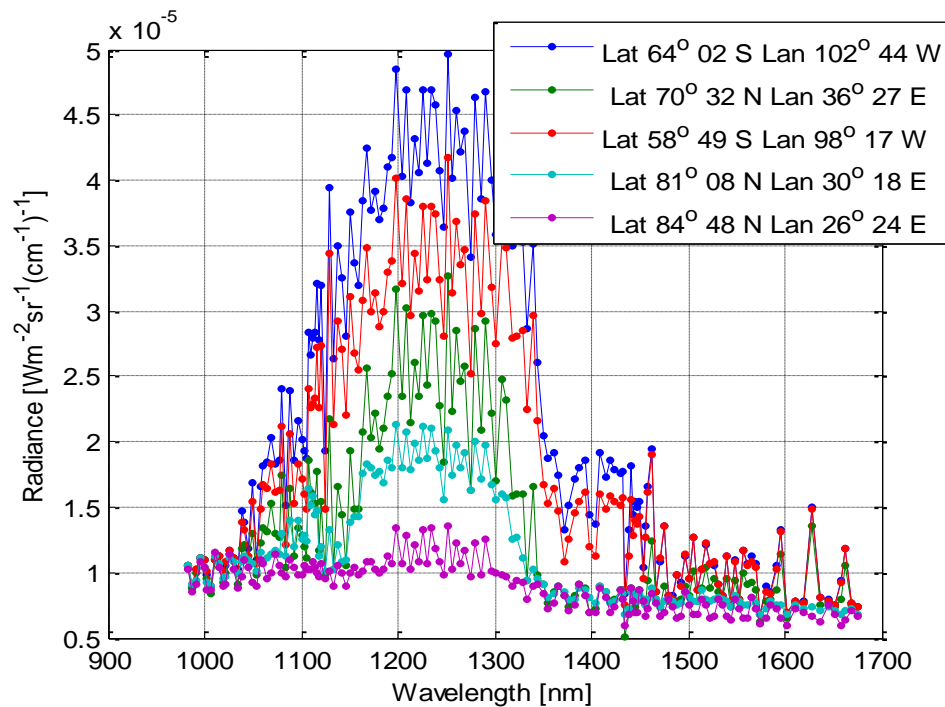


Fig. 64: Raw (unsmoothed) radiance spectra from Argus 1000 taken on September 15, 2010. Different colors represent profile with different latitude and longitude.

Following Fig. 65 shows a comparison of spectra collected over land and sea areas. The red line represents the data over Atlantic Ocean taken on September 06, 2010 having latitude and longitude $39^{\circ}47'30''$ S $129^{\circ}29'23''$ W. The blue line shows the data taken on same day over Alta Garcia, Argentina with latitude and longitude $31^{\circ}40' 28''$ S $64^{\circ}30' 32''$ W. We estimate the surface albedo to be 0.046 (over ocean) and 0.24 (over land) for these two cases, respectively.

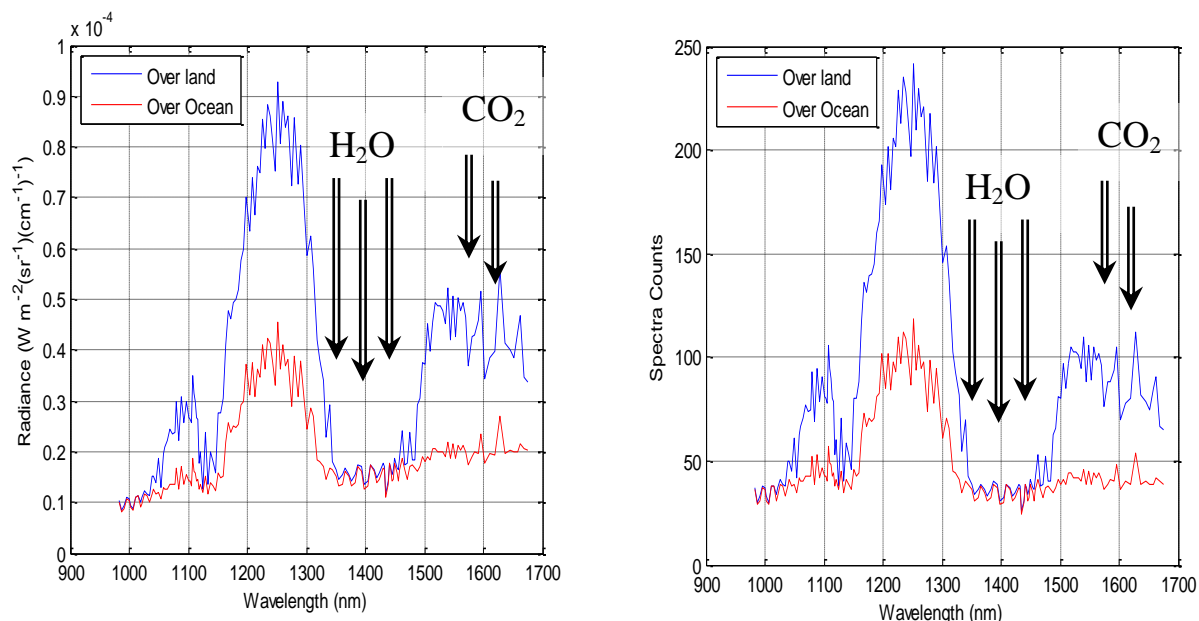


Fig. 65: Radiance spectra (left) and Spectra Counts (right) of Argus 1000 taken on September 6, 2010 data over land and ocean.

5.7 Retrieval Results

Any retrieval method is likely to be loaded with difficulty as no method can completely capture the complex behavior of the atmosphere. Even if the observational problems can be overcome the potential utility of such data may not be clear [Rayner *et al.*, 2009]. We used the method of optimal retrievals by means of a forward model to output simulated radiance observations. Unlike other techniques, a forward model provides an observation residual that reveals remaining uncertainties caused by unmodeled effects and observation and process noise. After launch, a flight calibration check is performed to verify wavelength calibration. Well known absorption features are utilized to determine a precise wavelength calibration. This flight calibration is utilized in the retrieval, to match the simulated spectra. In practice results are very similar to those obtained using laboratory calibration data.

Another instrument parameter is used in the construction of the instrument's slit function. The shape of the slit function, and the relationship between width and center wavelength is based upon laser calibration analysis and spectrometer measurements of the band pass of a sample Argus. A retrieved instrument parameter specifies the width of a two-sigma truncated Gaussian function convolved with this experimental slit function, accounting for the finite angular width of the focused light passing through the Argus.

Fig. 66 shows a comparison of GENSPECT simulated radiance and observations for a profile number 83 recorded by Argus on February 24, 2009 at latitude and longitude $45^{\circ} 25' N$, $75^{\circ} 44' W$, respectively. This spectrum for Argus 1000 spectrometer shows the absolute radiance value around 1.5×10^{-4} to $2 \times 10^{-4} \text{ Wm}^{-2} \text{sr}^{-1} (\text{cm}^{-1})^{-1}$. Model parameters are optimized to achieve best-fit retrieval results. The gases used in model are O_2 , CO_2 , CH_4 , and H_2O . Rayleigh single scattering is included in the model. The surface reflectivity is determined iteratively to be 3.9 % (assuming a Lambertian surface). This value matches reasonably well with the other space instruments as shown in literature for example the Chesapeake Lighthouse and Aircraft Measurements for Satellite (CLAMS) experiment and parameterization of spectral surface albedo [Jin *et al.*, 2004a 2005b]. The atmospheric composition model used is RefMod 2000 and atmospheric density model is from the US standard Atmosphere. The spacecraft nadir view angle is 5° , latitude is 50° and longitude is 92° , and Sun angle is 70° .

The presence of clouds imposes a major perturbation on our CO_2 retrieval. We have avoided retrievals for cloudy scenes. However, our results indicate that even the

presence of any cloud effects can significantly alter the measured spectra and, consequently, cloud contamination is likely responsible for some of the residual error.

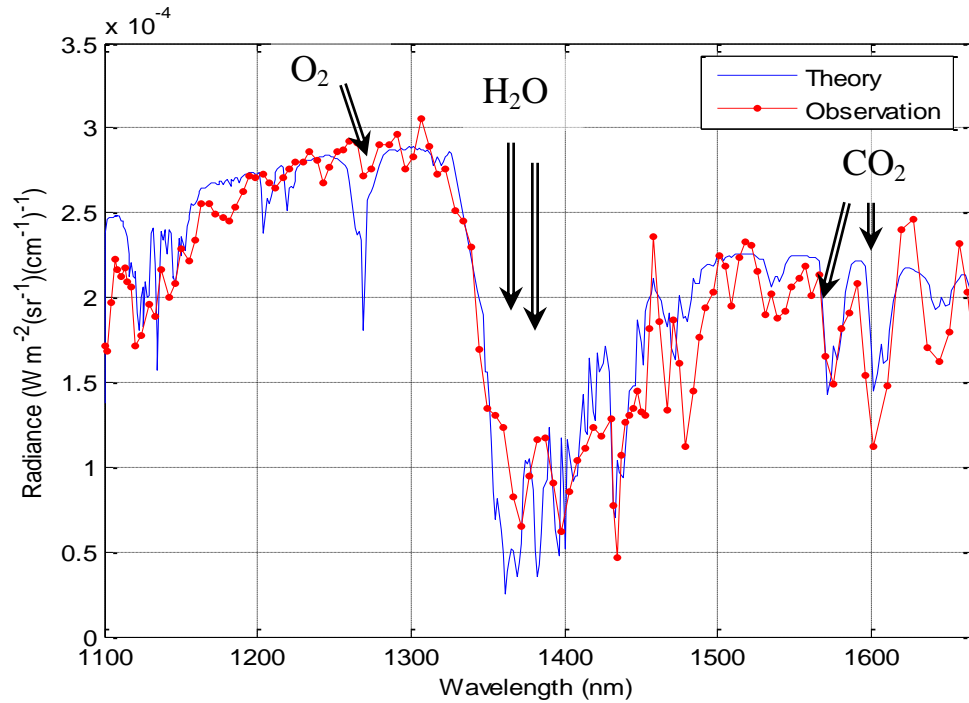


Fig. 66: Simulated (GENSPECT) and observed [actual orbital measurements recorded on February 24, 2009 at 45 degree 25 min N, 75 degree 44 min W near Hudson Bay, Canada].

As shown in Fig. 66, even for a fit encompassing the full Argus spectral window, there is a good match between model and observations near 1600 nm, an enlargement of which is shown in Fig. 67. For the O₂ feature near 1260 nm, we can see only an approximate match. This radiance field saturation of the spectrometer can be improved if integration times are reduced but at the expense of signal-to-noise performance at the CO₂ peak. Collision-induced absorption and line mixing in the dense line structure of the O₂ band may also contribute to this error. Similarly, for the water vapour feature near

1400 nm, it is difficult to match observations due to the large variability in the vertical and horizontal distribution of water vapour content. Our results from Argus report the first known match between experiment and simulation in this spectral band between 1000-1700 nm. Despite some discrepancies in our representation of the transfer of radiation through the atmosphere and the instrument measurements made by Argus, the GENSPECT model provides a reliable basis to evaluate retrieval methods for this important spectral window. Other sources of residual fit error include, spectroscopic modeling errors, anisotropy, multiple scattering, aerosols, polarization effects, difference in spectral resolution and uncertainty in other retrieval parameters such as albedo.

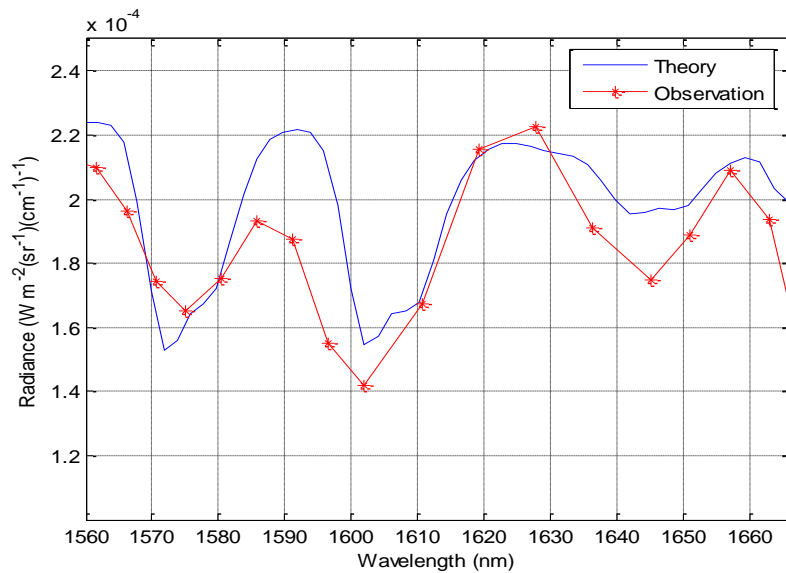


Fig. 67: Simulated and Experimental radiance for CO₂ absorption window around 1600 nm (120 % of standard atmospheric concentrations used).

To match the absolute radiance measurements with the simulated radiance, we used the following mixing ratio (gas concentrations) of the species. CO₂ concentration was increased by 20% of standard 384 ppm value of carbon dioxide and the concentration

of water vapour was reduced by 80% of its standard value in the model, (water vapour is one of the most variable constituents in the atmosphere).

The CO₂ enhancement required to fit our data is clearly non-physical as the standard CO₂ concentration is well established by ground-based instrumentation. Instead, our hypothesis is that the presence of even small cloud and aerosol amounts in the surrounding atmosphere causes path enhancements through multiple scattering. As noted earlier photons that undergo multiple scattering travel a longer path through the atmosphere and, consequently are more likely to be absorbed by CO₂ and other species. For example, if 20% of photons experience a double surface reflection (they reflect off the surface, off a cloud and then back off the surface again) before reaching the instrument then these photons will travel through the dense lower atmosphere approximately twice. Consequently, absorption features will be enhanced by approximately $0.8 + 0.2 * 2 = 1.2$ (20% absorption enhancement). A multiple scattering model may help to address this matter. However, it is very likely that the model will simply require inclusion of additional parameters that must be adjusted to match enhanced absorption. Such model parameters are unlikely to be independent of uncorrelated CO₂ concentration parameters making the multiple scattering effects indistinguishable from absorption enhancement.

As a result of multiple scattering in the aerosol layers the light path is enhanced compared to the situation where aerosol scattering is neglected. This scattering effect can cause very complex modifications of the satellite observed radiance spectra and there is nearly an infinite amount of micro and macro physical parameters that are needed to

expansively report for all scattering effects in the forward model [Reuter *et al.*, 2009]. Overestimation of the CO₂ column diverse aerosol types may be because of differences in single scattering albedo, scattering phase function, and spectral dependence of the aerosol optical thickness. Obviously, from the estimated errors for the diverse atmospheric scenarios and observation geometries a modification is needed to account for the effect on the light path caused by multiple scattering for more accurate CO₂ features. This issue has been recognized by the other teams of the CO₂ mission SCHIMACHY, OCO and GOSAT [Aben *et al.*, 2007].

The other major factors are considered are albedo, emissivity, nadir angle and Sun angle to obtain results of the best fit. We use an equivalent Sun and Earth temperature 5750 K and 288 K respectively in the retrieval code where we assumed different parameters to obtain the simulated radiance plot [Jagpal *et al.*, 2009]. Adjusting the blackbody temperature of the Sun in our retrieval provides a means to account for solar variability induced by Sun-spots, solar flares and other short-duration solar phenomena as we approach the next period of maximum solar activity. These effects act to increase (flares) or lower (spots) the Sun's effective temperature that may be accounted for by adjusting the idealized blackbody emission model utilized in our simulations.

5.7.1 Results of data from May 28 and Sept 20, 2010

Experimental results obtained on May 28, 2010 and September 20, 2010 data are shown in Fig. 68 and 69, respectively. These data were collected over New Delhi, India and Atlantic Ocean, respectively. The spectrum was obtained at exposure time 204.8 ms

and capacitance setting is 10 pF. For Fig. 68, the path is nadir solar-reflection for 1030 Orbit at 45N. The spacecraft nadir view angle is 4° , latitude is $28^\circ 37' 33''$ N and longitude is $77^\circ 13' 44''$ E and Sun angle is 65° . The mixing ratio of CO_2 in the model has been enhanced by a factor of 25% to obtain a good fit to the radiance profiles observed by Argus over New Delhi, India.

Fig. 69 is based on observation profile 91 taken on September 20, 2010 having latitude and longitude ($54^\circ 11' 18''$) S and ($71^\circ 22' 32''$) W respectively. The CO_2 concentration is retrieved at 384 ppm and temperature of Sun is 5780 K. The mixing ratio of CO_2 in the model uses the standard model amount of CO_2 to obtain a good fit to the radiance profiles observed by Argus. This observation is of a particularly cloud free scene as verified by Google Earth KML file analysis. Both Fig. 68 and Fig. 69 shows a comparison of the simulated radiance (using GENSPECT) with Argus measured radiance profiles in the spectral region where absorption due to CO_2 is almost exclusively dominant. It can be seen from Fig. 68 that while the general behavior of the recorded profiles are roughly similar to that expected from GENSPECT, the variation in absolute radiance is somewhat different from the one another. This might be due to variations in background albedo, and the presence of clouds.

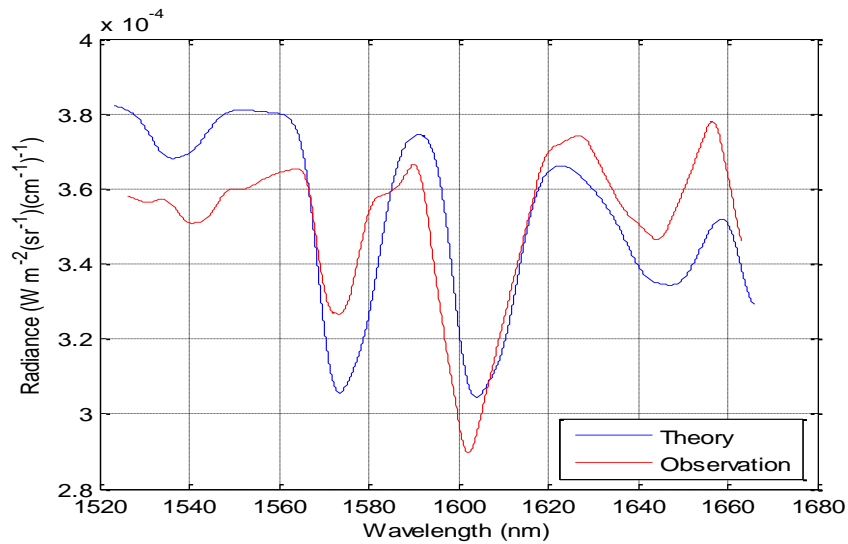


Fig. 68: Synthetic and Experimental radiance for CO₂ absorption window at 1600 nm (May 28, 2010 observation at 15:27 GMT) latitude is 28°37' 33" N, longitude is 77°13' 44" E and Sun angle is 65°.

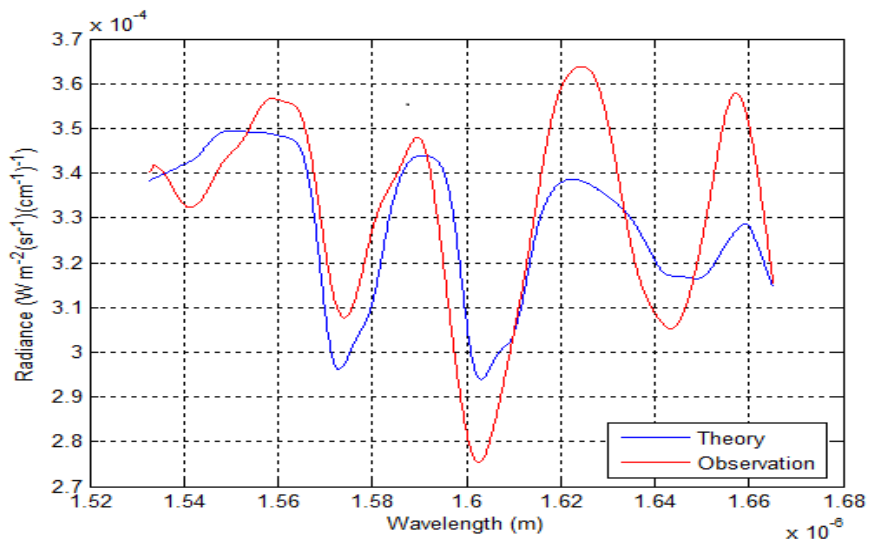


Fig. 69: Synthetic and Experimental radiance for CO₂ absorption window around 1600 nm (September 20, 2010 observation at 15:30 GMT) latitude (54°11'18") S and longitude (71°22'32") W respectively.

In most analysis cases it is necessary to enhance CO₂ amount in our model to match with absolute radiance amount obtained by Argus. The SCIAMACHY instrument also has some issues with their retrieval algorithm [Bösch *et al.*, 2006] which lead us to speculate that the majority of retrieval algorithms [Nassar *et al.*, 2003] applied to space-based CO₂ observation utilize hybrid retrieval approaches in order to match ground-based observation concentrations. [Buchwitz *et al.*, 2009].

The upper part of the Fig. 70 shows the radiance over 1520 to 1660 nm NIR spectral range between GENSPECT model radiance (blue) and Argus 1000 observation radiance (red). Their residue of the radiance data is shown in lower part in the Fig. 70. We can see the reasonable match between two curves of the radiance data in this spectral window.

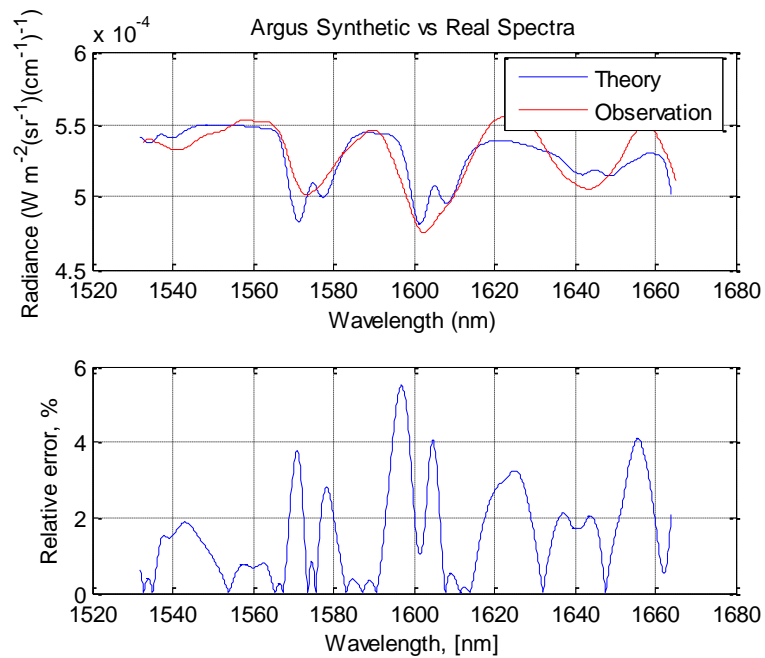


Fig. 70: Comparison of Synthetic and Argus radiance observations (upper panel) and residual (lower panel).

5.7.2 Presence of Clouds

In this section we present data collected with and without the presence of cloud. Fig. 71 represents the data obtained on December 12, 2008 having latitude and longitude (42°58'12") N and (80°03'22") W, respectively for cloud free observation. The measurement taken in the presence of cloud have latitude and longitude (43°37'42") N and (78°45'34") W, respectively. The spectra with cloud have more reflected radiance because in the presence of clouds a significant fraction of the sunlight is immediately reflected back to space by the cloud. In this case the spectra looks more like a solar extraterrestrial Black body contaminated with water vapour. We note that between 1050 nm and 1350 nm the spectrum becomes saturated at this integration setting because of the additional radiance.

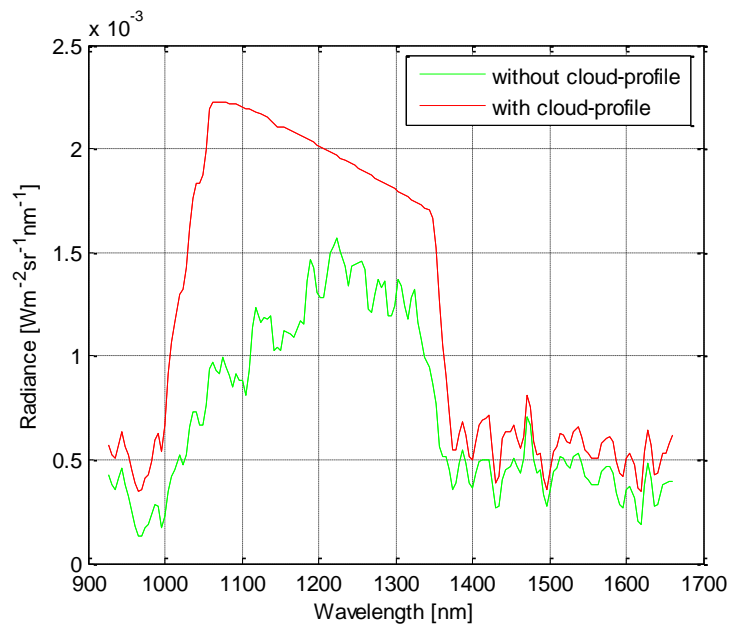


Fig. 71: Radiance plot for profile with cloud and without cloud of the data obtained on December 12, 2009.

5.7.3 Comparison of Rural vs. Industrial Zones (June 2, 2010 data over India)

Fig. 72 and 73 show the Google Earth map over South Asian region. The blue line represents the Argus 1000 target trajectory while the red line represents the CanX-2 path over the ground.

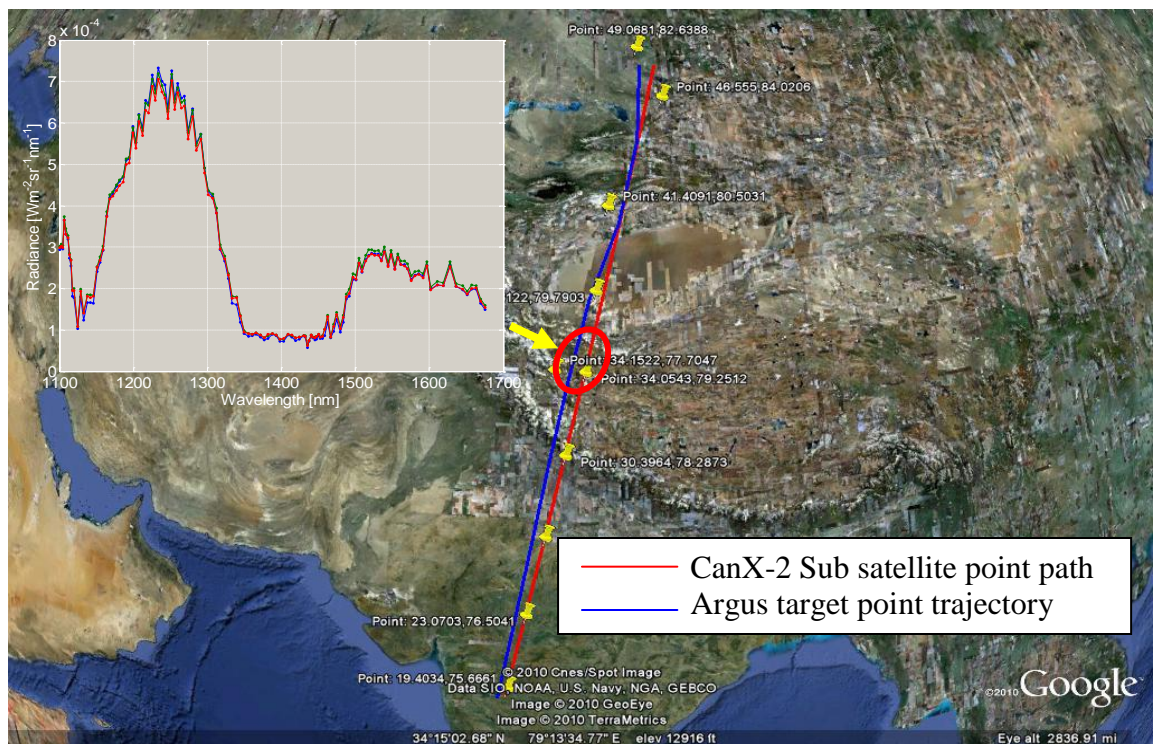


Fig. 72: Geolocated Argus observations using Google Earth with geography and cloud data overlaid. Inset illustrates three consecutive radiance spectra for these locations. Red ellipse shows the corresponding location as dots with an uncertainty zone.

The radiance spectra taken over the land of Northern India are indicated by red ellipses. The yellow tags depict the latitude and longitude coordinates along blue and red traces. The inset in Fig. 72 illustrates the radiance of the profile numbers 64, 65, and 66, which were recorded over $29^{\circ} 58' 15'' \text{ N}$, $78^{\circ} 10' 24'' \text{ E}$. This is a hilly area with no obvious sources of industrial pollution nearby. The inset in Fig. 73 shows the radiance profile numbers 88, 89 and 90, recorded over $34^{\circ} 35' 25'' \text{ N}$, $77^{\circ} 12' 32'' \text{ E}$. This is close to a major industrial area known as the Steel Hub— producing steel, cooper, aluminum and some other metals.

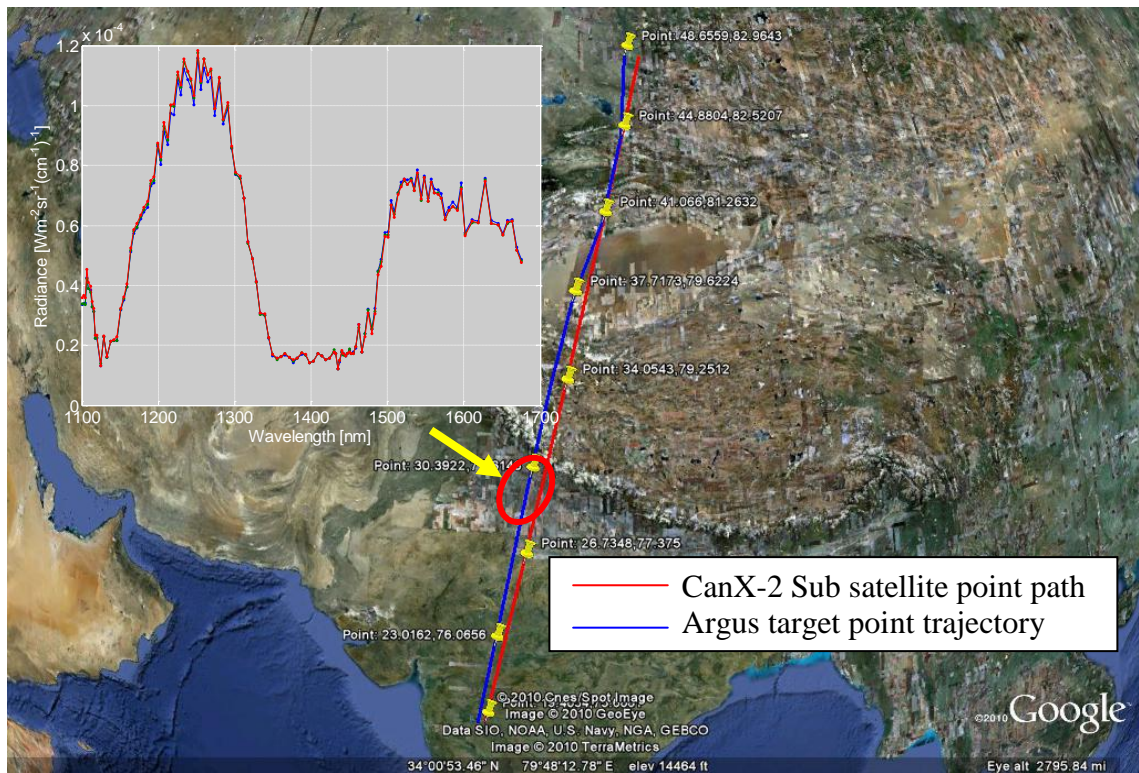


Fig. 73: Geolocated Argus observations using Google Earth with geography and cloud data overlaid. Inset illustrates three consecutive radiance spectra for these locations. Red ellipse shows the corresponding location as dots with an uncertainty zone.

Comparing two spectra from insets in Fig. 72 and 73, we can see the significant absorption of CO₂ in the IR region around 1580 nm to 1620 nm over the industrial area. Using GENSPECT radiative transfer model we determined 15% additional increase of CO₂ concentration is required to fit the spectra for the polluted location. This additional absorption may be inferred by the increase of CO₂ concentrations and by enhancement of CO₂ absorption by aerosol emission.

We note that our results of CO₂ enhancement observed over cities are in good agreement with those recently reported by ground-based instrumentation [Rigby *et al.*, 2008; Jacobson 2009].

5.8 Comparison of Argus 1000 and GOSAT

In this section we compare results from Argus, a grating spectrometer, with that of GOSAT-FTS, a Fourier transform spectrometer. GOSAT-FTS makes measurements in the same IR region as Argus but with a narrower spectral band but much higher spectral resolution.

The data rate of GOSAT-FTS is comparable with that of Argus; however the spacecraft and communications segments are capable of downloading significantly higher volumes of instrument data. Over a three-day period, GOSAT-FTS takes fifty-six thousand measurements. Since their analysis is limited to areas under clear sky conditions, only two to five percent of the data collected (approximately 300 to 900 spectra per day) are usable for calculating column abundances of CO₂ and CH₄. The column abundances of CO₂ and CH₄ are then averaged on a weekly or monthly basis and processed into global distribution maps.

A comparison of the radiance spectra observed by Argus 1000 and GOSAT instruments was undertaken. In order to perform the comparison, the difference in convolution slit function for the two instruments must be taken into account. The GOSAT data contains near IR radiance data in units of $(V\text{cm}^{-1})$. To convert the unit to $(W\text{m}^{-2}\text{sr}^{-1}(\text{cm}^{-1})^{-1})$, the TANSO-FTS radiometric conversion coefficient is used. For comparison purposes, Argus and GOSAT data are smoothed. Fig. 74 shows the GOSAT radiance (blue) and its smoothed variation (red) over the NIR region.

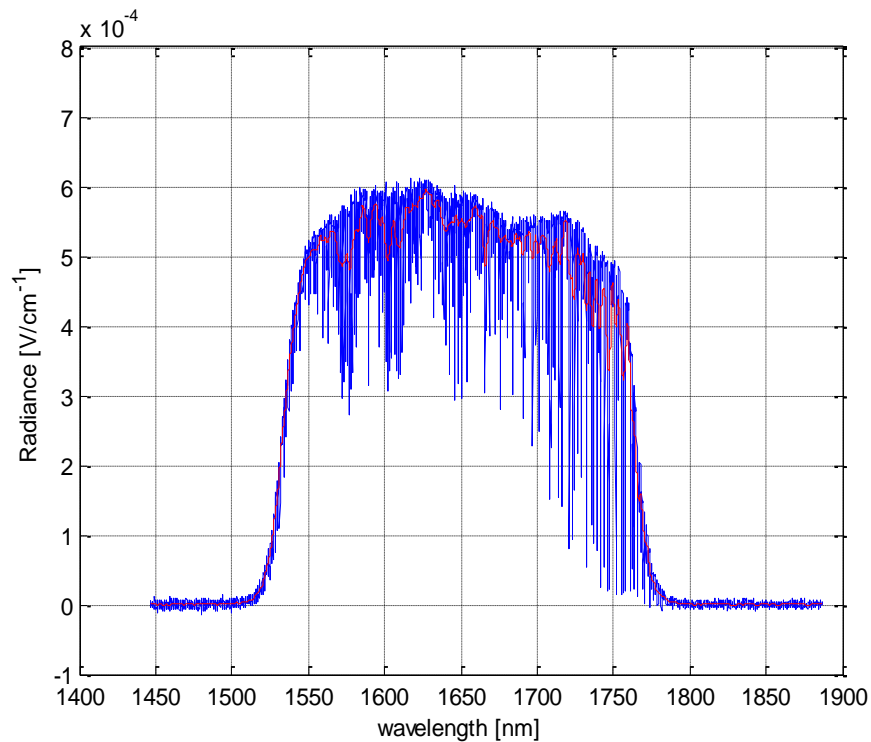


Fig. 74: GOSAT spectrum radiance (blue) and its smoothed variation (red).

The upper part of the Fig. 75 shows the radiance over 1560 to 1640 nm near IR spectral range between GOSAT observation smoothed radiance (blue) and Argus 1000 observation radiance (red). Their residue of the radiance data is shown in lower part in

the Fig. 75. We can see the reasonable match between two curves of the radiance data in this spectral window. Given the width of the CO₂ bands, all data points in this region are correlated with CO₂ amount. Both data sets are collected on October 27, 2009 over Atlantic Ocean.

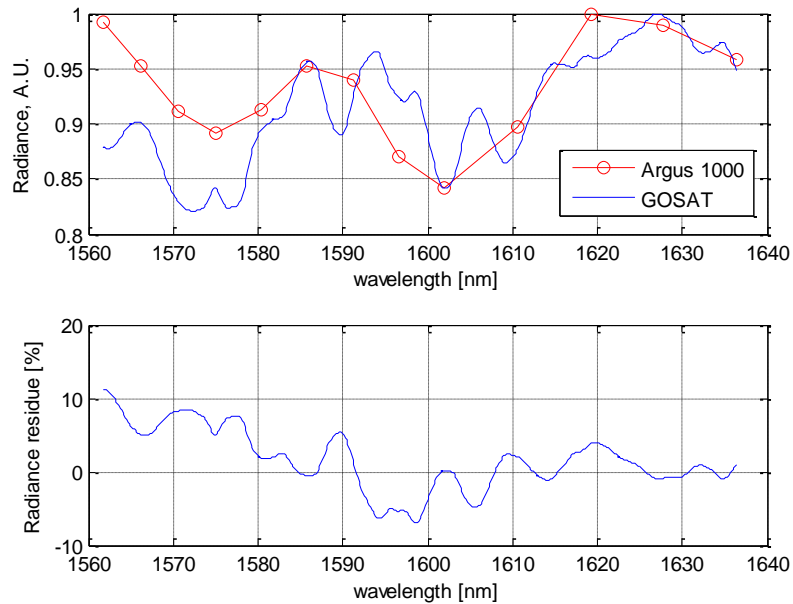


Fig. 75: Comparison of GOSAT and Argus radiance observations (upper panel) and difference of GOSAT and Argus measured radiance (lower panel).

5.9 Errors Analysis

This section describes the various error sources contributing to the Argus calibration and retrieval processes.

5.9.1 Errors Wavelength Calibration

As described previously, the calibration for Argus wavelength is derived from two parts: a ground-based calibration using lasers and a space-based calibration utilizing the

atmosphere. Analysis indicates less than 2% variation between the wavelength assignments for each method. As the atmosphere contains a significantly larger number of features than can be generated with five lasers it is likely that this calibration method improves the overall wavelength calibration accuracy. However, we base our wavelength error analysis on the more conservative laser calibration approach. Our analysis takes into account errors related to laser instabilities. These include the power drift and wavelength fluctuation. Our gas-tube lasers are regarded as highly stable and frequency shifts for these lasers are less than 100 ppb over the tube lifetime. This indicates that the wavelength range of such fluctuation with respect to the laser centre wavelength λ_0 does not exceed ± 0.002 nm. The diode laser utilized has significantly poorer stability performance of approximately ± 1 nm and has a line-width which is relatively broad. Consequently, our wavelength error accuracy is dependent mainly on our gas laser results. Our tests indicate that the lasers utilized in testing are highly stable and spectrometer reading fluctuated less than 2.0 counts (0.19%) with a co-adding setting of two. Power fluctuations were not seen to contribute to wavelength variations and compared to other sources of errors are neglected. The main source of error is the assignment of a particular pixel to each laser frequency. It is difficult to assign exactly this frequency and consequently, this uncertainty is estimated at ± 2 pixels (1.2%).

The other sources of errors are in laser calibration includes:

- 1) Uncertainty in pixel position assuming 12 nm errors at 1000 nm (1.2 %).
- 2) Fluctuation in laser beam intensity assuming 0.002 nm at 1000 nm (0.0002%).

Consequently, the wavelength calibration total root mean squared error is found to be 1.2%. The error is further mitigated by utilizing gas absorption features to calibrate on orbit.

5.9.2 Error due to Radiance Calibration

The overall laboratory radiometric calibration accuracy depends on various factors, including the accuracy of calibration sources and surfaces, the accuracy to which the set-step can be measured and the accuracy of the spectrometer. The error analysis for the radiance calibration includes the following factors:

- 1) Lamp blackbody calibration accuracy (drift – in wavelength and in power)
- 2) Uncertainty in the angle between screen and source (or angle between normal to screen and source).
- 3) Source linear position during calibration.
- 4) NIST (standard) screen uncertainties.
- 5) Spectrometer sensitivity.

In the calibration procedure, two factors leading to the measurement error have to be taken into account. The first factor is the drift of the radiant power, which depends upon time as the characteristics of the ORIEL lamp (Oriel, standard NIST SRS-99-020-REFL-48) used for calibration which deteriorates with usage. According to the lab manual the drift of the irradiance ranges between 0.35% to 1.6%. This drift occurs mostly due to aging of the lamp and also due to small variations of the output voltage generated by the highly stabilized power supply (Oriel kit). Due to these reasons we can take an average value for the drift to be 0.83%. The second factor is the measurement

error arising due to uncertainty in angle. We follow the typical procedure in assumption of the uncertainty in angle by taking its value as half of the smallest scale of the protractor that is $\pm 0.25\%$. In order to convert radiant power measurements into spectral radiance the source is placed a known distance from the screen. Best results were obtained for 12 m range. The uncertainty in the distance between the light source and the detector is 10 mm which is equivalent to 0.08%. The spectrometer records measurements with a stability of approximately 2.0 counts.

Apart from the errors related to the drift, linear position, measurement noise and angle uncertainty, we have to take into account that the reflectance factor of the white screen is less than unity. Strictly, the reflectance factor $f(\lambda)$ is a function of the wavelength and incident and emergent angle. However within the wavelength range of interest (1550–1650 nm), the reflectance factor can be taken to be $f(\lambda = 1600 \text{ nm}) = 0.987$, according to Fig. 23.

From Table 10 we can conclude that the overall error in radiant power is mostly due to the uncertainty in spectrometer counts and the drift of the ORIEL lamp. Therefore the total error in calibration is in good agreement with the error measurement specifications listed in the Argus 1000 documentation. This table also shows the radiant power and the corresponding errors due to power drift and pointing-angle uncertainty. The corresponding RMS of the total error within the range 1500 to 1650 nm is $7.32 \times 10^{-6} \text{ W}$.

Table 10: Errors in calibration parameters.

Wavelength, [nm]	Error due to Radiant power drift [W]	Error, assuming an angle uncertainty $\pm 0.25^\circ$, [W]	Error in source location $\pm 0.08\%$ [W]	Error in Lambertian Screen at 1.25% [W]	Error in spectrometer sensitivity at 0.19% [W]	Total error, [W]
1500	9.90e-007	1.74e-006	4.73e-008	4.64e-006	2.65e-007	7.68e-006
1550	9.27e-007	1.63e-006	4.68e-008	4.61e-006	2.55e-007	7.45e-006
1600	8.66e-007	1.52e-006	4.59e-008	4.56e-006	2.48e-007	7.18e-006
1650	8.10e-007	1.42e-006	4.45e-008	4.47e-006	2.24e-007	6.96e-006

5.9.3 Error in Gas Cell Measurements

Errors contributing to the gas cell calibration results include:

- 1) Uncertainty in gas concentration (density uncertainty 1 %).
- 2) Uncertainty in length of the cell ($1\text{m} \pm 0.002 = >0.2\%$) – as uncertainty $\Delta L = 2\text{mm}$.
- 3) Variation of lamp intensity and spectrometer over course of experiment. This uncertainty is estimated as 2 spectrometer counts for each measurement (with and without CO₂ or 0.19% for each measurement).

The total error in this gas cell calibration is 1.02% (in absorption).

5.9.4 Error due to Geolocation Analysis

The sources of error present in geolocation analysis of the Argus data result from uncertainties including:

- 1) Attitude Uncertainty
- 2) Position (2 Line Element) Uncertainty
- 3) Time Uncertainty.

The attitude uncertainty of Argus observations are estimated as approximately $\pm 1^\circ$ in longitude and latitude. This error introduced from the TLE and SGP4 is predicted to be about 12.2 km error along and across the satellite track. The position error along and across the satellite track using two-line element is 1.9 km. The onboard timing system has a maximum uncertainty of 1.0 second (one sigma), which translates to an along-track position uncertainty 7.5 km at the spacecraft velocity of 7.5 km/s. This then translates into maximum geolocation errors of 21.63 km along-track or 14.88 km cross-track at nadir. We take a simple root mean squared sum of the uncertainties as a conservative worst case estimation of the geolocation uncertainty [Chesser *et. al*, 2011].

The Table 11 summarizes the major uncertainties due to geolocation error of Argus. Red ellipse in Fig. 52 shows this uncertainty zone.

Table 11. Uncertainties in Position and Time.

	Along Track (km)	Cross Track (km)
Attitude Uncertainty	12.21	12.21
Position (2 Line Element)	1.92	1.92
Time Uncertainty Error	7.50	0.75
RMS	21.63	14.88

5.9.5 Error in Retrieval Analysis

The retrieval algorithm includes a method of sensitivity analysis to assign error bars to estimates of retrieved gas-mixing ratios. After the estimator has converged to produce a set of best-fit mixing ratios, a sensitivity ratio is computed. Working sequentially by gas, the best-estimate mixing ratio is perturbed by 1% in order to determine the corresponding change in radiance at each atmospheric layer following [Park, 1997]. Using this method, at very high spectral resolution, the peak sensitivity ratio for CO₂ is determined as a factor of 2.0 (a 1% change in CO₂ causes a 2% change in peak radiance). When averaged to the resolution of the Argus instrument, the sensitivity to 1% CO₂ is reduced to 0.12% or 0.41 instrumental counts, as discussed previously. Orbital spectra acquired over constant scenes appear highly repeatable and, consequently instrument precision is determined by the quantization noise as approximately 1.0 count. The error due to this quantization is equivalent to a CO₂ sensitivity of 2.5% per pixel that is correlated with CO₂. Approximately five Argus pixels are highly correlated with CO₂ amount, and consequently, statistical averaging can increase sensitivity by the square root

of the sample set or a factor 2.2. An additional performance gain of a factor of up to 3.3 can be made by the hardware co-adding of up to 10 spectra; however this enhancement comes at the expense of spatial resolution.

Other major sources of errors in the retrieval analysis are uncertainty in nadir angle, Sun zenith angle, equivalent black-body Sun temperature, background reflectance (surface albedo).

Uncertainty in nadir angle and Sun zenith angle is taken to be $\pm 0.5^\circ$ as a result of uncertainty in time/position of the spectrometer as presented in section 5.9.4. Realistically these uncertainties are quite conservative. Nevertheless we have taken a worse case scenario by increasing it up to $\pm 0.5^\circ$. Uncertainty of the solar temperature fitting, 10° C, is related to two main reasons. The first reason, the Sun behavior is not entirely similar to a black body and exhibits daily variability. The second reason, the temperature of the Sun is determined by the peak in its radiance that is not located at the IR spectral position where our measurements are recorded. The uncertainty caused by error in albedo fitting is estimated empirically from the fitting parameters in the retrieval as 0.1%.

A root-mean-square (RMS) residual is calculated between the simulated (fitted) and measured radiance in the neighbourhood of the absorption window for a specific absorbing gas species. Table 12 shows the average and RMS errors due to standard uncertainties. The accumulated (total) error can be estimated by analyzing the effect of these uncertainties. The uncertainty in the viewing (nadir) and Sun elevation corresponds to an error in estimation of CO₂ mixing ratio of approximately 2.5% at a

satellite/instrument altitude of 700 km. Radiance error, blackbody temperature error, and viewing angle error are added in quadrature to obtain the total error as a function of altitude. Our total errors are in a reasonable agreement with those of similar measurements published elsewhere. Line spectra knowledge error is derived from Rothmann *et al.*, (2006).

Table12: Radiance average and RMS errors due to uncertainties
in measurements (co-adding setting of 1.0).

Parameter	Uncertainty	Average Error [W m ⁻² sr ⁻¹ (cm ⁻¹) ⁻¹]	Percent. Diff. [%]
Nadir Angle	± 0.5°	1.12×10 ⁻⁷	0.04
Solar Angle knowledge	± 0.5°	4.63×10 ⁻⁶	1.65
Albedo fit	0.1%	1.8×10 ⁻⁶	0.64
solar Temp. fit	10 °C	1.14×10 ⁻⁷	0.05
Line Spectra knowledge	3 %	8.40×10 ⁻⁶	3.0
Instrument Noise (per pixel)	2.5 %	7.04×10 ⁻⁶	2.5
Total RMS Error	–	1.22×10 ⁻⁶	7.85

Our retrieval methodology computes a root-mean-square (RMS) residual is between the fitted and measured radiance spectra. In the region of the CO₂ band around 1600 nm our results indicate that this residual error is comparable with the theoretical error analysis presented above. Since the measurement of CO₂ column is dependent on the count differential between pixels with and without sensitivity to CO₂ the error in absolute column is 7.85%. We note however that the measurement precision is significantly higher than this. If a variability of 1.0 count is assumed, then our instrumentation can record radiance data highly correlated to CO₂ amount with a

statistical precision of 0.71% of column when fitting five correlated pixels and with a co-adding setting of 2.0. In the space-based identification of sources and sinks the measurement precision is likely a more important factor than absolute radiance calibration as small local variations in radiance may be attributable to the presence of sources and sinks when factors such as cloud variability are absent.

6.0 CONCLUSIONS

A small, light and inexpensive micro-spectrometer operating in near IR spectral region was calibrated and tested at the space test facility at York University. The radiometric, wavelength, slit function, angular sensitivity calibrations are presented. Space simulation testing is performed to verify flight operation. With three years of orbital heritage on its first flight, the miniature spectrometer meets all requirements for stable and durable operation in Earth orbit. Applying GENSPECT as the tool to model radiative transfer, the retrieval of preliminary data products from Argus is generated. With measurement data obtained from the Argus instrument, the column of the CO₂ & H₂O gases contributing to greenhouse emission can be monitored from radiance measurements. Our results indicate that even for clear sky observations the CO₂ absorption is typically 1.20 times higher than predicted by theoretical absorption models. Our assumption of no multiple scattering in the model, and a simple linear path may provide an explanation as to why 1.20 times the expected abundance of CO₂ was required to match with experimental radiance. If, for example, 20% of photons incident at the instrument are indirect, then an enhanced CO₂ concentration of 1.20 would be required to match instrumental results under a linear path assumption. Photons following an indirect or multiple scattering path are subject to approximately double the path of a single line path. Our conclusion is therefore that a simple linear path approximation does not account adequately for CO₂ absorption, even on nearly cloud free scenes.

Our flight experience indicates that data received from the instrument and its assimilated retrieval results show the stable and reliable performance under space

conditions. For each set of space data received from Argus, the corresponding geolocation is determined in near real time basis. With a much higher density of observations this approach enables us to monitor globally the same events related to greenhouse gases emission.

In summary, our major findings with Argus spectrometer are that:

- 1) Clouds and water vapour appear to be far more radiatively dominant in this important spectral region 1000 nm to 1700 nm compared to CO₂.
- 2) With present Argus instrument carbon dioxide can be detected; its measurement accuracy can be improved further by more precise calibration and geolocation determination.
- 3) Absorption by CO₂ likely exceeds significantly the amounts presumed in current climatology models because the presence of clouds has an amplifying effect on radiation absorption by CO₂ molecules. We conclude that a linear path radiative transfer model used for our analysis may be insufficient to describe atmospheric CO₂ absorption due to the effect of multiple scattering effects by clouds as discussed earlier on pages 107 and 108.
- 4) We report the first actual experimental results for nadir NIR spectra in the scientific literature for the 1100-1700 nm window.
- 5) We have demonstrated that the low-cost miniature sensors, commensurate with flight on cube-sat sized spacecraft can make significant contributions to the understanding of the Earth's radiation budget.

There is no physical reason to believe that significant calibration errors would arise between adjacent detector pixels located on and off the CO₂ absorption feature. Consequently, because the CO₂ absorption is spectrally localized, calibration error cannot provide a suitable explanation for additional absorption. Further, we record two distinct CO₂ bands that have exactly the same behavior. Although we compute a comprehensive absolute radiance synthetic fit, this is not required for CO₂ retrieval. A simple ratio approach between on-band and off-band absorption can provide similar results to our more comprehensive analysis but will not estimate error or provide calibrated concentration units that are quantifiable from radiance calibration. Our modeling approach uses the same methodology as that proposed by the OCO team. In summary, there is no suitable instrument or linear-path retrieval related explanation that can describe the additional absorption by CO₂ that would be expected from our linear path analysis. Consequently, we conclude that the additional absorption by CO₂ seen by Argus is present in raw radiance data may be due to multiple scattering. Indeed, by visual inspection of the radiance figures, it is obvious that CO₂ absorption is stronger than predicted by current models including those presented by the OCO team as shown in Fig. 5, [Miller *et al.*, 2005].

Improvements to geolocation performance can be made by improvement in attitude knowledge through the use, for example, of a star camera to augment the CanX-2 onboard attitude sensors (magnetometer, rate sensors and sun sensor). Star cameras utilizing sub-pixel interpolation techniques to centroid star locations can provide arc second accuracy [Lee *et. al*, 2008]. Better time certainty and resolution will improve the

along-track geolocation performance significantly. While this issue is mainly related to the spacecraft bus system, future instrument versions may include a frame timer. We are currently examining ways to model and analyze the sensor noise, and design the compensation algorithm to fuse the data for attitude measurement. Alignment, a leading cause of attitude error, is extremely expensive to realize in hardware. By implementing an adaptive Kalman Filter with a compensation algorithm, we are seeking an alternative method to determine the spacecraft attitude using low-cost sensors [Chesser *et. al*, 2011]. The geolocation errors highlight the need for better attitude knowledge and better control accuracies for future operational missions employing the Argus spectrometer.

The Argus instrument onboard CanX-2 has demonstrated the potential of nanosatellites to perform significant science missions. Argus has been collecting science data following since December 2008. In total, 143 sets of data were successfully observed and analyzed to date. About 30% of the observation sets were acquired over area targets centered over the ocean. Overall, major cities make up about 24% of the total observation sets obtained. Argus instruments orbiting the Earth can provide a globally accepted standard dataset for improving our understanding of the carbon cycle and carbon sources and sinks.

6.1 Future Work

Now that broad-band measurements of IR radiance have been recorded by the CanX-2 Argus, future instrumentation may benefit from enhanced resolution of the CO₂ band at the expense of observing the Oxygen A-band. In addition, radiative transfer model that accounts for multiple path scattering by clouds and aerosols will be desirable

for more accurate data retrieved. The use of a full Monte Carlo scattering model to counter the multiple scattering problems should be considered, since the effect of anthropogenic carbon dioxide enhancement on the environment cannot be adequately modeled without accounting for scattering effects. This activity could form the basis of a future Ph.D. investigation.

Further work is required to compare observations to other similar space instruments and analyze future data to be acquired by the Argus instrument. Some modifications to Argus have been completed recently and configuration options including "gold optics", "space certified", and "extended range" are already available. Methodologies for the operation of small collective networks of Argus (and Argus-like) instruments should be investigated. This will further facilitate the continuous monitoring of anthropogenic activities. Argus 1000-type instruments can be also used for scientific exploration on the surface or in the orbit of the extraterrestrial planets for the detection of sources of water vapour and other molecular gases. Absorption by O₂ at 1260 nm should be investigated further for use as a proxy measurement for atmospheric path density. Observations of the Oxygen-A band may be needed as an additional data set. In future instruments we propose an on-orbit calibration set up, which will update radiometric coefficients, the signal-to-noise ratio, and the bad-pixel map. These updates could be repeated on a cycle of 7 days.

We also propose the measurement of CO₂ in the strong band at 2040-2080 nm. CO and a variety of other gases have strong, well-resolved spectral lines in this region,

which can be used for retrieval of low-resolution profiles, are observable by an extended range Argus.

Argus spectral resolution can be improved but at the expense of a broad range radiative environment measurement that carries more information content regarding energy balance and exchange. Broad spectral range provides environment for the magnitude of CO₂ absorption. Future space missions may carry sets of Argus instruments each tuned to a particular spectra range and species. Instruments may be developed to observe aerosols.

REFERENCES

- Aben I., Hasekampa O., and Hartmann W.: Uncertainties in the space-based measurements of CO₂ columns due to scattering in the Earth's atmosphere, *J. Quant. Spectrosc. Radiat. Transfer*, 104, 3, 450-459, 2007.
- Abrarov, S. M., Quine, B. M., and Jagpal, R. K.: A simple interpolating algorithm for the rapid and accurate calculation of the Voigt function, *J. Quant. Spectrosc. Radiat. Transfer*, 110, 376-383, 2009.
- Abrarov, S. M., Quine, B. M., and Jagpal, R. K.: Rapidly convergent series for high-accuracy calculation of the Voigt function, *J. Quant. Spectrosc. Radiat. Transfer*, 111, 372-375, 2010a.
- Abrarov, S. M., Quine, B. M., Jagpal, R. K., High-accuracy approximation of the complex probability function by Fourier expansion of exponential multiplier, *Comp. Phys. Commun.*, 181, 876-882, 2010b.
- Armstrong, B. H. and Nicholls, B. W., *Emission, absorption and transfer of radiation in heated atmospheres*, Pergamon Press, New York, 229-234 1972,.
- Atkinson P. M.; Cutler M. E. J.; Lewis H., Mapping sub-pixel proportional land cover with AVHRR imagery; *International Journal of Remote Sensing*, 18, 917-935, 1997.
- AVHRR (Advanced Very High Resolution Radiometer) Google Earth Imagery, downloaded from Space Science and Engineering Centre, <http://ge.ssec.wisc.edu/avhrr/>.

- Barkley, M. P., Frieß, U., and Monks, P. S.: Measuring atmospheric CO₂ from space using Full Spectral Initiation (FSI) WFM-DOAS, *Atmos. Chem. Phys.*, 6, 3517–3534, 2006a.
- Barkley, M. P., Monks, P. S., and Engelen, R. J.: Comparison of SCIAMACHY and AIRS CO₂ measurements over North America during the summer and autumn of 2003, *Geophys. Res. Lett.*, 33, L20805, doi:10.1029/2006GL026807, 2006b.
- Barkley, M. P., Monks, P. S., Frieß, U., Mittermeier, R. L., Fast, H., Körner, S., and Heimann, M.: Comparisons between SCIAMACHY atmospheric CO₂ retrieved using (FSI) WFM-DOAS to ground based FTIR data and the TM3 chemistry transport model, *Atmos. Chem. Phys.*, 6, 4483–4498, 2006c.
- Barkley, M. P., Monks, P. S., Hewitt, A. J., Machida, T., Desai, A., Vinnichenko, N., Nakazawa, T., Yu Arshinov, M., Fedoseev, N., and Watai, T.: Assessing the near surface sensitivity of SCIAMACHY atmospheric CO₂ retrieved using (FSI) WFM-DOAS, *Atmos. Chem. Phys.*, 7, 3597–3619, 2007.
- Benner, C. D., Rinsland, C. P., Devi, V. M., Smith, M. A. H., and Atkins D.: A Multispectrum Nonlinear Least Squares Fitting Technique, *J. Quant. Spectrosc. Radiat. Transfer*, 53, 705, 1995.
- Bösch, H., Toon, G. C., Sen, B., Washenfelder, R. A., Wennberg, P. O., Buchwitz, M., de Beek, R., Burrows, J. P., Crisp, D., Christi, M., Connor, B. J., Natraj, V., and Yung, Y. L.: Spacebased near- infrared CO₂ measurements: Testing the Orbiting Carbon Observatory retrieval algorithm and validation concept using SCIAMACHY

- observations over Park Falls, Wisconsin, *J. Geophys. Res.*, 111, D23302, doi:10.1029/2006JD007080, 2006
- Buchwitz, M. and Burrows, J. P.: Retrieval of CH₄, CO, and CO₂ total column amounts from SCIAMACHY near-infrared nadir spectra: Retrieval algorithm and first results, in: *Remote Sensing of Clouds and the Atmosphere VIII*, edited by: Schäfer, K. P., Comèron, A., Carleer, M. R., and Picard, R. H., *Proceedings of SPIE*, 5235, 375–388, 2004.
- Buchwitz, M., De Beek, R., Burrows, J. P., Bovensmann, H., Warneke, T., Notholt, J., Meirink, J. F., Goede, A. P. H., Bergamaschi, P., Körner, S., Heimann, M., and Schulz, A.: Atmospheric methane and carbon dioxide from SCIAMACHY satellite data: initial comparison with chemistry and transport models, *Atmos. Chem. Phys.*, 5, 941–962, 2005a.
- Buchwitz, M., De Beek, R., Noel, S., Burrows, J. P., Bovensmann, H., Bremer, H., Bergamaschi, P., Körner, S., and Heimann, M.: Carbon monoxide, methane and carbon dioxide columns retrieved from SCIAMACHY by WFM-DOAS: year 2003 initial data set, *Atmos. Chem. Phys.*, 5, 3313–3329, 2005b.
- Buchwitz, M., Reuter, M., Schneising, O., Heymann, J., Bovensmann, H., and Burrows, J. P., Towards an improved CO₂ retrieval algorithm for SCIAMACHY on ENVISAT, *Proceedings Atmospheric Science Conference, Barcelona, Spain, 7-11 Sept 2009*, ESA Special Publication SP-676, 2009.
- Buchwitz, M., Rozanov, V. V., and Burrows, J. P.: A correlated-k distribution scheme for overlapping gases suitable for retrieval of atmospheric constituents from moderate

- resolution radiance measurements in the VIS/NIR spectral region, *J. Geophys. Res.*, 105, 15 247–15 261, 2000a.
- Buchwitz, M., Rozanov, V. V., and Burrows, J. P.: A near-infrared optimized DOAS method for the fast global retrieval of atmospheric CH₄, CO, CO₂, H₂O, and N₂O total column amounts from SCIAMACHY Envisat-1 nadir radiances, *J. Geophys. Res.*, 105, 15 231–15 245, 2000b.
- Buchwitz, M., Rozanov, V. V., and Burrows, J. P., A near-infrared optimized DOAS method for the fast global retrieval of atmospheric CH₄, CO, CO₂, H₂O, and N₂O total column amounts from SCIAMACHY Envisat-1 nadir radiances, *J. Geophys. Res.*, 105, 15, 231-15, 245, 2000.
- Buchwitz, M., De Beek, R., Burrows, J. P. *et al.*, Atmospheric methane and carbon dioxide from SCIAMACHY satellite data: initial comparison with chemistry and transport models, *Atmos.Chem. Phys.*, 5, 941-962, 2005.
- Buchwitz, M., Schneising, O., Burrows J. P. *et al.*, First direct observation of the atmospheric CO₂ year-to year increase from space, *Atmos. Chem. Phys.*, 7, 4249-4256, 2007.
- Buchwitz, M., Reuter, M., and Schneising, O., Towards an improved CO₂ retrieval algorithm for SCIAMACHY on ENVISAT, Proceedings Atmospheric Science Conference, Barcelona, Spain, 7-11 Sept 2009, ESA Special Publication SP-676 (CD-ROM), 2009.

- Burkert, P.; Fergg, F.; Fischer, H.: A Compact High-Resolution Michelson Interferometer for Passive Atmospheric Sounding (MIPAS);IEEE Geoscience and Remote Sensing Society, April 345 - 349 , 2007.
- Chedin, A., Hollingsworth, A., Scott, N. A., Serrar, S., Crevoisier, C., and Armante, R.: Annual and seasonal variations of atmospheric CO₂, N₂O and CO concentrations retrieved from NOAA/TOVS satellite observations, *Geophys. Res. Lett.*, 29, doi:10.1029/2001GL14 082, 2002a.
- Chedin, A., Serrar, S., Armante, R., Scott, N. A., and Hollingsworth, A.: Signatures of annual and seasonal variations of CO₂ and other greenhouse gases from comparisons between NOAA TOVS observations 5 and radiation model simulations, *J. Climate*, 15, 95–116, 2002b.
- Chesser, H., Lee, R., Jagpal, R., and Quine, B.: Geolocation of Argus Flight Data, Proceedings of the International Conference on Space Technology, Thessaloniki, Greece, 2009.
- Chesser, H., Lee, R., Benari G., Jagpal, R., Lam K., and Quine, B.: Geolocation of Argus Flight Data, *IEEE Trans. on Geoscience and Remote Sensing (TGRS)*, 2011 (submitted)
- Chevallier, F., Bréon, F.-M., and Rayner, P. J.: Contribution of the Orbiting Carbon Observatory to the estimation of CO₂ sources and sinks: Theoretical study in a variational data assimilation framework, *J. Geophys. Res.*, 112, 2007.

- Crisp, D., Atlas, R. M., Bréon, F.-M., Brown, L. R., Burrows, J. P., Ciais, P., Connor, B. J., Doney, S. C., Fung, I. Y., Jacob, D. J., Miller, C. E., O'Brien, D., Pawson, S., Randerson, J. T., Rayner, P., Salawitch, R. J., Sander, S. P., Sen, B., Stephens, G. L., Tans, P. P., Toon, G. C., Wennberg, P. O., Wofsy, S. C., Yung, Y. L., Kuang, Z., Chudasama, B., Sprague, G., Weiss, B., Pollock, R., Kenyon, D., and S. Schroll: The Orbiting Carbon Observatory (OCO) mission, *Adv. Space Res.* 34, 700-709, 2004.
- Deutscher, N. M., Griffith, D. W. T., Bryant, G. W., Wennberg, P. O., Toon, G. C., Washenfelder, R. A., Keppel-Aleks, G., Wunch, D., Yavin, Y., Allen, N. T., Blavier, J.-F., Jiménez, R., Daube, B. C., Bright, A. V., Matross, D. M., Wofsy, S. C., and Park, S.: Total column CO₂ measurements at Darwin, Australia – site description and calibration against in situ aircraft profiles, *Atmos. Meas. Tech.*, 3, 947-958, 2010.
- Drummond J. R., Brasseur, G. P., Davis, G. R., Gille, J. C., McConnell, J. C., Pesket, G. D., Reichle, H. G., and Roulet N.: MOPITT Mission Description Document, Department of Physics, University of Toronto, 1993, www.atmosp.physics.utoronto.ca/mopitt/mdd_93/index.html
- Drummond J. R. and Mand, G. S.: Measurement of pollution in the troposphere (MOPITT) instrument: Overall performance and calibration requirement, *J. Atm. Ocean. Tech.* 13, 314-320, 1996.
- Drummond, J. R., Hipkin, V. J., Tolton, B., Strong, K., Quine, B. M., Rivard, B. A., Caldwell, J. J., McConnell, J. C., Davis, G. R., Chateaufneuf, F., and Hackett, J.: A Canadian atmospheric and geological mission to Mars, *Geosci. Remote Sens. Symp. IGARSS , IEEE International*, 4, 2166 – 2168, 2002.

- Duggan P., Sinclair, P. M., LeFlohic, M. P., Forsman, J. W., Berman, R., May, A. D., and Drummond, J. R.: Testing the Validity of the Optical Diffusion Coefficient: Line-Shape Measurements of CO Perturbed by N₂, *Phys. Rev. A*, 48, 2077-2083, 1993.
- Dufour, E., Breon F.-M Spaceborne estimate of atmospheric CO₂ column by use of the differential absorption method: error analysis, *Appl. Opt.*, 42, 3595-3609, 2003.
- Dufour, D. G.; Drummond, J. R.; McElroy, C. T.; Midwinter, C.; Bernath, P. F.; Walker, K. A.; Evans, W. F. J.; Puckrin, E.; Nowlan, C., Intercomparison of Simultaneously Obtained Infrared (4.8 μm) and Visible (515-715 nm) Ozone Spectra Using ACE-FTS and MAESTRO. *J. Phys. Chem.*, 109, 8760-8764, 2005.
- Dufour, D. G., Drummond, J. R., McElroy, C. Th., Midwinter, C., Bernath, P. F., Walker, K. A., and Nowlan, C.: Simultaneous measurements of visible (400-700 nm) and infrared (3.4 μm) NO₂ absorption, *J. Phys. Chem. A*, 110, 12414–12418, 2006.
- Dufour, D. G., Drummond, J. R., McElroy, C. Th., Midwinter, C., Bernath, P. F., Walker, K. A., Evans, W. F. J., Puckrin, E., and Nowlan C.: Intercomparison of simultaneously obtained infrared (4.8 μm) and visible (515–715 nm) ozone spectra using ACE-FTS and MAESTRO, *J. Phys. Chem. A*, 109, 8760–8764, 2005.
- Eagleson, Stuart. “Canadian Advanced Nanospace Experiment 2: Scientific and Technological Innovation on a Three-Kilogram Satellite,” IAC. <http://www.utias-sfl.net/docs/canx2-iac-2005>.
- Engelen, R. J., Scott Denning, A., Gurney, K. R., and Stephens, G. L.: Global observations of the carbon budget, Expected satellite capabilities in the EOS and NPOESS eras, *J. Geophys. Res.*, 106, 20,055–20,068, 2001.

- Frohlich C. and Shaw G. E, New determination of Rayleigh scattering in the terrestrial atmosphere. *Appl. Opt.* 19, 1773, 1980.
- Gao, S., Clark, K., Unwin, M., Zackrisson, J.; Shiroma, W.A., Akagi, J.M., Maynard, K., Garner, P., Boccia, L., Amendola, G., Massa, G., Underwood, C., Brenchley, M., Pointer, M. & Sweeting, M.N. (2009). Antennas for modern small satellites. *IEEE Antennas and Propagation Magazine*, 51, 4, 40–56, 2009
- Gottwald, M., Bovensmann, H., Lichtenberg, G., Noël, S., Von Bargaen, A., Slijkhuis, S., Piders, A., Hoogeveen, R., Von Savigny, C., Buchwitz, M., Kokhanovsky, A., Richter, A., Rozanov, A., Holzer-Popp, T., Bramstedt, K., Lambert, J.-C., Skupin, J., Wittrock, F., Schrijver, H., and Burrows, J. P.: *SCIAMACHY, Monitoring the Changing Earth's Atmosphere*, DLR, Institut für Methodik der Fernerkundung, 79-84, 2006.
- Houweling, S., Breon, F.-M., Aben, I., Rödenbeck, C., Gloor, M., Heimann, M., and Ciais, P.: Inverse modeling of CO₂ sources and sinks using satellite data: a synthetic inter-comparison of measurement techniques and their performance as a function of space and time, *Atmos. Chem. Phys.*, 4, 523–538, 2004.
- Houweling, S., Hartmann, W., Aben, I., Schrijver, H., Skidmore, J., Roelofs, G.-J., and Breon, F.-M.: Evidence of systematic errors in SCIAMACHY-observed CO₂ due to aerosols, *Atmos. Chem. Phys.*, 5, 3003–3013, 2005.
- Jacobson M. Z.: The enhancement of local air pollution by urban CO₂ domes, *Environmental Science & Technology* 2009.

- Jagpal, R. K., Quine, B. M., Chesser, H., Abrarov S., and Lee R.: Calibration and in-orbit performance of the Argus 1000 spectrometer - the Canadian pollution monitor, *J. Appl. Rem. Sens. Lett.* 4, 049501, 2010.
- Jagpal, R. K.; Quine, B.; Abrarov, S. M.; Lee, R.; Chesser, H.; McKernan, E.; Bhattacharya, Y. Carbon Dioxide Retrieval from Space Spectral Data of ARGUS 1000 Spectrometer, American Geophysical Union, Fall Meeting 2009, [abstract #A51A-0087](#).
- Jounot, L. J. and Drummond, J. R.: Measurements of pollution in the troposphere-aircraft (MOPITT-A), *Geosci. Remote Sens. Symp.*, 2002. IGARSS '02. 2002 IEEE International, 6, 3180 - 3182, 2002.
- Koner, P. K., Drummond, J. R., Atmospheric trace gases profile retrievals using the nonlinear regularized total least square method, *JQSRT*, 109, 2045–2059, 2008.
- Koner, P. K. and Drummond, J. R.: A Minimized Mutual Information retrieval for simultaneous atmospheric pressure and temperature, *ArXiv*: <http://arxiv.org/abs/1012.4792>
- Kuang, Z., Margolis, J., Toon, G., Crisp, D., and Yung, Y.: Spaceborne measurements of atmospheric CO₂ by high-resolution NIR spectrometry of reflected sunlight: an introductory study, *Geophys. Res. Lett.* 29, 1716-1720, 2002.
- Kuze A., Suto H., Nakajima M., and Hamazaki T.: Initial Onboard Performance of TANSO-FTS on GOSAT' Conference Paper Fourier Transform Spectroscopy (FTS) Vancouver, Canada April 30, 2009

- Lee, R., Cantata M., Quine B. and Hornsey R.: Performance Analysis of Centroiding Algorithm Using a New Sub-pixel Interpolation Technique. Canadian Aeronautics & Space Institute ASTRO 2008 Conference, Montreal, April 2008.
- Mao J. and Kawa, S. R.: Sensitivity studies for space-based measurement of atmospheric total column carbon dioxide by reflected sunlight, *Appl. Opt.* 43, 914-927, 2004.
- McKernan, E., Quine, B. M., and Drummond, J. R., MOPITT sensitivity studies: Computation of instrument parameter dependencies, 2002 IEEE International Geoscience and Remote Sensing Symposium (IGARSS) 2, 1102 - 1104, 2002.
- McKernan, E. P., Tolton, B. T., Drummond, J. R., and Yurganov, L.: MOPITT Validation Using Ground-Based IR Spectroscopy, SPIE annual general meeting, 1999.
- Miller C.E., Brown L.R., Toth R.A., Benner D.C., Devi V.M. Spectroscopic challenges for high accuracy retrievals of atmospheric CO₂ and the Orbiting Carbon Observatory (OCO) experiment , 876-887 , 2005.
- Miller, C.E., D. Crisp, P.L. DeCola, S.C. Olsen, J.T. Randerson, A.M. Michalak, A. Alkhaled, P. Rayner, D.J. Jacob, P. Suntharalingam, D.B.A. Jones, A.S. Denning, M.E. Nicholls, S. C. Doney, S. Pawson, H. Boesch, B.J. Connor, I.Y. Fung, D. O'Brien, R.J. Salawitch, , Sander, S. P., Sen, B., Tans, P., Toon, G. C., Wennberg, P. O., Wofsy, S. C., Yung, Y. L., and Law, R. M.: Precision requirements for space-based XCO₂ data, *J. Geophys. Res.*, 112, 2007.
- Nassar, R., Boone C., Walker K. A., McLeod S. D., and Bernath P. F.: SCISAT-1: Retrieval algorithms, ACE-FTS testing and the ACE database, *Proceedings of SPIE*,

- Vol. 5151 Earth Observing Systems VIII, edited by W. L. Barnes (SPIE, Bellingham, WA) pp 173-183, 2003.
- O'Brien, D. M., and P. J. Rayner, Global observations of the carbon budget, CO₂ column from differential absorption of reflected sunlight in the 1.61 um band of CO₂, J. Geophys. Res., 107(D18), 4354, (2002).
- Olsen, S. C. and Randerson, J. T.: Differences between surface and column atmospheric CO₂ and implications for carbon cycle research, J. Geophys. Res., 109, D02301, 10, 2004.
- Pagano, Th. S., Aumann, H. H., Hagen, D. E. and Oweroye K.: Prelaunch and in-flight radiometric calibration of the atmospheric infrared sounder (AIRS), IEEE Trans. Geosc. Rem. Sen. 41, 265-273 2003.
- Pak, B. C. and Prather, M. J., CO₂ source inversions using satellite observations of the upper troposphere, Geophys. Res. Lett., 28, 4571–4574, 2001.
- Park, J. H.: Atmospheric CO₂ monitoring from space, Appl. Opt., 36, 2701–2712, 1997.
- Picture taken from article “8 most polluted cities in India” using weblink
<http://www.green.in.msn.com/environmentalthreats>
- Quine, B. M. and Drummond, J. R.: GENSPECT: a line-by-line code with selectable interpolation error tolerance, J. Quant. Spect. Rad. Trans. 74, 147-165, 2002.
- Quine, B. M., Jagpal, R. and Ho A.: Argus – a Canadian Pollution Monitor: Instrument Overview, Proceedings of the 13th Canadian Astronautics Conference, ASTRO 2006, Montreal, QC, Canada, organized by Canadian Astronautics and Space Institute, April 25-27, 2006.

- Quine, B. M., M. Toohey, J. R. Drummond, K. Strong, D. Wunch, C. Midwinter, and C. T. McElroy, “The Concentration Profile of Nitric Acid and Other Species over Saskatchewan in August 1998: Retrieval from Data Recorded by Thermal-Emission Radiometry”, *Atmosphere- Ocean*, 43, 361-376, 2005.
- Rayner, P. J. and O’Brian, D. M.: The utility of remotely sensed CO₂ concentration data in surface inversions, *Geophys. Res. Lett.*, 28, 175–178, 2001.
- Rayner, P. J., R. M. Law, D. M. O’Brien, T. M. Butler, and A. C. Dilley (2002), Global observations of the carbon budget, 3, Initial assessment of the impact of satellite orbit, scan geometry, and cloud on measuring CO₂ from space, *J. Geophys. Res.* 107, 4557, 2002.
- Rayner, P., Jacob, D. J., Suntharalingam, P., Jones, D. B. A., Denning, A. S., Nicholls, M. E., Doney, S. C., Pawson, S., Boesch, H., Connor, B. J., Fung, I. Y., O’Brien, D., Salawitch, R. J., Reuter, M., Buchwitz, M., Schneising, O., Heymann, J., Bovensmann, H. and Burrows, J.P.: A method for improved SCIAMACHY CO₂ retrieval in the presence of optically thin clouds. *Atmospheric Measurement Techniques Discussions*, 2, 2483-2538, 2009.
- Reuter, M., Buchwitz, M., Schneising, O., Bovensmann, H., Burrows, J.P., Retrieval of atmospheric CO₂ from satellite near-infrared nadir spectra in a scattering atmosphere, *Geophysical Research Abstracts*, Vol. 11, EGU2009-1180, 2009.

- Rigby M., Toumi R., Fisher R, Lowry D, and Nisbet E. G.: First continuous measurements of CO₂ mixing ratio in central London using a compact diffusion probe, *Atmospheric Environment* 42 8943–8953, 2008.
- Rothman, L. S., Barbe, A., Benner, D. C., Brown, L. R., Camy-Peyret, C., Carleer, M. R., Chance, K., Clerbaux, C., Dana, V., Devi, V. M., Fayt, A., Flaud, J. M., Gamache, R. R., Goldman, A., Jacquemart, D., Jucks, K. W., Lafferty, W. J., Mandin, J. Y., Massie, S. T., Nemtchinov, V., Newnham, D. A., Perrin, A., Rinsland, C. P., Schroeder, J., Smith, K. M., Smith, M. A. H., Tang, K., Toth, R. A., Vander Auwera, J., Varanasi, P., and Yoshino, K.: The HITRAN molecular spectroscopic database: edition of 2000 including updates through 2001, *J. Quant. Spectrosc. Radiat. Transfer*, 82, 5–44, 2003.
- Rothman, L. S., Jacquemart, D., Barbe, A., Benner, D. C., Birk, M., Brown, L. R., Carleer, M. R., Chackerian, C., Chance, K., Coudert, L. H., Dana, V., Devi, V. M., Flaud, J.-M., Gamache, R. R., Goldman, A., Hartmann, J.-M., Jucks, K. W., Maki, A. G., Mandin, J.-Y., Massie, S. T., Orphal, J., Perrin, A., Rinsland, C. P., Smith, M. A. H., Tennyson, J., Tolchenov, R. N. Toth, R. A., Auwera, J. V., Varanasi, P., and G. Wagner,: The HITRAN 2004 molecular spectroscopic database, *J. Quant. Spectrosc. Radiat. Transfer* 96, 139-204, 2005.
- Rothman, L. S., Rinsland, C. P., Goldman, A., Massie, S. T., Edwards, D. P., Flaud, J. - M., Perrin, A., Camy-Peyret, C., Dana, V., Mandin, J. -Y., Schroeder, J., McCann, A., Gamache, R. R., Wattson, R. B., Yoshino, K., Chance, K. V., Jucks, K. W., Brown, L. R., Nemtchinov, V., and Varanasi, P.: The HITRAN Molecular Spectroscopic

- Database and Hawks (HITRAN Atmospheric Workstation): 1996 Edition, J. Quant. Spectrosc. Radiat. Transfer, 60, 665-710, 1998.
- Rozanov, A., Rozanov, V., Buchwitz, M., Kokhanovsky, A., and Burrows, J.: SCIATRAN 2.0 - A new radiative transfer model for geophysical applications in the 175-2400 nm spectral region, in: Atmospheric remote sensing: Earth's surface, troposphere, stratosphere and mesosphere - I, edited by Burrows, JP and Eichmann, KU, vol. 36 of Adv. Space Res., pp. 1015–1019 35th COSPAR Scientific Assembly, Paris, France, 2004, 2005.
- Sarda, K., Eagleson, S., Caillibot, E., Grant, C., Kekez, D., Pranajaya, F., Zee, R.: Canadian advanced nanospace experiment 2: Scientific and technological innovation on a three-kilogram satellite, Acta Astronautica, 59, 236-245, 2006.
- Schneising, O., Buchwitz, M., Burrows, J. P., Bovensmann, H., Reuter, M., Notholt, J., Macatangay, R., and Warneke, T.: Three years of greenhouse gas column-averaged dry air mole fractions retrieved from satellite - Part 1: Carbon dioxide, Atmos. Chem. Phys., 8, 3827–3853, 2008.
- Shimada, M., Green, R. O. and Shimoda, H.: Calibration of advanced visible and near infrared radiometer, IEEE Trans. Geosc. Rem. Sen. 37, 1472-1482, 1999.
- Suemnich K.H; Kunkel B.P; Harnisch B. Radiance source for in-flight calibration of VIS-NIR spectrometers (Proceedings Paper) SPIE , 410-415, 1998.
- Toohey, M., Quine, B. M., Strong, K., Bernath, P. F., Boone, C. D., Jonsson, A. I., McElroy, C. T., Walker, K. A., and Wunch, D.: Balloon-borne radiometer

- measurement of Northern Hemisphere mid-latitude stratospheric HNO₃ profiles spanning 12 years, *Atmos. Chem. Phys. Discuss.*, 7, 11561-11586, 2007.
- Tolton, B. T., Yurganov, L., McKernan, E., Predoi-Cross, A., and Grechko, E. I.; Intercalibration of medium-resolution grating spectrometers for MOPITT validation, *Proceedings Vol. 3756, Optical Spectroscopic Techniques and Instrumentation for Atmospheric and Space Research III*, pp. 492-499, 1999.
- Vanier, J. and Wardle, D. I., The effects of spectral resolution on total ozone measurements. *Quarterly Journal of the Royal Meteorological Society*, 95: 395–399, 2006
- Wang M., Knobelspiesse K. D., McClain C.R.: Study of the Sea-Viewing Wide Field-of-View Sensor (SeaWiFS) aerosol optical property data over ocean in combination with the ocean color products *J.G. R., VOL. 110, D10S06, 14 PP.*, 2005
- Walberg, G., H. G. Reichle, and W. H. Morrow. “Design and Testing of the Micro-MAPS Gas Filter Correlation Radiometer.” Final Report SSTI:94C:004. 21 January 1999.
- Wallace J. M., Hobbs P. V., *Atmospheric Science, An Introductory Survey*, 8, 1997.
- Walker, J. H., Saunders, R. D., Jackson, J. K., and McSparron, D. A., *NBS Measurement Services: Spectral Radiance Calibration*, NBS special publication, 102, 1987.
- Wertz J.R. and Larson W.J , *Space Mission Analysis and Design* ,110-116, 2003.
- Yang J., Wan Ch., *Advances in Climate Change Research, Progress in Research on the Impacts of Global Climate Change on Winter Ski Tourism*, 1, 5562, 2010.

- Yokota, T., Oguma, H., Morino, I., Higurashi, A., Aoki, T., and Inoue, G.: Test measurements by a BBM of the nadir-looking SWIR FTS aboard GOSAT to monitor CO₂ column density from space, in Society of Photo-Optical Instrumentation Engineers (SPIE) Conference Series, S. C. Tsay, T. Yokota, and M.-H. Ahn, 5652, 182-188, 2004.
- Zhiming K. , Marglois J., Toon G., Crisp, D., Yuk Y. : Spaceborne measurements of atmospheric CO₂ by high-resolution NIR spectrometry of reflected sunlight: An introductory study Geophysical research letters 29,15, 11.1-11.4, 2002.
- Zhang, Zhibo; Yang, Ping; Kattawar, George; Huang, Hung-Lung (Allen); Greenwald, Thomas; Li, Jun; Baum, Bryan A.; Zhou, Daniel K. and Hu, Yongxiang. A fast infrared radiative transfer model based on the adding-doubling method for hyperspectral remote-sensing applications. J. Quant. Spectrosc. Radiat. Transfer, Vol. 105, pp.243-263, 2007.
- Zhang, J., Goldstein, D. B., Varghese, P. L., Gimelshein, N. E., Gimelshein S. F., and Levin D. A.: Simulation of gas dynamics and radiation in volcanic plumes on Io, Icarus, 163, 182-197, 2003.